



저작자표시-동일조건변경허락 2.0 대한민국

이용자는 아래의 조건을 따르는 경우에 한하여 자유롭게

- 이 저작물을 복제, 배포, 전송, 전시, 공연 및 방송할 수 있습니다.
- 이차적 저작물을 작성할 수 있습니다.
- 이 저작물을 영리 목적으로 이용할 수 있습니다.

다음과 같은 조건을 따라야 합니다:



저작자표시. 귀하는 원저작자를 표시하여야 합니다.



동일조건변경허락. 귀하가 이 저작물을 개작, 변형 또는 가공했을 경우에는, 이 저작물과 동일한 이용허락조건하에서만 배포할 수 있습니다.

- 귀하는, 이 저작물의 재이용이나 배포의 경우, 이 저작물에 적용된 이용허락조건을 명확하게 나타내어야 합니다.
- 저작권자로부터 별도의 허가를 받으면 이러한 조건들은 적용되지 않습니다.

저작권법에 따른 이용자의 권리는 위의 내용에 의하여 영향을 받지 않습니다.

이것은 [이용허락규약\(Legal Code\)](#)을 이해하기 쉽게 요약한 것입니다.

[Disclaimer](#)

Doctoral Thesis

Suspended 1D metal oxide nanostructure-based  
gas sensor

Yeongjin Lim

Department of Materials Science and Engineering

Graduate School of UNIST

2018

# Suspended 1D metal oxide nanostructure-based gas sensor

Yeongjin Lim

Department of Materials Science and Engineering

Graduate School of UNIST


# Suspended 1D metal oxide nanostructure-based gas sensor

A thesis/dissertation  
submitted to the Graduate School of UNIST  
in partial fulfillment of the  
requirements for the degree of  
Doctor of Philosophy

Yeongjin Lim

06. 08. 2018

Approved by



---

Advisor

Heungjoo Shin

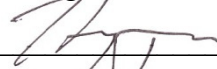
# Suspended 1D metal oxide nanostructure-based gas sensor

Yeongjin Lim

This certifies that the thesis/dissertation of Yeongjin Lim is approved.

06. 08. 2018

signature



Advisor: Heungjoo Shin

signature



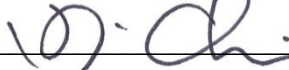
Soon-Yong Kwon

signature



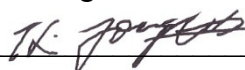
Jeong Min Baik

signature



Kyoung Jin Choi

signature



Jongbaeg Kim

## ABSTRACT

We developed a novel batch fabrication technology for the ultralow-power-consumption metal oxide gas sensing platform consisting of a suspended glassy carbon heating nanostructure and hierarchical metal oxide nanostructures forests fabricated by the carbon-micro electromechanical systems (carbon-MEMS) and selective nanowire growth process. We have developed a new manufacturing process for suspended glass carbon nanostructures such as single nanowire, nano-mesh and nano-membranes fabricated using carbon-MEMS consisting of the UV-lithography and the polymer pyrolysis processes. We designed a gas sensing platform consisting of suspended glassy carbon heating nanostructures and suspended hierarchical metal oxide nanostructure forests for the sensing part. Glassy carbon structure produced by the carbon-MEMS has many advantages such as high thermal & chemical stabilities, good hardness, and good thermal & electrical characteristics. The electrical conductivity of glassy carbon nanostructures has been increased more than three times by using rapid thermal annealing (RTA) process owing to the inferior heating property of glassy carbon nano-heater in the electrical conductivity. In order to divide the suspended glassy carbon nano-heater and the suspended hierarchical metal oxide nanostructures forests, the insulating layer of  $\text{HfO}_2$  materials is a high dielectric constant and is deposited uniformly using a atomic layer deposition (ALD) process on a suspended glassy carbon nano-heater. Suspended hierarchical metal oxide nanostructures forests were grown circumferentially on the suspended  $\text{HfO}_2$ /glassy carbon nano-heater using a hydrothermal method consisting of the seed deposition and the growth processes. For selective metal oxide seed layer deposition process, a short-time exposed polymer patterning process was performed using the positive photoresist. After the polymer patterning process, a metal oxide seed layer is deposited using the rf-sputtering system, followed by a metal oxide nanostructure growth process. The

distinguishing architecture of a suspended hierarchical metal oxide nanostructures forests/HfO<sub>2</sub>/glassy carbon nanostructure ensures efficient mass transport to the metal oxide nanostructure detection point of the gas analyte, resulting in highly sensitive gas detection. In the absence of an external heating system, the ultralow-power-consumption gas sensing platform of a suspended hierarchical metal oxide nanostructures forests/HfO<sub>2</sub>/glassy carbon nanostructure has excellent the gas sensing characteristics.

## **DEDICATION**

*This thesis is lovingly dedicated to my parents, Mindong Lim, and Mijeong Kim, for their support, sacrifice and love throughout my life.*



**TABLE OF CONTENTS**

<b>ABSTRACT</b> .....	<b>i</b>
<b>DEDICATION</b> .....	<b>iii</b>
<b>TABLE OF CONTENTS</b> .....	<b>iv</b>
<b>LIST OF FIGURES</b> .....	<b>vi</b>
<b>LIST OF TABLES</b> .....	<b>xiv</b>
<b>1. Chapter 1. Monolithic suspended glassy carbon nanostructure</b> .....	<b>1</b>
<b>1.1 Background</b> .....	<b>2</b>
<b>1.2 Fabrication &amp; Experimental</b> .....	<b>9</b>
<b>1.3 Results &amp; discussion</b> .....	<b>11</b>
<b>2. Chapter 2. Suspended Pd/glassy carbon nanowire</b> .....	<b>22</b>
<b>2.1 Background</b> .....	<b>23</b>
<b>2.2 Fabrication &amp; Experimental</b> .....	<b>26</b>
<b>2.3 Results &amp; discussion</b> .....	<b>29</b>
<b>3. Chapter 3. Suspended ZnO NWs/glassy carbon nanowire</b> .....	<b>37</b>
<b>3.1 Background</b> .....	<b>38</b>
<b>3.2 Fabrication &amp; Experimental</b> .....	<b>44</b>
<b>3.3 Results &amp; discussion</b> .....	<b>47</b>
<b>4. Chapter 4. Suspended 1D metal oxide nanostructure integrated the nano-heater</b> .....	<b>63</b>
<b>4.1 Background</b> .....	<b>64</b>
<b>4.2 Fabrication &amp; Experimental</b> .....	<b>71</b>
<b>4.3 Results &amp; discussion</b> .....	<b>75</b>

<b>5. Conclusions</b> .....	<b>100</b>
<b>REFERENCES</b> .....	<b>104</b>
<b>ACKNOWLEDGEMENTS</b> .....	<b>126</b>
<b>CURRICULUM VITA</b> .....	<b>128</b>

## LIST OF FIGURES

**Figure 1.1** Schematics showing the sensing mechanism at a sensing platform consisting of an active surface and a transducer.

**Figure 1.2** Schematics showing the nanowire nanosensors having various advantages from Y. Hunang et. al. [6].

**Figure 1.3** Categorization of the sensitivity improvement such as improving mass transport, sensing temperature and catalyst loading. As the improving mass transport, suspended structure and various nanowire morphology were shown from H. Wu et. al. [12] and J. Choi et. al. [13].

**Figure 1.4** Categorization of the carbon materials such as graphene from K. Chung et. al. [23] & C. Li et. al. [24], CNT from C. Staii et. al. [26], glassy carbon from C. Wang et. al. [31, 35], and diamond like carbon from J. Luo et. al. [28].

**Figure 1.5** The protocol of the pyrolysis process of organic compounds features three stages: (1) pre-carbonization, (2) carbonization and (3) annealing depending on the pyrolysis temperature.

**Figure 1.6** Schematic fabrication steps of a suspended carbon nanostructure.

**Figure 1.7** (a) SEM images of a suspended SU-8 wire micro-structure before the polymer pyrolysis, (b) a suspended glassy carbon wire nanostructure after the polymer pyrolysis, and (c) the suspended glassy carbon meshes.

**Figure 1.8** (a) Schematic image of the experimental, (b-e) SEM images of a suspended single glassy carbon nanowire as a FIB milling process proceeds from (b) to (e)

**Figure 1.9** (a) a HREM image at the edge of the glassy carbon nanowire, and (b) the

diffraction pattern from a glassy carbon nanowire.

**Figure 1.10** (a) Raman spectrum from a glassy carbon structure, (b-c) XPS spectrums in (b) C1s and (c) O1s regions from a glassy carbon structure and SU-8 photoresist structure.

**Figure 1.11** (a) Voltage versus current curve from a suspended glassy carbon nanowire in various temperature conditions at the measurement, (b) Electrical conductivity to the temperature curve of a suspended glassy carbon nanowire in a logarithmic scale.

**Figure 1.12** (a) Cyclic voltammogram of a suspended glassy carbon nanowire in 10 mM  $K_3Fe(CN)_6$  with 0.1 M KCl solution. (b, c) Simulated 2D concentration profiles from (b) a suspended nanowire and (c) a substrate-bound nanowire structure with the same surface area as the glassy carbon nanowire.

**Figure 2.1** Categorization of the Pd-based applications from M. Lofdahl et. al. [61] & K. J. Jeon et. al. [62] & C. Perrotton et. al. [63] & F. Favier et. al. [64] & H. H. Choi et. al. [65] & M. Penza et. al. [66].

**Figure 2.2**  $H_2$  gas sensing platforms based on the palladium depending on the dimensions from K. J. Jeon et. al. [62] & F. Yang et. al. [71] & K. R. Kim et. al. [75] & E. Lee et. al. [76] & J. Choi et. al. [13] & X. Q. Zeng et. al. [77].

**Figure 2.3** Schematic image of the fabrication of the suspended Pd/carbon nanowire for use as the  $H_2$  gas sensor.

**Figure 2.4** SEM images of the suspended SU-8 photoresist microwire; (a) bird-view, (b) top view, and (c) magnified bird-view; and the suspended glassy carbon nanowire: (d) bird-view, (e) top view, and (f) magnified bird-view. The inserted image in (d) shows a detailed view of the etched Si substrate isotropically under the  $SiO_2$  eave.

**Figure 2.5** EDS mapping images (a, carbon; b, silicon; c, palladium) of the side of the Pd-deposited glassy carbon structure shown in SEM image (d).

**Figure 2.6** (a) Schematic image of the principle of the palladium selective deposition process. (b) SEM image of Si substrate etched isotropically under the SiO<sub>2</sub> eave. (c) Electrical circuit & (d) schematic image of a suspended Pd/carbon nanowire for use as a H<sub>2</sub> gas sensing platform.

**Figure 2.7** (a) Electrical conductivity of a suspended glassy carbon nanowire fabricated by the pyrolysis of 700, 800, and 900 °C and measured at the temperature from 25 to 200 °C). (b) I-V curves of the suspended glassy carbon nanowire depending on the 5-nm-thick-Pd layer deposition.

**Figure 2.8** Gas sensing characteristics of the suspended Pd/carbon nanowire type the H<sub>2</sub> gas sensor. (a) Gas sensing responses at various concentrations from 10 to 500 ppm. (b) Gas sensing response with respect to the square root of the H<sub>2</sub> concentration. (c) Reproducible gas response over three gas injection-purging cycles at various concentrations of the H<sub>2</sub> gas. (d) Response time with respect to the H<sub>2</sub> gas concentrations (solid triangle : response time, black triangles : reciprocal of response time).

**Figure 2.9** (a) Gas sensing characteristics of the suspended Pd/carbon nanowire type the H<sub>2</sub> gas sensor for 50 ppm H<sub>2</sub> concentration at 25 (room temperature), 50, and 100 °C. (b) Comparison of the gas sensing characteristics at 50 ppm of H<sub>2</sub> gas between the suspended Pd/carbon nanowire and the substrate-bound Pd nanowire.

**Figure 3.1** Needs to gas sensing platform at various field such as biomedical, food & beverage, agriculture & Farming, environment chemical industry, and military defense.

**Figure 3.2** Some primary air pollutants react with other chemicals in the air to make

secondary air pollutants.

**Figure 3.3** Researches on n-type and p-type metal oxide semiconducting nanostructure for use as the gas sensor from H. Kim et. al. [99].

**Figure 3.4** Gas sensing mechanisms of electronic core-shell structures in (a) n-type and (b) p-type metal oxide semiconducting nanomaterials from H. Kim et. al. [99].

**Figure 3.5** Categorization of gas sensing platform based on semiconducting nanowire to enhance the gas sensing response such as hierarchical nanowire from Y. Zhang et. al.[112], network architecture from Y. Choi et. al.[113], and hierarchical suspended structure from M. R. Alenezi et. al.[114].

**Figure 3.6** Fabrication steps for hierarchical ZnO nanowires forests grown a suspended single glassy carbon nanowire for use as gas sensing platforms.

**Figure 3.7** Steps for fabricating a suspended ZnO nanowires forests/glassy carbon nanowire to apply to the gas sensing platform.

**Figure 3.8** SEM images of the hierarchical ZnO nanowires forests grown on selectively the suspended single glassy carbon nanowire; (a, b) bird-view, (c, d) cross-section view.

**Figure 3.9** SEM images of substrate-bound ZnO nanowires forests grown on (a, b) a 1- $\mu\text{m}$ -width and (c-f) a 20- $\mu\text{m}$ -width ZnO seed lines. The seed lines are 100- $\mu\text{m}$ -length.

**Figure 3.10** Point chemical analysis spectrum acquired from a suspended ZnO nanowires forests/glassy carbon nanowire; (a, b) ZnO nanowires grown on a suspended glassy carbon nanowire, (c, d) core glassy carbon nanowire.

**Figure 3.11** XRD pattern of ZnO nanowires grown on a glassy carbon structure using hydrothermal method.

**Figure 3.12** TEM analysis of a ZnO nanowires/ZnO seed layer/carbon structure. (a, b) HREM images of (b) ZnO seed layer and (c) ZnO nanowire inserted the diffraction pattern and inverse FFT image.

**Figure 3.13** I-V characteristics of ZnO nanowires grown on a suspended single carbon nanowire (olive line : carbon nanowire, orange line : ZnO seed layer/carbon nanowire, violet line : ZnO nanowires/ZnO seed layer/carbon nanowire) at (a) room temperature and (b) 200 °C.

**Figure 3.14** Gas sensing mechanisms and equivalent electrical circuit based on n-type metal oxide semiconducting materials from H. Kim et. al. [99].

**Figure 3.15** (a) Gas responses at various NO<sub>2</sub> concentrations of the suspended ZnO nanowires forests and substrate-bound ZnO nanowires forests. Resistance changes at various NO<sub>2</sub> concentrations of (b) the suspended ZnO nanowires forests and substrate-bound ZnO nanowires forests grown on (c) a 1-μm-width and (d) a 20-μm-width pads.

**Figure 3.16** (a) Gas responses of a ZnO nanowires forests/carbon nanostructure versus various concentrations of NO<sub>2</sub>. (b) Response time and recovery time versus various NO<sub>2</sub> gas concentrations.

**Figure 3.17** Long term stability of the gas sensing platform based on ZnO nanowires forests grown on a suspended carbon nanowire: the gas response and recovery behaviors for 500 ppb NO<sub>2</sub> were tested in the period of 60 days.

**Figure 3.18** Gas sensing characteristics of a ZnO nanowires forests/carbon nanostructure based gas sensor for various CH<sub>4</sub> gas concentration mixed in dried air at 200 °C.

**Figure 3.19** Gas sensing characteristics of a ZnO nanowires forests/carbon nanostructure based gas sensor for various CO gas concentration mixed in dried air at 200 °C.

**Figure 3.20** Gas sensing characteristics of a ZnO nanowires forests/carbon nanostructure based gas sensor for various C<sub>6</sub>H<sub>6</sub> gas concentration mixed in dried air at 200 °C.

**Figure 3.21** Gas sensing characteristics of a ZnO nanowires forests/carbon nanostructure based gas sensor for various H<sub>2</sub> gas concentration mixed in dried air at 200 °C.

**Figure 3.22** Gas sensing characteristics of a ZnO nanowires forests/carbon nanostructure based gas sensor for various SO<sub>2</sub> gas concentration mixed in dried air at 200 °C.

**Figure 3.23** Gas selectivity based on a suspended hierarchical ZnO nanowires forests/glassy carbon nanowire in dried air at 200 °C.

**Figure 4.1** Development of metal oxide semiconductor gas sensors in size and power efficiency from J. Burgues et. al. [135].

**Figure 4.2** Schematic showing the increase in the degree of alignment of the graphitic phase owing to the RTA process.

**Figure 4.3** Schematic image of detailed our gas sensing platforms based on the suspended hierarchical metal oxide nanostructures grown on the HfO<sub>2</sub>/glassy carbon nanowire integrated the heating system.

**Figure 4.4** Schematic image of our gas sensing platforms and an electrical circuit.

**Figure 4.5** Schematics of mechanisms of the HfO<sub>2</sub> deposition fabricated by the atomic layer deposition process.

**Figure 4.6** Fabrication steps for a suspended hierarchical ZnO nanowires forests/HfO<sub>2</sub>/glassy carbon nanowire for use as gas sensor integrated a heating system.

**Figure 4.7** (a) Pyrolysis condition for the glassy carbon structure fabrication and (b) RTA process condition for the enhancement of the electrical conductivity.



**Figure 4.8** SEM images of (a) a suspended and (b) a substrate-bound carbon nanowire. I-V characteristics of (c) a suspended and (d) a substrate bound nanowire.

**Figure 4.9** Electrical conductivities of a suspended and a substrate-bound glassy carbon nanowire at pyrolysis condition before and after the RTA process.

**Figure 4.10** Raman spectrum of a glassy carbon structure before (green line) and after RTA process (orange line) consisting of (a) 600 °C, (b) 700 °C, (c) 800 °C, and (d) 900 °C .

**Figure 4.11** XPS analysis a glassy carbon structure before (green line) and after RTA process (orange line) consisting of (a) 600 °C, (b) 700 °C, (c) 800 °C, and (d) 900 °C .

**Figure 4.12** (a, b) TEM image, (c, d) diffraction pattern, and (e) inverse FFT of a suspended glassy carbon nanowire after the RTA process. (f, g) TEM image, (h, i) diffraction pattern of a substrate-bound glassy carbon nanowire.

**Figure 4.13** Breaking down voltages of various insulating materials such as Al<sub>2</sub>O<sub>3</sub>, HfO<sub>2</sub>, SiO<sub>2</sub> deposited on a suspended single glassy carbon nanowire.

**Figure 4.14** The electrical resistance of (a) a suspended glassy carbon, (b) hierarchical ZnO nanowires forests changed by the temperature of an external heater. The electrical resistance of hierarchical ZnO nanowires forests depending on the applied voltage of a suspended glassy carbon nanowire. (c) The predicted temperature of an internal heater by the applied voltage of a suspended glassy carbon structure.

**Figure 4.15** (a) Simulation results of the temperature profile based on the Joule heating model at the suspended nano-structure. Temperature changes of the suspended nanowire depending on the applied voltage.

**Figure 4.16** (a) Resistance changes of ZnO nanowires forests grown on the HfO<sub>2</sub>/carbon

nanowire with respect to (left) power consumption of the carbon nanowire heater and (right) temperature of the external heater. (b) Comparison of the temperature between the simulation results and experimental results at the suspended nano-structure.

**Figure 4.17** Gas sensing characteristics of the ultralow-power consumption gas sensor of suspended hierarchical ZnO nanowire forests/HfO<sub>2</sub>/carbon nanostructure for various gases such as CH<sub>4</sub>, C<sub>6</sub>H<sub>6</sub>, CO, NO<sub>2</sub>, H<sub>2</sub> and SO<sub>2</sub> and gas concentrations mixed in dried air at 1.5-mW power heated at the suspended carbon nanostructure.

**Figure 4.18** Gas responses at 50 ppb NO<sub>2</sub> gas consisting of internal heater and external heater of a suspended and substrate-bound ZnO nanowire structure.

**Figure 4.19** Response time and recovery time versus various NO<sub>2</sub> gas concentration using internal and external heater (between suspended and substrate-bound structure) to compare gas sensing characteristics from 50 to 500 ppb.

**Figure 4.20** Gas sensing characteristics of the suspended hierarchical metal oxide nanowires such as ZnO and CuO grown on selectively HfO<sub>2</sub>/carbon nanowire at various gases and gas concentrations depending on the heater power consumption such as (a) 0.8 mW, (b) 1.4 mW, (c) 2.4 mW and (d) 3.1 mW.

**Figure 4.21** Discrimination of six gases by the ultralow-power consumption gas sensor at four temperatures using static response.

**Figure 4.22** Influence of humidity response to nitrogen dioxide. Real time difference of gas response depending on humidity and overcoming gas response through heating.

**Figure 4.23** Long-term stability of the ultralow-power-consumption gas sensor based on suspended 1D metal oxide nanostructure: the gas response and recovery behaviors for 500 ppb NO<sub>2</sub> were tested for a period of 7 days.

## LIST OF TABLES

**Table 1.** Structural dimension change of a suspended glassy carbon single nanowire after the polymer pyrolysis process.

**Table 2.** Structural dimension changes of a suspended SU-8 micro-structure in various pyrolysis temperature conditions. The temperature conditions include natural cooling down processes of the microwires after the polymer pyrolysis processes listed in the table.

**Table 3.** Power consumption using the metal oxide semiconductor gas sensor integrated the MEMS heating system.

**Table 4.** Categorization of the breaking down voltage of the insulating materials such as  $\text{Al}_2\text{O}_3$ ,  $\text{HfO}_2$ ,  $\text{SiO}_2$ .

**Table 5.** Relative parameters ( $R_g/R_a$ ) of 6 gas sensor array for the target gas response.

**Table 6.** Relative sensitivities ( $S_{ij}$ ) of gas sensor array to the tested gases.

**Table 7.** Normalized pattern data by preprocessing of gas sensor array signals.

**Table 8.** Pattern recognition algorithms with the PCA process.

# 1

## **Suspended glassy carbon nanostructure**

*In this chapter, a monolithic glassy carbon nanostructure fabricated by carbon-MEMS will be introduced. The chemical composition and physical properties are also given.*

# 1 Suspended glassy carbon nanostructure

## 1.1 Background

A sensor is a device that provides a functioning output in response to a specific input measured, which could be a physical or chemical quantity, property, or state [1]. The sensor acquires the physical parameters and converts them into signals suitable for processing. Sensors could be physical, electrical, magnetic, optical, chemical thermal, or a mixture of two or more of these. The sensor consists of an active face and a transducer [1-2].

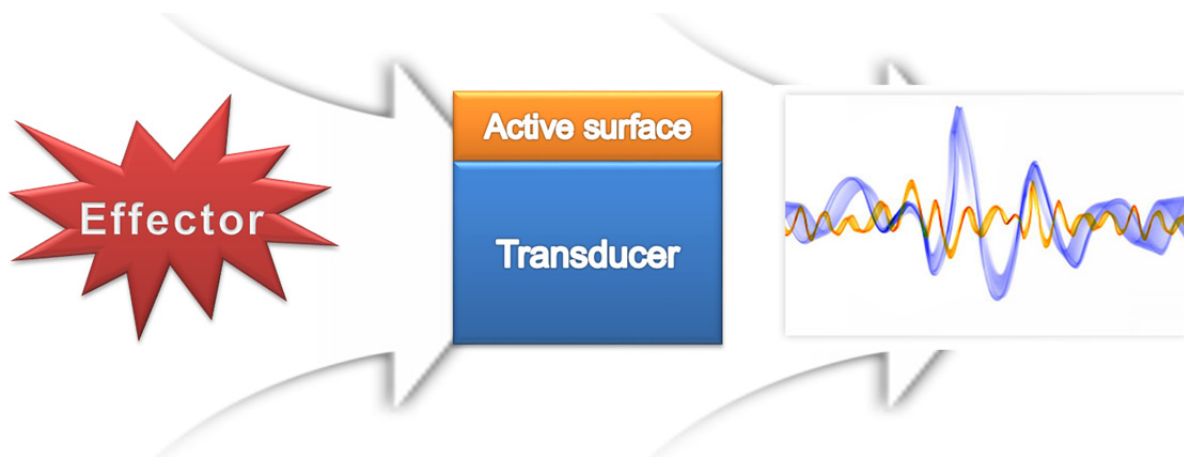
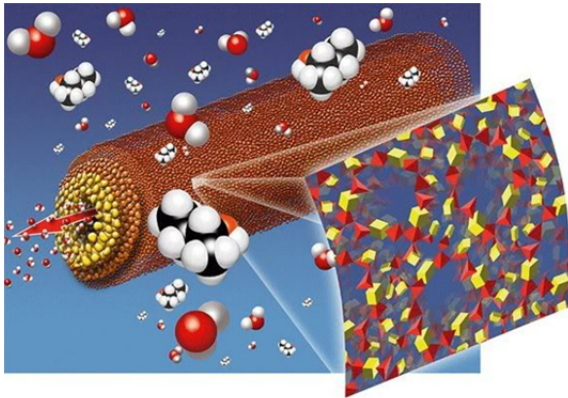


**Figure 1.1** Schematics showing the sensing mechanism at a sensing platform consisting of an active surface and a transducer.

Sensors require high sensitivity and accurate analysis, real-time and rapid analysis and miniaturization techniques [1-5]. Nanowire sensors were introduced by the research group because of the high surface to volume ratio and the quantum confinement effect [5-6]. Nanowire sensors have many advantages, including high sensitivity and surface to volume ratio, efficient mass transport and simple configuration [3-6].



High surface to volume ratio

Quantum confinement effect

H. L. Casticum et. al.  
*Chem. Commun.* **9** (2008) 1103-1105

**Figure 1.2** Schematics showing the nanowire nanosensors having various advantages from Y. Hunang et. al. [6].

To improve sensitivity on the sensing platform, there are 3 categorizes of improved mass transfer, temperature sensing catalytic loading, with an emphasis on improving mass transfer [7-9]. The research groups have introduced the nanowire morphology and the suspended structure [10-11]. Hierarchical architecture is a larger surface area than other nanoscale morphologies in the nanowire architecture. The hierarchical nanostructure has the largest surface to volume ratio, but the dead surface comes into contact with the substrate [11]. Suspended architectures have the advantage of high surface to volume ratio, improved mass transfer, and no interference from the substrate. Having a hierarchical architecture and a suspended architecture in the nanowire sensor reduces response and recovery time and improves sensitivity [11]. However, it is difficult to fabricate a public type-based architecture using only a simple and cheap process. In order to make the architecture, it could be classified as the top-down and bottom-up processes. The bottom up process is the build process. The bottom up process is consisting of the self-assembly process, atomic layer deposition (ALD) and molecular beam epitaxy (MBE) and metal organic chemical vapor deposition (MOCVD) and has disadvantages of the poor mechanical & electrical contact, poor control and low throughput [14-17]. On the other hand, the top down process is the

milling process introduced the lithography, printing, stamping, molding [18-21]. Although the top down process is able to overcome these disadvantages of the bottom up process, the top down process is the expensive & the complex process.

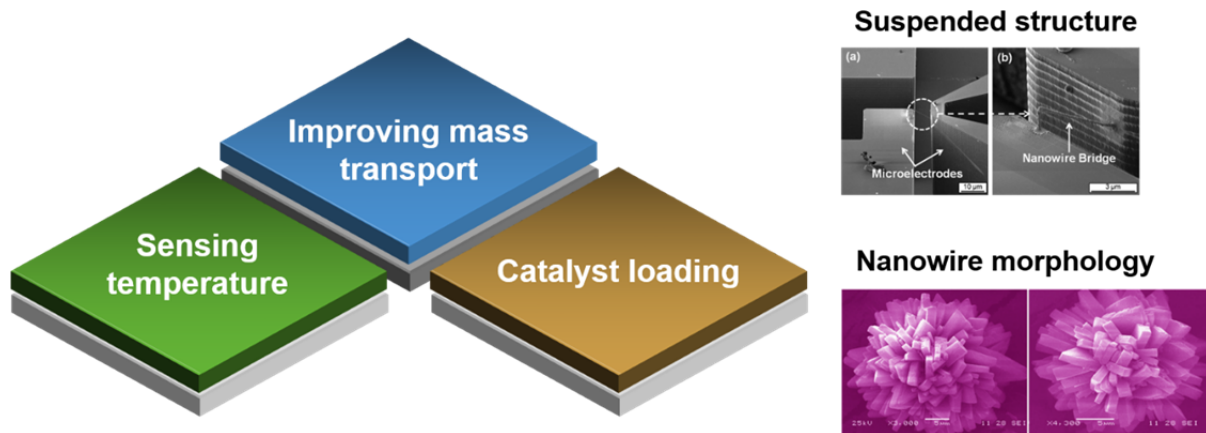


**Figure 1.3** Categorization of the sensitivity improvement such as improving mass transport, sensing temperature and catalyst loading. As the improving mass transport, suspended structure and various nanowire morphology were shown from H. Wu et. al. [12] and J. Choi et. al. [13].

Carbon exists in a variety of isotopes such as graphene, carbon nanotube (CNT), diamond-like carbon, pyrolytic carbon, and glassy carbon, and these have been extensively developed due to their unique properties [22-29]. Of these carbon materials, the glassy carbon exhibits a wide range of electrochemical stability windows, excellent biocompatibility, excellent thermal and chemical stability, low gas permeability and high thermal and electrical conductivity [29-32]. The low reactivity and gas impermeability of the glassy carbon is introduced by a fullerene-grade model containing sp<sup>2</sup>-bonded carbon which is predominantly non-graphitized [32].

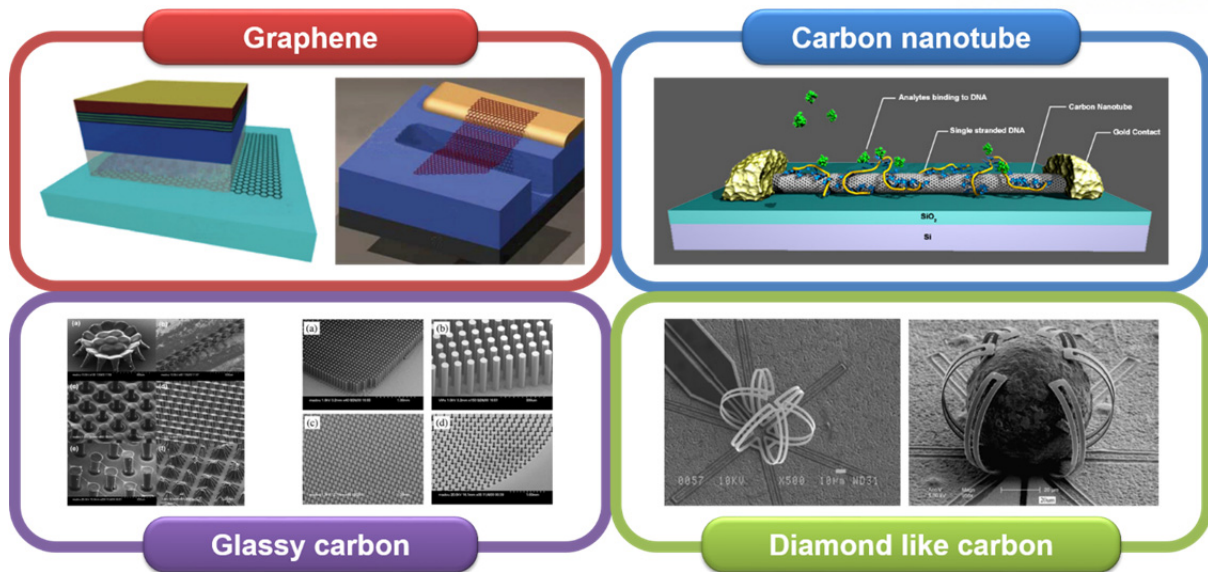


**Figure 1.4** Categorization of the carbon materials such as graphene from K. Chung et. al. [23] & C. Li et. al. [24], CNT from C. Staii et. al. [26], glassy carbon from C. Wang et. al. [31, 35], and diamond like carbon from J. Luo et. al. [28].

Since the polymer pyrolysis process does not proceed, the glassy carbon phases consist of a tetrahedral diamond ( $sp^3$  hybridized carbon) structure and a stacked planar ( $sp^2$  hybridized carbon) graphite structure [32]. The pyrolysis temperature is lower than the temperature at which the graphite is formed, making it difficult to exist as the perfect graphite structure in the carbon structure. Glassy carbon is used because of its many advantages not found in graphite, which is present in glassy carbon [33]. Because of the many advantages of glassy carbon, the researchers have developed the solar cell system, Li-ion batteries, optical memory devices and electrochemical bio sensing platforms [33-36]. A more useful manufacturing method called carbon micro-electro-mechanical systems (carbon-MEMS) has been developed using the glassy carbon. Carbon-MEMS shows a monolithic 3D glassy carbon micro-/nano-structures of a suspended structure consisting of the polymer patterning processes such as the photolithography, electrospinning, e-beam lithography and nanoimprint and the polymer pyrolysis [37-41]. Particularly, when the patterning polymer structures using



the photolithography, carbon-MEMS constitutes a simple and relatively inexpensive manufacturing process.

During the polymer pyrolysis, the polymer structures undergoes dramatic volume shrinkage and that shrinkage is isotropic and predictable [36]. The pyrolysis process results in a dramatic volume reduction of up to 90 %, which transforms the photoresist micro-structure into a carbon nano-structure, enabling nano-fabrication of carbon structures without the use of complex nano-manufacturing processes. In the case of the e-beam lithography, it is possible to form an expandable polymer nano-structure that is pre-patterned by an e-beam passing through a thin polymer layer [37]. By using the photolithography instead of the e-beam lithography, the photoresist micro-structure could be patterned in batch fabrication to enable simple and inexpensive [38]. The photolithography is a process of making nano-structure, but the photoresist micro-structure is changed to a glassy carbon nano-structure due to the volume reduction which is dramatically reduced under the the pyrolysis condition.

The pyrolysis process is the carbonization process in which the carbon residue-rich solid residue is obtained from the organic materials [42-49]. The pyrolysis process of the organic materials can be roughly divided into three steps: (1) pre-carbonization, (2) carbonization and (3) annealing. During the pre-carbonization ( $T < 300\text{ }^{\circ}\text{C}$ ), the solvent molecules and unreacted monomers are removed from the the pre-patterned polymer structure. Next, the carbonization can be divided into two sub-steps; from 300 to 500  $^{\circ}\text{C}$  of the first sub-step, Removal of the hetero-atoms of the halogens and oxygen creates a network of conjugated carbon systems and a rapid mass loss during the initial removal of hydrogen atoms; and from 500 to 1200  $^{\circ}\text{C}$  of the second sub-step, where hydrogen, oxygen and nitrogen atoms are completely removed and aromatic structures are interconnected. At this point, the permeability decreases and density, hardness, the Young's modulus and electrical

conductivity increase. Finally, the annealing process should be performed at temperatures above 1,200 °C to gradually remove defects. The final pyrolysis conditions determine the degree of carbonization and the residuals of the external elements [50-51].

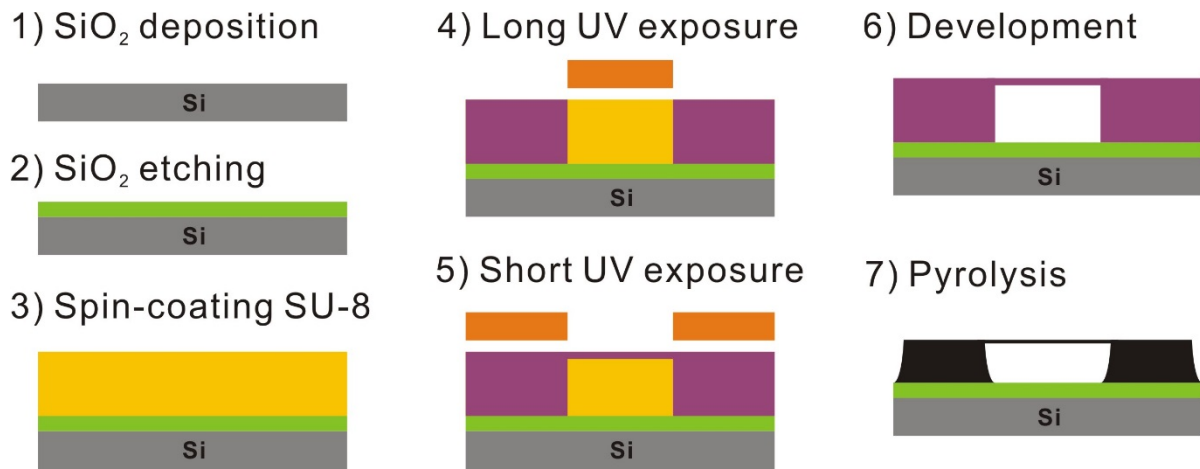


**Figure 1.5** The protocol of the pyrolysis process of organic compounds features three stages: (1) pre-carbonization, (2) carbonization and (3) annealing depending on the pyrolysis temperature.

The nanoscale structure has a high surface effect, but most of it is placed on the substrate and the surface area could be not utilized to the maximum. It is possible to increase the surface effect using a suspended nano-structure. The suspended glassy carbon nanowires were fabricated by an electro-spinning process to enhance the surface effect [39]. The electro-spinning process is a fiber manufacturing process in which an electric force is applied to draw a charging filament of a polymer solution, or a polymer is melted in a fiber form in a nanometer [39]. When a satisfactorily high voltage is applied to the droplet, the volume of the liquid is charged and the electrostatic repulsion stabilizes the surface tension and the droplet stretches from the surface with the flow of the liquid outlet as the main point. This point is denoted as Taylor cone. This cone is determined by the ratio of surface tension to electrostatic repulsion in the slow acceleration of osmotic pressure. The fiber is increased by whipping due to electrostatic repulsion in convection of the rapid acceleration. In order to produce a suspended glassy carbon nano-structure by electro-spinning, the polymer nanowires produced by an electrospinning process are formed on a glassy carbon post, and the pyrolysis process is carried out twice. The diameter of the polymer nanowire determines the applied voltage, drum spinning speed and polymer density.

In this study, novel monolithic suspended glassy carbon nano-structures from nanowire to nanomeshes were developed through the photolithography and the polymer pyrolysis process. By the photolithography, the suspended polymer micro-structure is created and a single pyrolysis process proceeds. The photolithography process is cheaper and more aligned than the electro-spinning process. The geometries of a bridge-type suspended nanowire were characterized by the scanning electron microscopy (SEM). The carbon materials such as sp-2 hybridized carbon and sp-3 hybridized carbon were analyzed using the Raman spectroscopy. For the feasibility of the suspended glassy carbon nanowires, the electrical, electrochemical properties were experimented and stimulated.

## 1.2 Fabrication & Experimental



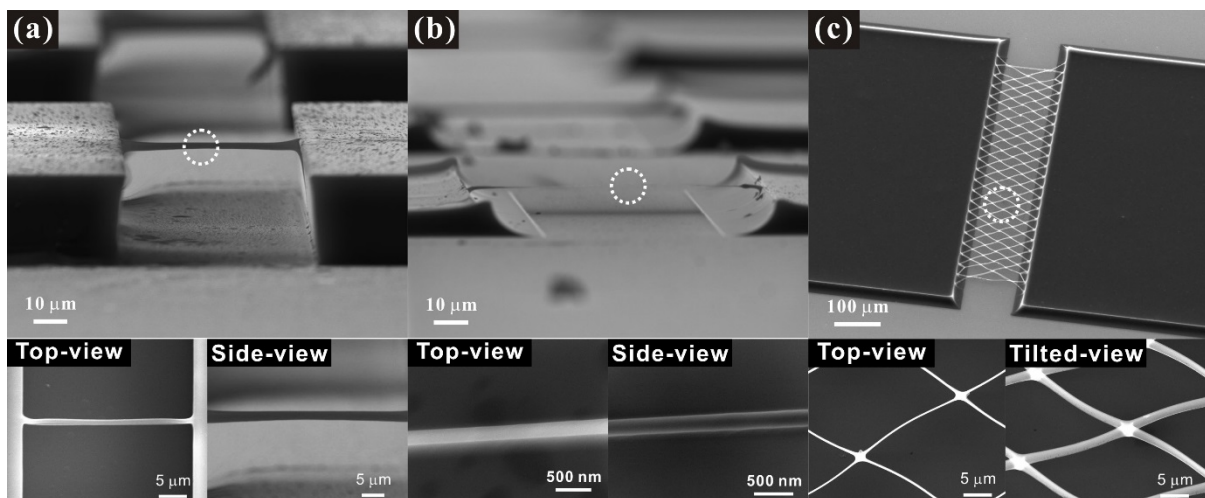
**Figure 1.6** Schematic fabrication steps of a suspended carbon nanostructure.

Figure 1.6 shows the fabrication processes of a suspended glassy carbon nanostructure. First, an insulating layer having a thickness of 1  $\mu\text{m}$  made of SiO<sub>2</sub> was deposited on a 6-inch Si wafer (p-type, B-doped,  $8 \sim 12 \Omega \cdot \text{cm}^2$ , 660- $\mu\text{m}$  thickness) by a wet process using a thermal oxidation method. The SiO<sub>2</sub>/Si substrate was cleaned using a hot piranha solution (4 : 1 = H<sub>2</sub>SO<sub>4</sub> : H<sub>2</sub>O<sub>2</sub>, J.T. Baker, USA) and dehydrated on a hot plate at 200 °C for 5 minutes. A 30- $\mu\text{m}$ -thick negative photoresist (SU-8 2025, Microchem. Corp., USA) was coated on a SiO<sub>2</sub>/Si substrate using a spin-coating system, followed by a long UV exposure on thick posts supported by a suspended micro-wire, followed by a short UV exposure for patterning 1- $\mu\text{m}$  wide photoresist line. The single post exposure bake and development process has released a suspended photoresist micro-wire array. After suspended photoresist wire micro-structure was made, the suspended photoresist micro-structure was converted to a suspended glassy carbon nano-structure using the polymer pyrolysis process. The pyrolysis condition consists of the post-baked time and carbonized time. At post-baked time, the sample was heated to 300 °C at a ramping rate of 1 °C/min and held for 60 min. The temperature was increased to 1000 °C at an increasing rate of 1 °C/min and maintained for 60

minutes to convert from photoresist microwire to glassy carbon nanowire. The temperature was steadily decreased to room temperature using the natural cooling. Vacuum conditions of about  $10^{-6}$  torr are maintained during the polymer pyrolysis process. The suspended photoresist wire micro-structure and the suspended glassy carbon wire nano-structure were performed by a SEM (Quanta 200, FEI, USA), a high-resolution transmission electron microscopy (HRTEM, JEM-2100F, JEOL Ltd., Japan) and a focused-ion beam milling (FIB, Quanta 3D FEG, FEI company, USA). The development of the suspended glassy carbon nanowire structure has been studied by Raman spectroscopy (Alpha300R, WITec, Germany) and X-ray photoelectron spectroscopy (XPS : K-alpha, Thermo Fisher Co. Ltd., UK). The electrical conductivity was measured depending on the temperature in the natural convection oven (ON-02GW, JEIO TECH Co., Ltd., Republic of Korea) using the source-meter (Keithley 2400, Keithley Instruments Inc., USA).

### 1.3 Results & discussion

The shape of the glassy carbon nanostructures bridging the two glassy carbon posts is roughly an isometrically shrunk version of the suspended microscale photoresist wire connecting the two SU-8 posts, as shown in Figure 1.7 (a) and (b). The width of the photoresist wire matches the size of the photomask pattern, but the photoresist wire thickness varies with the total UV light absorbed by the photoresist as determined by the second UV exposure. For the same pyrolysis duration, the photoresist structure experience different amounts of shrinkage ranging from 40 to 90 % depending on the original photoresist structure sizes, as listed in Table S1. The smallest photoresist microwire with a width of 1  $\mu\text{m}$  and a thickness of 2  $\mu\text{m}$  is converted to a glassy carbon nanowire with a width of 195 nm and a thickness of 210 nm, corresponding to a size reduction of 80 ~ 90 %.



**Figure 1.7** (a) SEM images of a suspended SU-8 wire micro-structure before the polymer pyrolysis, (b) a suspended glassy carbon wire nanostructure after the polymer pyrolysis, and (c) the suspended glassy carbon meshes.

On the other hand, the length of the glassy carbon nanowires increased from 54.0  $\mu\text{m}$  to 89.4  $\mu\text{m}$  due to the volume shrinkage of the two posts supporting the suspended wire.

Even with this large elongation (39.6 %), the resulting longitudinal tension in the glassy carbon nanowires was not significant, as demonstrated by FIB milling experiment of the glassy carbon nanowire, as shown in Figure 1.8. We have found that the glassy carbon nanowires were cut using FIB equipment and the sum of the lengths of the two glassy carbon nanowires did not differ significantly from the length of the single glassy carbon nanowires before the cross section; this means that the tensile stress of the carbon nanowires is not large (in this case the wire would have expected to “bounce”). Importantly, the glassy carbon nanowires are slightly bent upward. We pointed out that the development of the transverse slope of the stress along the nanowire thickness, which is the upper part of the nanowire, is not the case when stress is applied to the bottom of the nanowire.

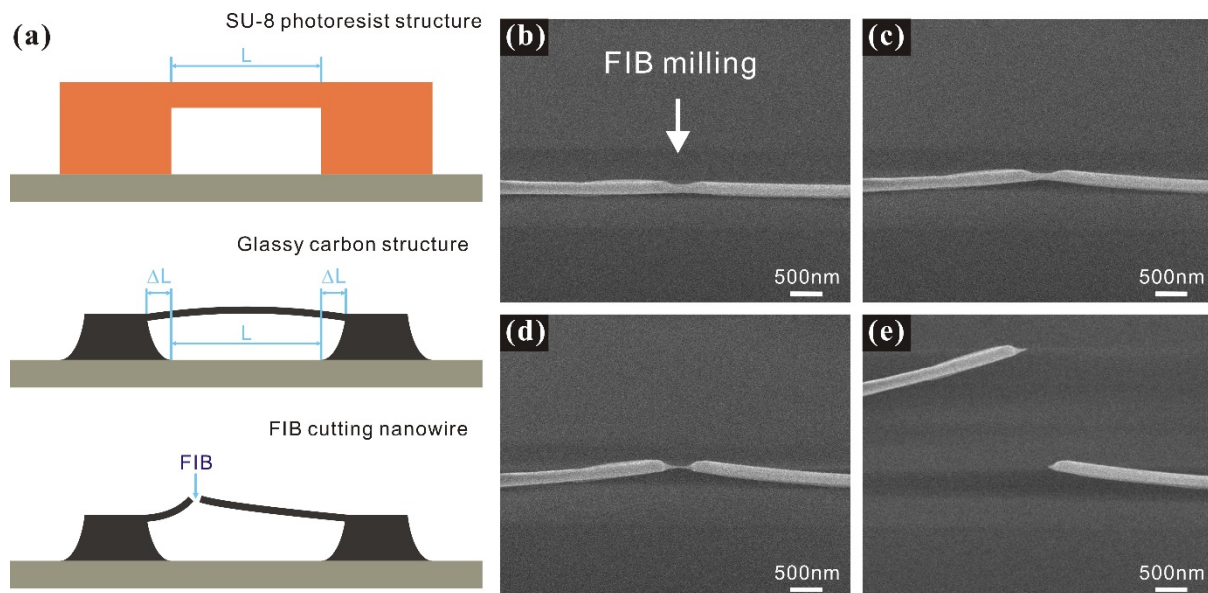
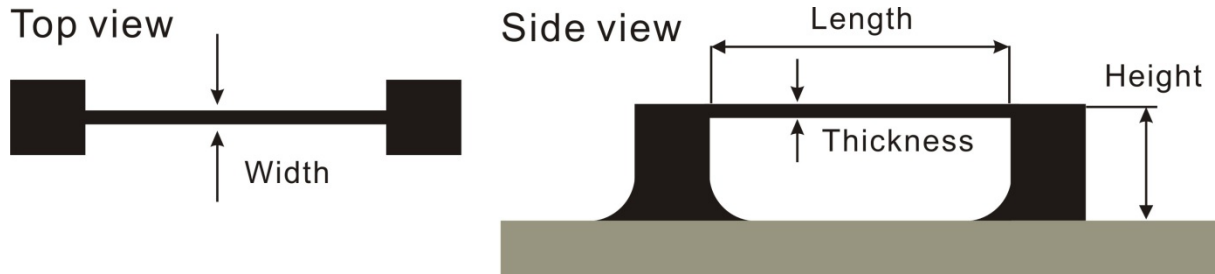


**Figure 1.8** (a) Schematic image of the experimental, (b-e) SEM images of a suspended single glassy carbon nanowire as a FIB milling process proceeds from (b) to (e)

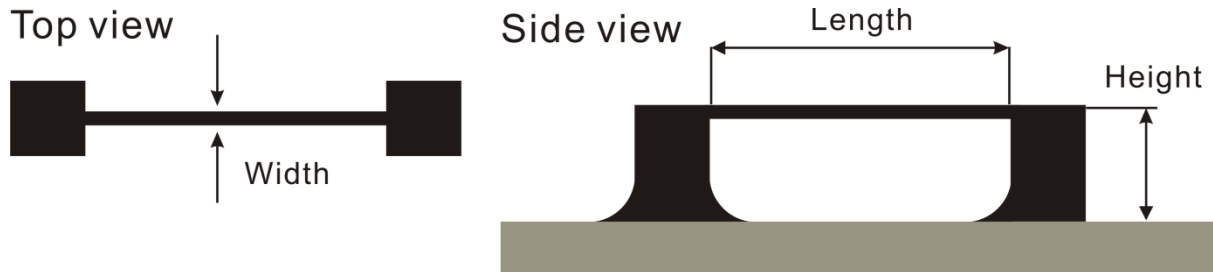
**Table 1.** Structural dimension change of a suspended glassy carbon single nanowire after the polymer pyrolysis process.



	Width [ $\mu\text{m}$ ]	Thickness [ $\mu\text{m}$ ]	Height [ $\mu\text{m}$ ]	Length [ $\mu\text{m}$ ]
Suspended polymer microstructures	1	2	27.3	54.0
	2	6.5		
	3	7.3		
	4	10.2		
Suspended carbon nanostructures	0.195	0.21	11.4	89.4
	0.6	1.56		
	0.74	1.99		
	1.12	2.87		



**Table 2.** Structural dimension changes of a suspended SU-8 micro-structure in various pyrolysis temperature conditions. The temperature conditions include natural cooling down processes of the microwires after the polymer pyrolysis processes listed in the table.



Pyrolysis temperature conditions	Suspended wire		Bulk post
	Width [ $\mu\text{m}$ ]	Length [ $\mu\text{m}$ ]	Height [ $\mu\text{m}$ ]
Before pyrolysis	1	55.8	24
300°C for 2 min	0.675	63.5	20.2
350°C for 2 min	0.495	79.2	15.3
400°C for 2 min	0.430	82.7	12.9
450°C for 2 min	0.359	84.4	11.5
500°C for 2 min	0.305	85.0	11.4
500°C for 60 min	0.296	85.8	10.6
350°C for 60 min and 900°C for 60 min	0.195	89.4	10.0

This result and the shrinkage as a function of the polymer pyrolysis temperature were obtained from the experiment, as listed in the Table 1. It is deduced that the SU-8 photoresist occurs in the early stages of the pyrolysis at up to  $\sim 450$  °C. This is done before the solid carbon formation takes place as known in the literature [53], and the photoresist structure is flexible enough to withstand large amounts of elongation without breakage. The volume continues to decrease at the 450 °C to 900 °C solid carbonization part, but the volume shrinkage is much less than the low temperature volume reduction part. Therefore, a small

amount of longitudinal stress along the glassy carbon nanowire could be explained by the fact that most dimensional changes occur on the polymer and only small dimensional changes occur in the carbon formation itself. It should be emphasized that a slow temperature ramp rate of 1 °C/min during the polymer pyrolysis process and the natural cooling process tends to heat the excess stress accumulated in the glassy carbon structure. The shape of the support posts is converted from a brick-shape to a quadrupole tent shape, and the wire is bent downward from the support to which the nanowire and the post are connected, as shown in Figure 1.7 (b). This geometric shape is the result of very good adhesion of the SU-8 photoresist to the substrate, with the bottom of the post being strongly held by the substrate during the polymer pyrolysis process, while the top of the post is likely to shrink. As a result of the non-uniform volume reduction of the this type of post, the sidewall profile of the post changes from a straight-line wall to a curved shape, with the result that the suspended nanowire experience more elongation at the kidney than at the bottom is curved down ward. The difference from the elongation of the bottom over the thickness of the nanowire which causes the stress gradient in the transverse direction of the nanowire is just like this. The SU-8 photoresist wire is formed thicker in the support, as shown in Figure 1.7 (b) & (c), because the limited exposed area of the suspended wire site at the 2<sup>nd</sup> UV exposure is sharply expanded in the support so that the UV energy is transmitted deeper in the support. The SU-8 photoresist support remains thicker than the wire through polymer pyrolysis, transforming it into a thick carbon flexural support. This bridged glassy carbon nanowire nano-structure and the tensile stresses are not critical, but they increase with the nanowire thickness to improve the structural integrity of the nanowire, and the glassy carbon nanowires with high aspect ratio (~ 450) even when wet-processed with a very small gap of the substrate.

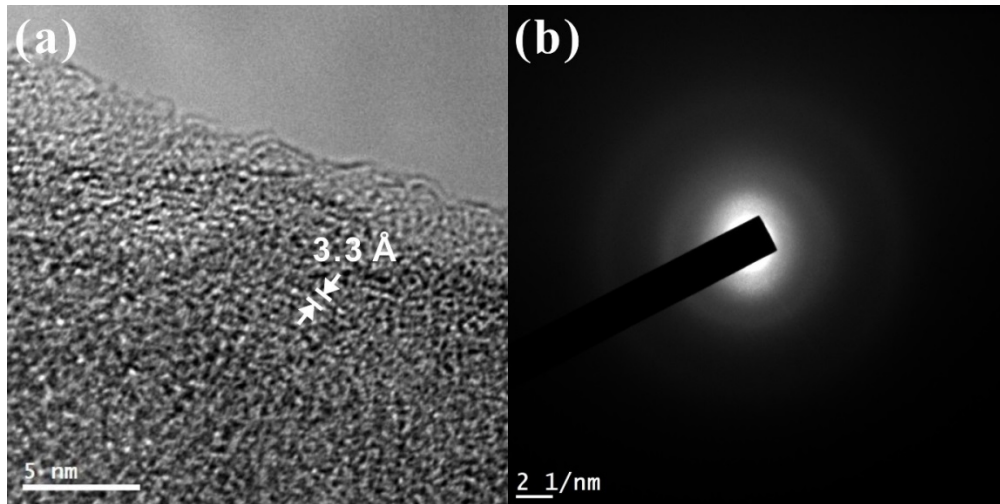


**Figure 1.9** (a) a HREM image at the edge of the glassy carbon nanowire, and (b) the diffraction pattern from a glassy carbon nanowire.

In contrast to suspended glassy carbon nanowires fabricated using electrospinning, the suspended glassy carbon nanowires of a UV-lithography pattern could be formed in various forms such as the nanomeshes, as shown in Figure 1.7 (c). Dimensions, including width and aspect ratio, and locations of SU-8 photoresist structure are determined by the photomask patterns and the UV dose, as shown in the Figure 1.7 (a). The suspended glassy carbon nanomesh is designed to be angled to the bulk carbon post edge so that each intersection of the four short glassy carbon nanowires evenly supported by for nanowires. This rugged mesh design is designed to avoid stiction between neighboring wires due to surface tension during the development and to be slanted at the bulk carbon post edge so that each junction where the four short carbon wires intersect is evenly distributed by four nanowires, is supported evenly by the four nanowires. This robust mesh design avoids stiction between adjacent wires due to surface tension during the development and breakage of the mesh structure during the polymer pyrolysis, and as a result, the nanowires could be spaced at small intervals.

The microstructure of the glassy carbon structures was studied using HREM and

Raman spectroscopy. Figure 1.9 shows an HREM image at the edge of a glassy carbon nanowire of  $\sim 190$ -nm diameter. Since the diameter of the suspended glassy carbon nanowires is so large that electrons are not transmitted across the center of the nanowires, only the edges of the glassy carbon nanowires can be clearly observed in the TEM. The properties of the glassy carbon nanowires are mainly disordered, but exhibit several short-range ordered nanostructure. In this work, suspended glassy carbon nanowires do not exhibit well-developed graphite shells surrounding irregular carbon cores as found in electro-spun glassy carbon nanowires [40]. The flow of the photoresist through the small nozzles in electro-spinning improves the disentanglement of the photoresist, which is enhanced by the electrical biasing and mechanical attraction of the electro-spun photoresist, resulting in more graphitization during the polymer pyrolysis process. The reason for the low graphite content in current glassy carbon nanowires is that the SU-8 photoresist chain does not dissolve during processing as much as the electro-spun photoresist. The nature of the microstructure of the nanowire was confirmed by the diffraction pattern in the TEM, as shown in Figure 1.9 (b). The ring-shaped diffraction pattern represents a short-range crystal order, and the fog pattern surrounded by the ring pattern represents a graphite-like defect [54]. The short-range crystallinity of the glassy carbon has been confirmed using Raman spectroscopy [33, 55].

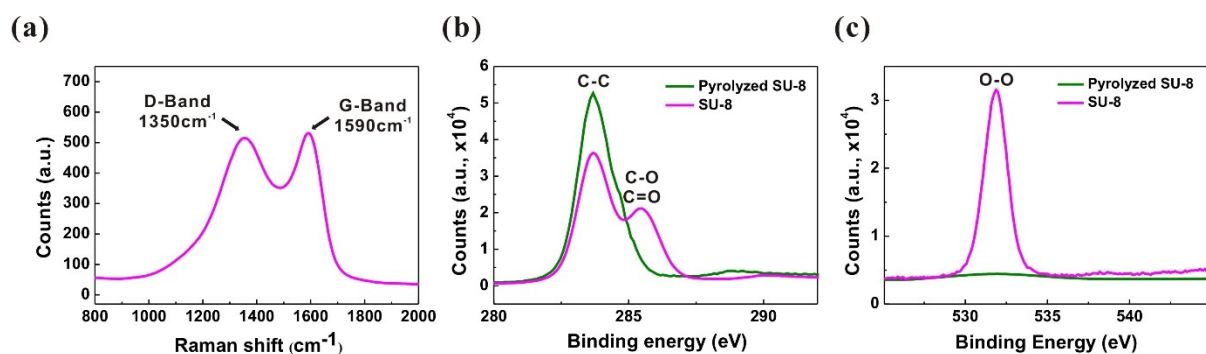


**Figure 1.10** (a) Raman spectrum from a glassy carbon structure, (b-c) XPS spectrums in (b) C1s and (c) O1s regions from a glassy carbon structure and SU-8 photoresist structure.

The Raman spectrum of the glassy carbon post is shown in Figure 1.10 (a). The G-band at  $1590\text{ cm}^{-1}$  represents the  $\text{sp}^2$  hybrid graphite phase and the D-band at  $1350\text{ cm}^{-1}$  originates from the disordered carbon phase [55]. The overlapping shapes of the D and G bands the relative intensity of the two bands corresponds to TEM images of mixture of aligned carbon and disordered carbon.

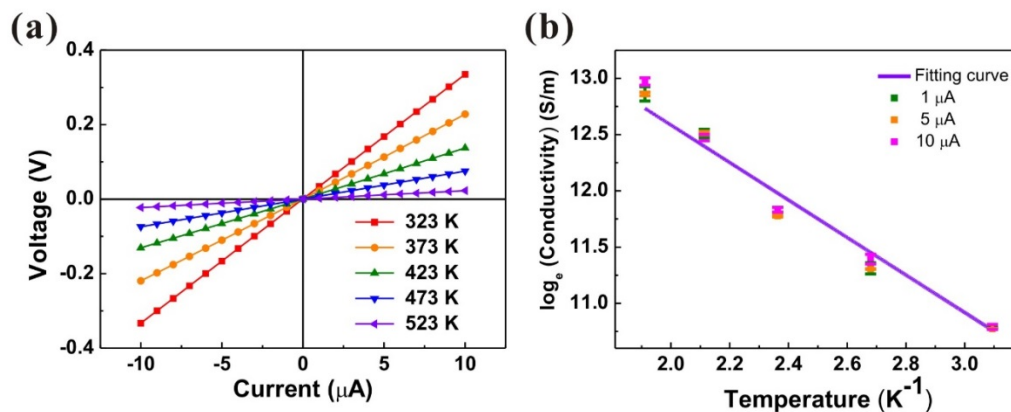


**Figure 1.11** (a) Voltage versus current curve from a suspended glassy carbon nanowire in various temperature conditions at the measurement, (b) Electrical conductivity to the temperature curve of a suspended glassy carbon nanowire in a logarithmic scale.

The oxygen-to-carbon (O/C) ratio is used to characterize the composition of the carbonized materials. The high-resolution XPS spectrum is shown in the C1s and O1s regions of the glassy carbon structure and the SU-8 photoresist structure, respectively at the Figure 1.10 (b, c). The C1s spectrum of the SU-8 photoresist structure consists of peaks of 283.7 eV and 285.9 eV. The peak at 285.9 eV corresponds to carbon bound to oxygen and the peak at 283.7 eV represents the aromatic and aliphatic carbon of the SU-8 photoresist [56]. The C1s spectrum of the glassy carbon structure has a single peak at 283.7 eV only. In the O1s spectrum, the glassy carbon is characterized by a peak at 531.8 eV at which the intensity from the corresponding peak of the SU-8 photoresist was significantly reduced prior to the polymer pyrolysis process. The difference in O/C ratio between the SU-8 photoresist

structure (23.2 %) and the polymer pyrolysis process (3.1 %) confirms low levels of oxygen in the glassy carbon structure. These results are consistent with those obtained with other glassy carbon structures treated with the polymer pyrolysis processes [57].

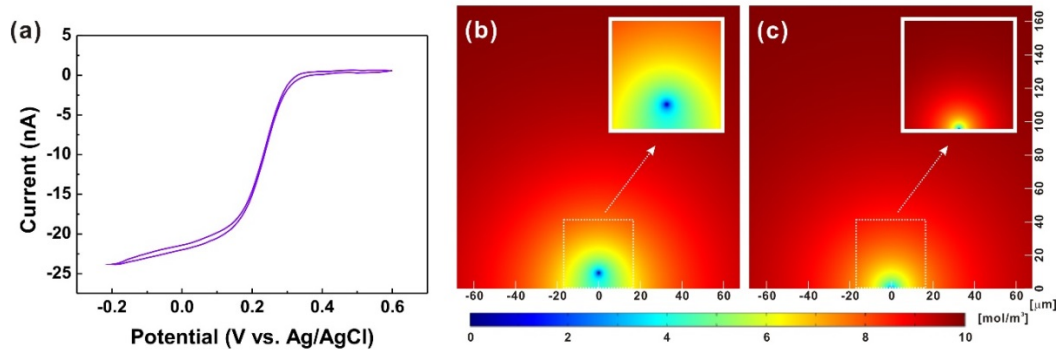


**Figure 1.12** (a) Cyclic voltammogram of a suspended glassy carbon nanowire in 10 mM  $K_3Fe(CN)_6$  with 0.1 M KCl solution. (b, c) Simulated 2D concentration profiles from (b) a suspended nanowire and (c) a substrate-bound nanowire structure with the same surface area as the glassy carbon nanowire.

The electrical conductivity of the suspended glassy carbon nanowires is characterized using a two-probe  $I$ - $V$  technique using the posts as the contact pads instead of using four-point probe method. Because the nanowire is monolithically connected to the post, the influence of the contact resistance and spreading resistance, which are the main causes of the electrical measurement error, can be ignored and the two-probe method can be used for this experiment. Carbon nanowires have a much greater resistance than glassy carbon posts due to their large size differences. Glassy carbon nanowires with a width and the thickness of  $\sim 190$ -nm exhibited excellent ohmic contact and decreased wire resistance with increasing temperature, as shown in the Figure 1.11. The resistance change of the glassy carbon nanowires was measured in a convection oven. The sample was equilibrated for 2,000 s at each temperature so that the temperature of the glassy carbon nanowire matched the temperature of the convection oven. The applied current was limited to  $\leq 10 \mu A$  in order to

avoid the nanowire temperature rise due to the joule heating effect. Temperature and resistance inversely is proportional to the behavior of semiconducting suspended glassy carbon nanowires. Similar electrical conductivities of the glassy carbon nanowires have been reported by the other research groups. The electrical conduction mechanism is the disordered carbon and is described by a hopping-based mechanism at the low temperatures ( $< 250$  K) [58] and a thermal activation mechanism at the high temperatures ( $> 250$  K) [59]. As electrical measurements are performed at the temperature higher than the room temperature, the following electrical conductivity and temperature relationships apply.

$$\sigma(T) = \sigma_0 \exp\left(-\frac{\epsilon_{act}}{k_B T}\right) \quad (1)$$

where  $\sigma_0$  is a constant,  $k_B$  is the Boltzmann constant, and  $\epsilon_{act}$  is the activation energy. The activation energy  $\epsilon_{act}$  is defined as  $\epsilon_{act} = \epsilon_C - \epsilon_F$ , where  $\epsilon_C$  is the conduction band edge and  $\epsilon_F$  is the Fermi level. The activation energy obtained by fitting a plot of  $\ln(\sigma)$  versus  $1/T$  from the electrical conductivity measurement results was about 0.146 eV.

The electrochemical properties of the suspended glassy carbon nanowires were characterized using the cyclic voltammetry in a 10 mM  $K_3Fe(CN)_6$  solution with 0.1 M KCl. The measured diffusion limited electrochemical currents were compared with simulated electrochemical currents from the suspended glassy carbon nanowires and a substrate-bounded glassy carbon nanowire having cross-sectional areas as the experimental nanowire. The measured diffusion limited electrochemical current was 81.6 nA at 0.6 V and the simulated electrochemical current results from a suspended glassy carbon nanowire and the substrate-bounded glassy carbon nanowire were 82.0 nA and 43.4 nA at 0.6 V, respectively. The agreement between the measured diffusion limited electrochemical current and the simulated electrochemical current indicates that a suspended glassy carbon nanowire surface

has significant electrochemical properties. Although only a quarter of the surface area of the glassy carbon nanowire bonded to the substrate was blocked by the substrate surface, the diffusion limited electrochemical current of the substrate-bounded glassy carbon nanowires reduced to 53 % from the suspended glassy carbon nanowire. This result, in addition to the freedom of substrate surface effects such as contamination and substrate temperature changes, is advantageous in the mass transfer of the suspended carbon nanowires across substrate-bounded glassy carbon nanowire geometry.



# 2

## Suspended Pd/glassy carbon nanowire

*In this chapter, a suspended Pd/glassy carbon nanowire will be introduced to apply the gas sensing platform. Also, fabrication steps and material property will be given.*

## 2 Suspended Pd/glassy carbon nanowire

### 2.1 Background

Palladium (Pd) has been actively developed as a hydrogen ( $H_2$ ) gas sensing material because its electrical resistance and volume change with the concentration of the  $H_2$  gas. This characteristic enables  $H_2$  sensing by simply measuring the electrical properties of Pd nanomaterials as a function of  $H_2$  gas concentration. This simple gas sensing approach facilitates the gas sensor miniaturization and placement process by making the Pd-based  $H_2$  gas sensor compatible with the MEMS process [60].

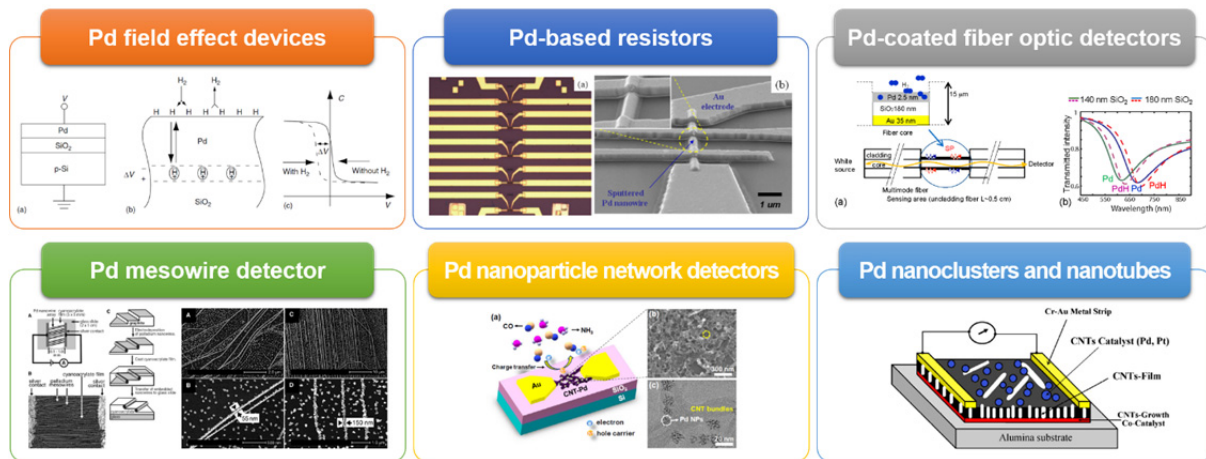


**Figure 2.1** Categorization of the Pd-based applications from M. Lofdahl et. al. [61] & K. J. Jeon et. al. [62] & C. Perrotton et. al. [63] & F. Favier et. al. [64] & H. H. Choi et. al. [65] & M. Penza et. al. [66].

Pd-nanostructure-based  $H_2$  gas sensors have been fabricated using a variety of the manufacturing methods including e-beam lithography, anodized aluminum oxide (AAO) templating, electrodeposition, electrophoresis and the focused ion beam (FIB) milling [62, 67-70]. This Pd-nanostructure-based  $H_2$  gas sensor showed the high sensitivity and fast response. However, the performance of the Pd-nanostructure-based  $H_2$  gas sensors could be

limited by the effect of the substrate formed in contact such as stagnation layer formation and contamination. This disadvantage could be overcome by placing the Pd nanostructure on the substrate at a fixed distance. In addition, the effect of the high surface-to-volume ratio of the nanostructures on the gas detection capability and mass transfer to the sensing region of the gas analyte can be improved by separating the sensing structure from the substrate, since more nanostructure surface areas are  $H_2$  gas. The nanowires can be placed on a substrate between pre-patterned electrodes using dielectric migration, field synthesis and FIB-chemical vapor deposition (CVD) growth [71-74]. However, these methods have limitations such as poor control of the size and the position of the nanostructures or complicated manufacturing processes.

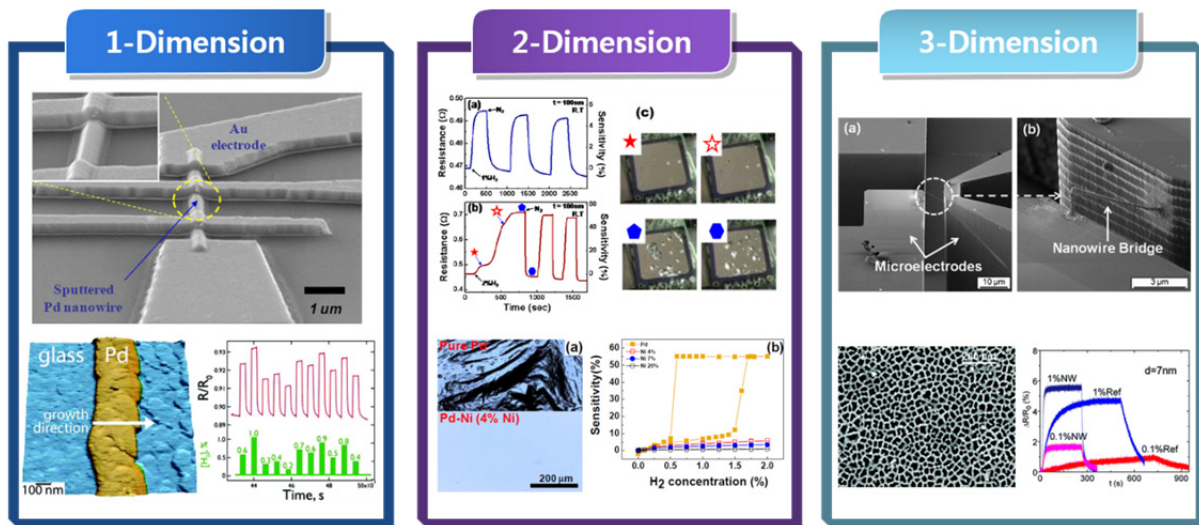


**Figure 2.2**  $H_2$  gas sensing platforms based on the palladium depending on the dimensions from K. J. Jeon et. al. [62] & F. Yang et. al. [71] & K. R. Kim et. al. [75] & E. Lee et. al. [76] & J. Choi et. al. [13] & X. Q. Zeng et. al. [77].

In this work, we have developed the suspended glassy carbon nanowires selectively functionalized with a thin Pd layer as the  $H_2$  gas sensor.  $SiO_2$  was patterned using an isotropic Si etch process fabricated by the Induced Coupled Plasma (ICP) etch process

under the glassy carbon electrodes. Because this eave served as a shadow mask during Pd deposition, a simple Pd evaporation process without complex lithography processes such as e-beam lithography and FIB milling processes selectively deposited only on the suspended glassy carbon nanowire and two glassy carbon post electrodes. In order to improve the effect of the Pd layer on the total resistance change of the suspended glassy carbon nanowire, the electrical conductivity of the glassy carbon materials was modulated by controlling the pyrolysis condition of the temperature.

## 2.2 Fabrication & Experimental

The manufacturing processes for a suspended carbon nanowire functionalized with the Pd layer are illustrated in Figure. 2.3. A 1  $\mu\text{m}$  thick  $\text{SiO}_2$  layer was deposited on a 6-inch Si wafer (p-type, boron doped, 5-20  $\Omega\cdot\text{cm}$ , 660 – 700  $\mu\text{m}$ ; LG Siltron Co., Ltd., Republic of Korea) using the wet oxide process based on a thermal oxidation process. The  $\text{SiO}_2/\text{Si}$  substrate was washed with the hot piranha solution ( $\text{H}_2\text{SO}_4 : \text{H}_2\text{O}_2 = 4 : 1$ ) and dehydrated at 200  $^\circ\text{C}$  for 5 minutes on a hot plate. A 1.5- $\mu\text{m}$ -thickness positive photoresist mask (AZ-5214E, AZ Electronic Materials, USA) was patterned on a  $\text{SiO}_2/\text{Si}$  substrate using the UV-lithography to produce a  $\text{SiO}_2$  shadow mask. After patterning the  $\text{SiO}_2$  shadow mask using buffered oxide etch (BOE, J. T. Baker, Chemical Co., Ltd., USA) solution, the Si part was isotropically etched to a thickness of 10  $\mu\text{m}$  under the  $\text{SiO}_2$  shadow mask using the ICP etching (Tegal 200, Alcatel Micro Machining System, France). By this isotropic etching, the  $\text{SiO}_2$  eave was formed on top of the etched Si substrate. The  $\text{SiO}_2/\text{Si}$  substrate was thoroughly cleaned using a hot piranha cleaning process and then dehydrated. A negative 30  $\mu\text{m}$  thick negative photoresist (SU-8 2025, Microchem. Corp., USA) was coated using a spin-coating process and soft-baked on a hotplate at 95  $^\circ\text{C}$  for 8 min, the coated negative photoresist was exposed to a UV dose (200  $\text{mJ}\cdot\text{cm}^{-2}$ ) sufficient to thoroughly polymerize the photoresist and form the post structures on top of the  $\text{SiO}_2$  eaves that support a suspended negative photoresist microscale wire. A subsequent second UV exposure of a short dose (16  $\text{mJ}\cdot\text{cm}^{-2}$ ) is performed to polymerize only a shallow region of the negative photoresist through a photomask including an open area having the shape of a wire bridging the exposed post structure. After a post-exposure bake process using a hotplate at 95  $^\circ\text{C}$  for 6 min, a monolithic negative photoresist structure consisting of a suspended microwire and two posts was patterned by a single batch fabrication step. A monolithic negative photoresist micro-structure

has been converted to a monolithic glassy carbon nanostructure after the polymer pyrolysis process. During the polymer pyrolysis process, the size of the negative photoresist structures has been greatly reduced. Thus, the diameter of a suspended negative photoresist microwire was reduced to a sub-micrometer scale while the length of a suspended structure was lengthened. Finally, a Pd layer (5 nm) was deposited on a single-layer glassy carbon nanostructure using an e-beam evaporation process, and the deposited Pd layer was annealed at 250 °C and  $7.0 \times 10^{-4}$  torr for 5 min using the rapid thermal annealing machine (RTA, RTA-2000, Korea vacuum Tech., Republic of Korea). In the Pd layer deposition process, the glassy carbon post was electronically connected by the Pd layer only through the suspended glassy carbon nanowire, because the SiO<sub>2</sub> eave formed by the isotropic Si etch process acted as a shadow mask for the selective Pd layer deposition.

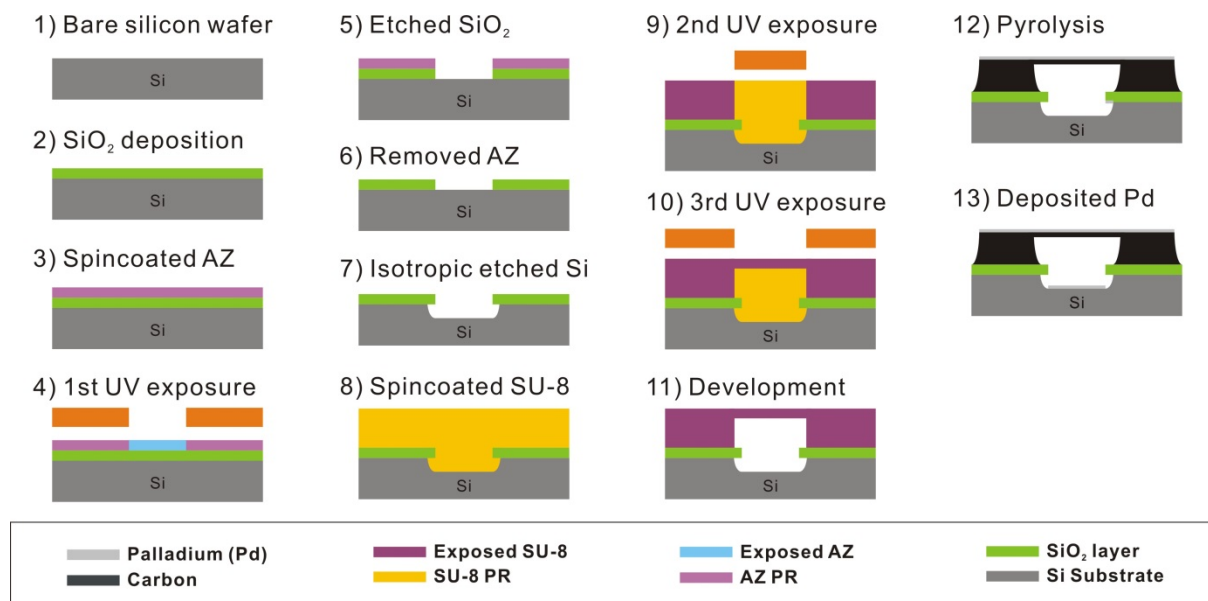


**Figure 2.3** Schematic image of the fabrication of the suspended Pd/carbon nanowire for use as the H<sub>2</sub> gas sensor.

The H<sub>2</sub> gas sensing response of the Pd-nanostructure-based H<sub>2</sub> gas sensor was characterized at atmospheric pressure in a chamber equipped with an external heater and four

mass flow meter systems. Prior to H<sub>2</sub> gas detection, the trapped unknown gas in the chamber was purged by several vacuum pinging and N<sub>2</sub> gas purging cycles. H<sub>2</sub> gas concentration was controlled by mixing 1000 ppm H<sub>2</sub> in N<sub>2</sub> and N<sub>2</sub> gas using a gas flow controller (GMC1200, ATOVAC, Republic of Korea). During the flow of the H<sub>2</sub>/N<sub>2</sub> gas mixture in a chamber under various temperature conditions, changes in the electrical properties of the glassy carbon nanowires functionalized with Pd were measured by the source meter (Keithley 2401, Keithley Instruments, Inc., USA).

## 2.3 Results & discussion

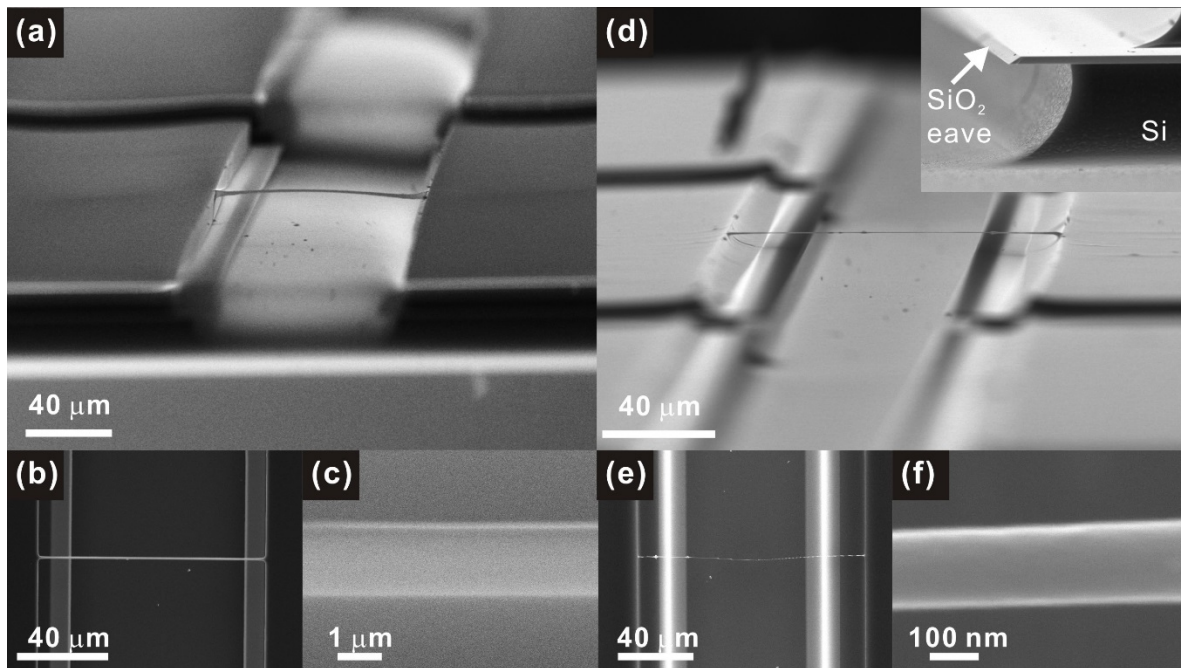


**Figure 2.4** SEM images of the suspended SU-8 photoresist microwire; (a) bird-view, (b) top view, and (c) magnified bird-view; and the suspended glassy carbon nanowire: (d) bird-view, (e) top view, and (f) magnified bird-view. The inserted image in (d) shows a detailed view of the etched Si substrate isotropically under the SiO<sub>2</sub> eave.

Suspended photoresist microwire in 1- $\mu\text{m}$ -wide and 1.5- $\mu\text{m}$ -thickness were reduced by  $\sim 90\%$  to create 110-nm-wide and 150-nm-thick suspended glassy carbon nanowire. At the same time, the length of the wire increased from 102.2- $\mu\text{m}$  to 122.5- $\mu\text{m}$  due to the volume reduction of the post structure. The size reduction feature of the suspended structure was that the Si substrate was isotropically etched and patterned on a SiO<sub>2</sub> mask forming a SiO<sub>2</sub> eave and a Si trench in Figure 2.4. Since the Si trench extends under the eaves of SiO<sub>2</sub>, SiO<sub>2</sub> eaves can serve as a shadow mask in the Pd evaporation process. The photolithography-free Pd deposition process using e-beam evaporation enabled a monolithic glassy carbon nanostructure that was selectively deposited as a Pd layer without the electrical



connection between the two glassy carbon posts through the Si substrate under the SiO<sub>2</sub> eaves.

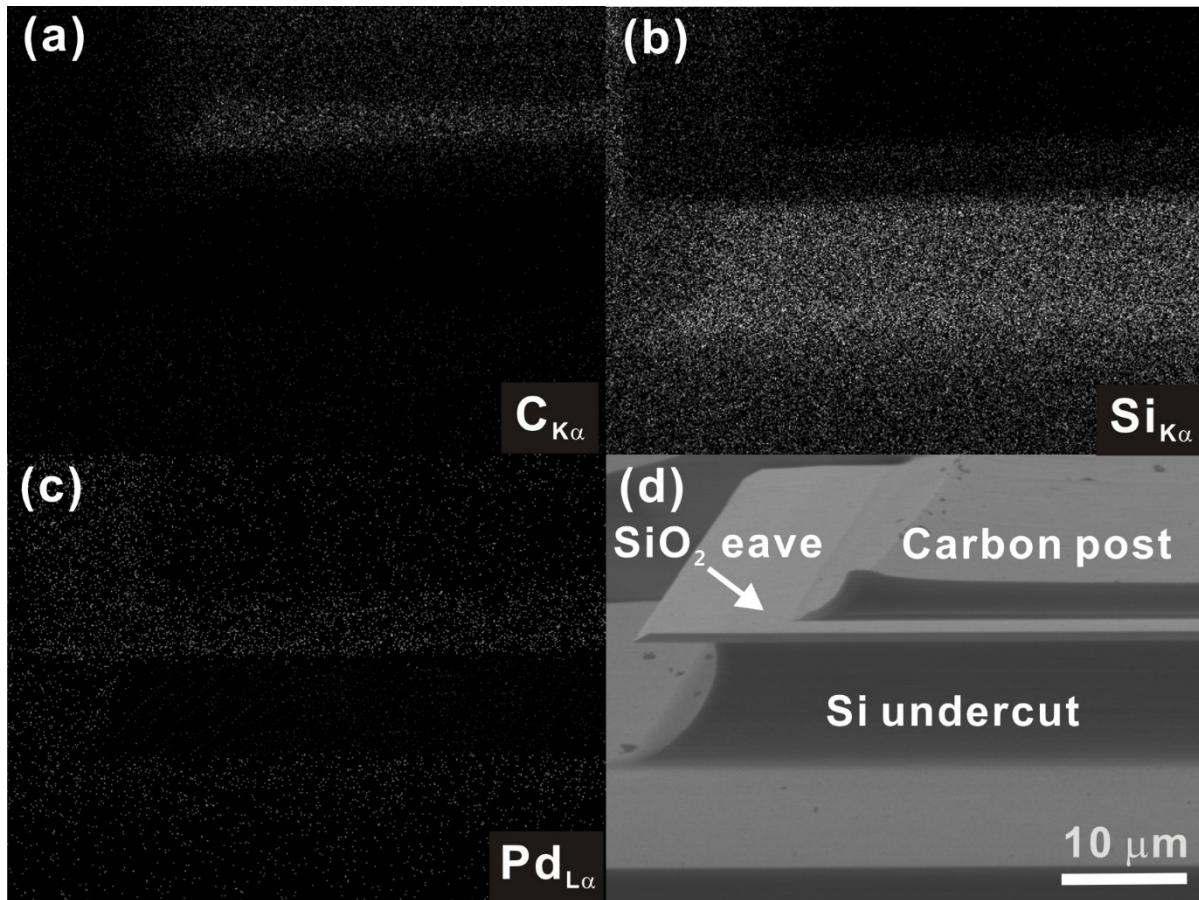


**Figure 2.5** EDS mapping images (a, carbon; b, silicon; c, palladium) of the side of the Pd-deposited glassy carbon structure shown in SEM image (d).

The effect of the SiO<sub>2</sub> eaves as a shadow mask has been confirmed by measuring the electrical resistance between the Pd-deposited glassy carbon post and the Si substrate, and chemical composition analysis of mapping the side wall composition of the Pd-deposited glassy carbon structure using electron dispersive spectroscopy (EDS, X-Max, Horiba, Ltd., Japan). The electrical characteristics showed no electrical connections and the chemical composition analysis did not reveal an important part of the Pd materials in the etched Si undercut area under the SiO<sub>2</sub> eaves in Figure 2.5.

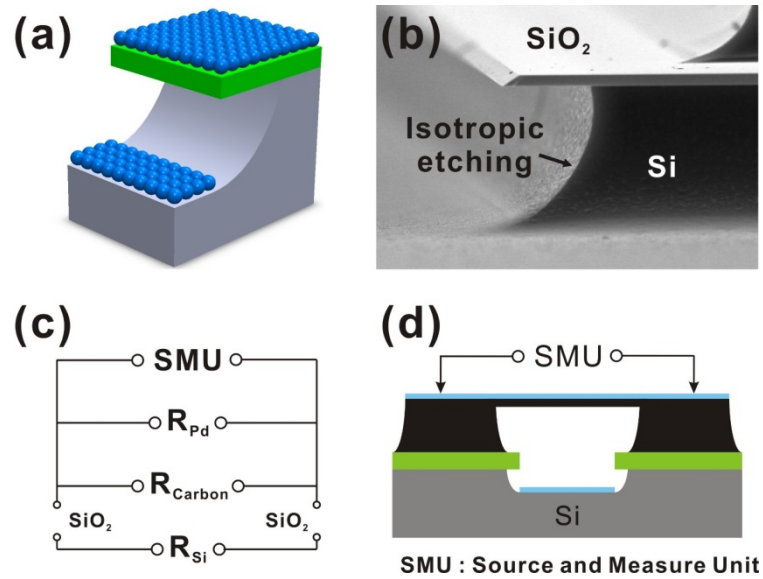


**Figure 2.6** (a) Schematic image of the principle of the palladium selective deposition process. (b) SEM image of Si substrate etched isotropically under the SiO<sub>2</sub> layer. (c) Electrical circuit & (d) schematic image of a suspended Pd/carbon nanowire for use as a H<sub>2</sub> gas sensing platform.

The H<sub>2</sub> gas sensing was carried out by measuring the change of electrical properties of the Pd-deposited glassy carbon nanowire. A mixed electrical characteristic appears along the nanowire between the glassy carbon and the Pd layer. Considering the large difference between the glassy carbon posts and the suspended glassy carbon nanowire, it is believed that the suspended glassy carbon nanowire and the deposited Pd layer are connected in parallel. In this section, the mixed electrical properties of Pd-deposited glassy carbon nanowire are more sensitive to changes in the resistance of the Pd layer as a result of H<sub>2</sub> gas concentration changes as a ratio of the electrical properties of the glassy carbon nanowire to the electrical properties of the metallic carbon nanowire Pd layer increase. In this study, the electrical properties of the glassy carbon nanowire were controlled by changing the pyrolysis conditions of the temperature. The electrical characteristics of the glassy carbon nanowire depend on the graphitic composition ratio which increases with increasing the pyrolysis

temperature. The electrical characteristics of the suspended glassy carbon nanowire treated with the polymer pyrolysis at 700, 800, 900 °C were measured while the temperature was varied from 25 to 200 °C. The electrical characteristics of the glassy carbon nanowire were not significantly changed (about  $\pm 10\%$ ) in the size reduction of the glassy carbon in the polymer pyrolysis process at various temperatures but decreased with increasing polymer pyrolysis temperature. Therefore, the electrical characteristics of a suspended glassy carbon nanowire increased in Figure 2.7.

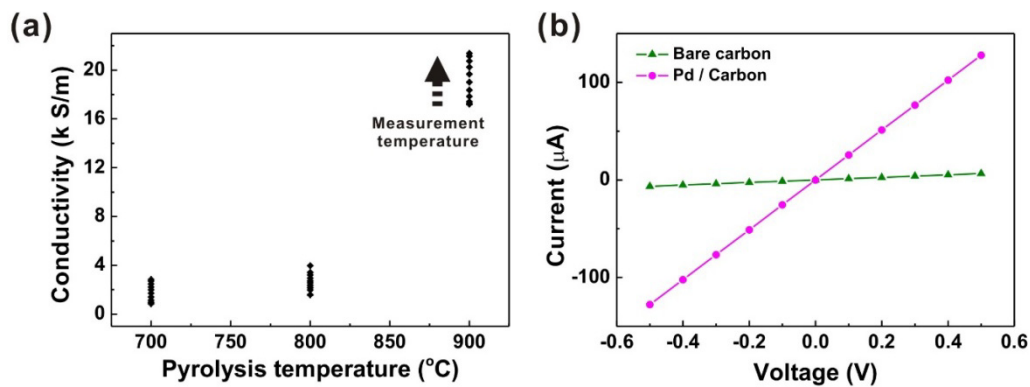


**Figure 2.7** (a) Electrical conductivity of a suspended glassy carbon nanowire fabricated by the pyrolysis of 700, 800, and 900 °C and measured at the temperature from 25 to 200 °C). (b) I-V curves of the suspended glassy carbon nanowire depending on the 5-nm-thick-Pd layer deposition.

Glassy carbon nanowires pyrolyzed at 700 °C were selected as the H<sub>2</sub> gas sensing platform. Under all the pyrolysis temperature conditions, the glassy carbon nanowires exhibited the semiconducting materials in the electrical conductivity-temperature relationships, and electrical conductivity increased as the measurement temperature increased. As shown in Figure 2.7, the electrical characteristics of the suspended carbon nanowires were reduced 20 times after the deposition of the Pd layer of 5-nm-thickness, and the Pd-deposited glassy carbon nanowires showed good ohmic contact characteristics.

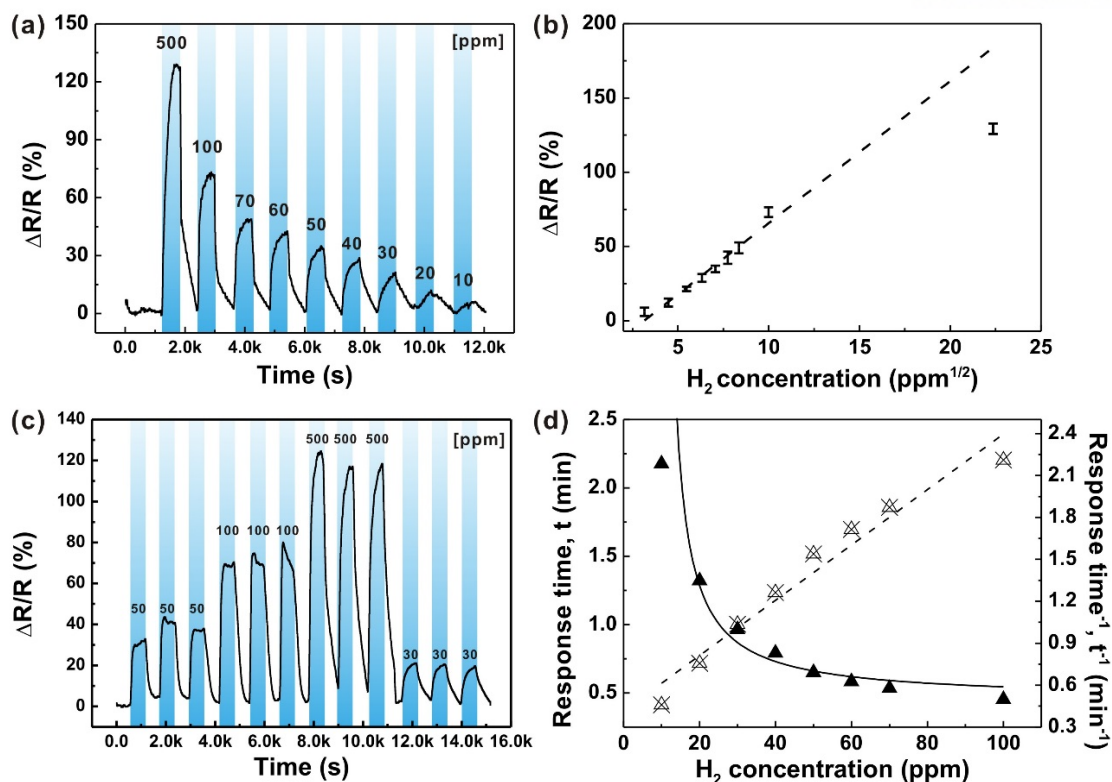


**Figure 2.8** Gas sensing characteristics of the suspended Pd/carbon nanowire type the H<sub>2</sub> gas sensor. (a) Gas sensing responses at various concentrations from 10 to 500 ppm. (b) Gas sensing response with respect to the square root of the H<sub>2</sub> concentration. (c) Reproducible gas response over three gas injection-purging cycles at various concentrations of the H<sub>2</sub> gas. (d) Response time with respect to the H<sub>2</sub> gas concentrations (solid triangle : response time, black triangles : reciprocal of response time).

The characteristics of the H<sub>2</sub> gas sensing platform based on the Pd deposited on the glassy carbon nanowires show that the H<sub>2</sub> gas concentration is varied from 500 ppm to 10 ppm and the heater temperature at which the H<sub>2</sub> gas sensing chip is placed is maintained at 100 °C. The gas reaction was proportional to the H<sub>2</sub> gas concentration from 10 to 100 ppm due to PdH<sub>x</sub> (Palladium hydride) formation; then, the gas reaction slowly saturates. The electrical characteristics of the glassy carbon nanowires deposited with Pd increased from 5.9 % at 10 ppm and 129.3 % at 500 ppm. In the Langmuir adsorption isotherm model, the

adsorption ( $r_a$ ) and desorption ( $r_d$ ) rates of dissociatively adsorbing gas molecules such as  $H_2$  are expressed as

$$r_a = k_a C (1 - \Theta)^2 \quad (2)$$

$$r_d = k_d \Theta^2 \quad (3)$$

where  $k_a$  and  $k_d$  are the adsorption and desorption rate constants,  $C$  is the  $H_2$  gas concentration; and  $\Theta$  is the fraction of the surface sites occupied by the adsorbates. In the early stages of the gas injection,  $\Theta$  can be neglected, so the adsorption rate is linearly proportional to the  $H_2$  gas concentration and is gradually affected by  $(1-\Theta)^2$ . Thus, the initial reaction time is inversely proportional to the  $H_2$  gas concentration. The  $H_2$  gas sensing platform shows an inverse linear relationship between the  $H_2$  gas concentration and the gas response time at low  $H_2$  gas concentration, defined as the time at which the  $H_2$  gas concentration reaches 36.8 % ( $=e^{-1}$ ). The  $H_2$  gas sensing rate of the  $H_2$  gas sensing platform is dominantly influenced by  $H_2$  dissociative adsorption to the Pd layer, while the mass transfer effect to the sensing surface area is negligible. However, since the available surface for  $H_2$  gas adsorption is depleted, the  $H_2$  gas reaction time at  $H_2$  gas concentration higher than 100 ppm increases. This  $H_2$  gas reaction kinetics is also found in the relationship between the  $H_2$  gas reaction and concentration. At the equilibrium, or  $r_a$  is equal to  $r_d$ , the ratio of the occupied fraction of the surface sites to the non-occupied fraction is proportional to the square root of the  $H_2$  gas concentration, described as

$$\frac{\Theta}{1 - \Theta} = \sqrt{\frac{k_a}{k_d} C} \quad (4)$$

The  $H_2$  gas response of a suspended Pd-deposited glassy carbon nanowire shows a linear relationship with the square root of the gas concentration at low  $H_2$  gas concentration. Thus, the  $H_2$  gas reaction of the suspended Pd-deposited glassy carbon nanowire is also

closely related to the H<sub>2</sub> gas chemisorption.

The reproducibility of the H<sub>2</sub> gas sensing platform was measured by three successive cycles of the H<sub>2</sub> gas injection and N<sub>2</sub> purge at the constant concentration. Repeatability tests were performed in order of 50, 100, 500, and 30 ppm. Even with rapid H<sub>2</sub> gas concentration changes, the H<sub>2</sub> gas sensing platform shows the relatively good H<sub>2</sub> gas response reproducibility ( $\pm 2.14 - 8.0\%$ ).

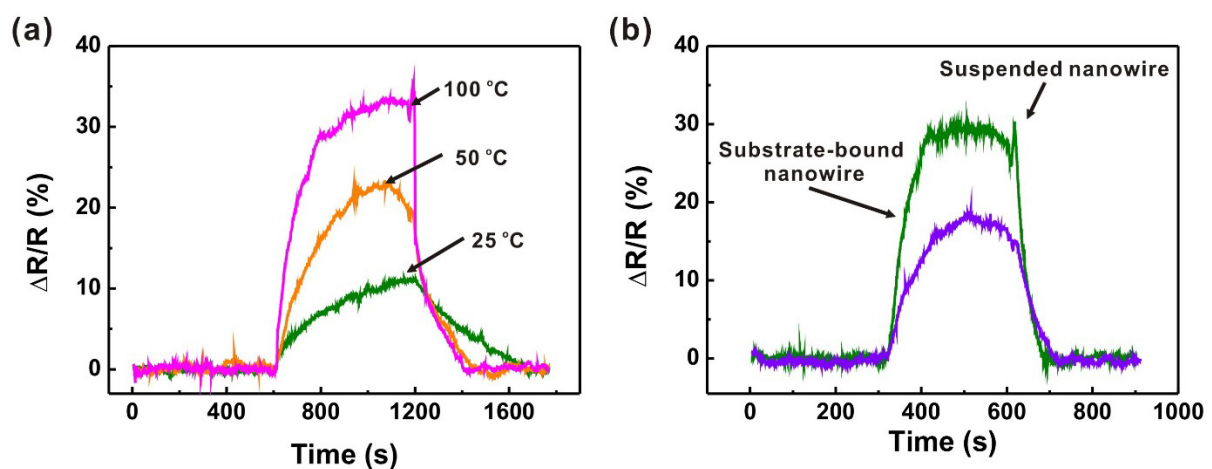


**Figure 2.9** (a) Gas sensing characteristics of the suspended Pd/carbon nanowire type the H<sub>2</sub> gas sensor for 50 ppm H<sub>2</sub> concentration at 25 (room temperature), 50, and 100 °C. (b) Comparison of the gas sensing characteristics at 50 ppm of H<sub>2</sub> gas between the suspended Pd/carbon nanowire and the substrate-bound Pd nanowire.

The effect of the measurement temperature on a H<sub>2</sub> gas sensing platform was characterized by comparing the H<sub>2</sub> gas response values at 25, 50, and 100 °C under 50 ppm H<sub>2</sub> in Figure 2.9 (a). The H<sub>2</sub> gas response increases as the measured temperature increase. However, since the internal diffusion of H<sub>2</sub> gas and the reaction rate change with temperature, the H<sub>2</sub> gas reaction time is reduced. The H<sub>2</sub> gas sensing platform at the room temperature exhibits a relatively good H<sub>2</sub> gas response of 11.0 %, which is about 31 % of the H<sub>2</sub> gas response at 100 °C.

1-D Pd nanostructures are advantageous for the fast detection at low H<sub>2</sub> gas concentrations due to fast gas absorption and high surface-to-volume ratios. Despite these advantages, the difficulty of the nanofabrication limits the application of nanostructures in the H<sub>2</sub> gas sensing platform. In contrast, the H<sub>2</sub> gas sensing platform was simply fabricated using a batch fabrication processes owing to the architecture of a suspended glassy carbon nanowire and SiO<sub>2</sub> eaves. The advantage of a suspended nanostructure of the H<sub>2</sub> gas sensing was evaluated by fabricating a Pd nanowire on the substrate and comparing their performance. Pd nanowires having a thickness of 100 μm, a width of 110 nm, and a thickness of 5 nm were patterned on 1-μm-thick SiO<sub>2</sub> deposited on a Si substrate. The dimensions of the substrate-bound Pd nanowires were selected to match the dimensions of the suspended nanowire. The H<sub>2</sub> gas-sensing capability of existing Pd deposited glassy carbon nanowires can not be directly compared with substrate-bound Pd nanowires. In the case of the former, the Pd layer contains a shell surrounding the electrically conductive glassy carbon nanowire core. However, since the thickness of the Pd layer is much smaller than the diameter of the glassy carbon nanowires, the surface-to-volume ratio of the suspended Pd-deposited glassy carbon nanowire could be approximated to the surface-to-volume ratio of the Pd nanowires on the substrate. It can also be assumed that the H<sub>2</sub> gas response of the suspended Pd-deposited glassy carbon nanowires is determined by the Pd material shell because the electrical properties of the glassy carbon nanowires are much greater than the electrical properties of the Pd layer shell. The H<sub>2</sub> gas response of the suspended Pd-deposited glassy carbon nanowires was 64.6 % higher with shorter reaction times and recovery times than with substrate-bound Pd nanowires. It is believed that the enhanced performance of the suspended Pd-deposited glassy carbon nanowires is due to convective enhancement and the transfer of the circumferential material to the stagnant nanowire and the reduction of the effect of the stagnation layer.

# 3

## Suspended ZnO NWs/glassy carbon nanowire

*In this chapter, a suspended ZnO NWs/glassy carbon nanowire will be introduced to apply the gas sensing platform. Also, fabrication steps and material property will be given.*



### 3 Suspended ZnO NWs/glassy carbon nanowire

#### 3.1 Background

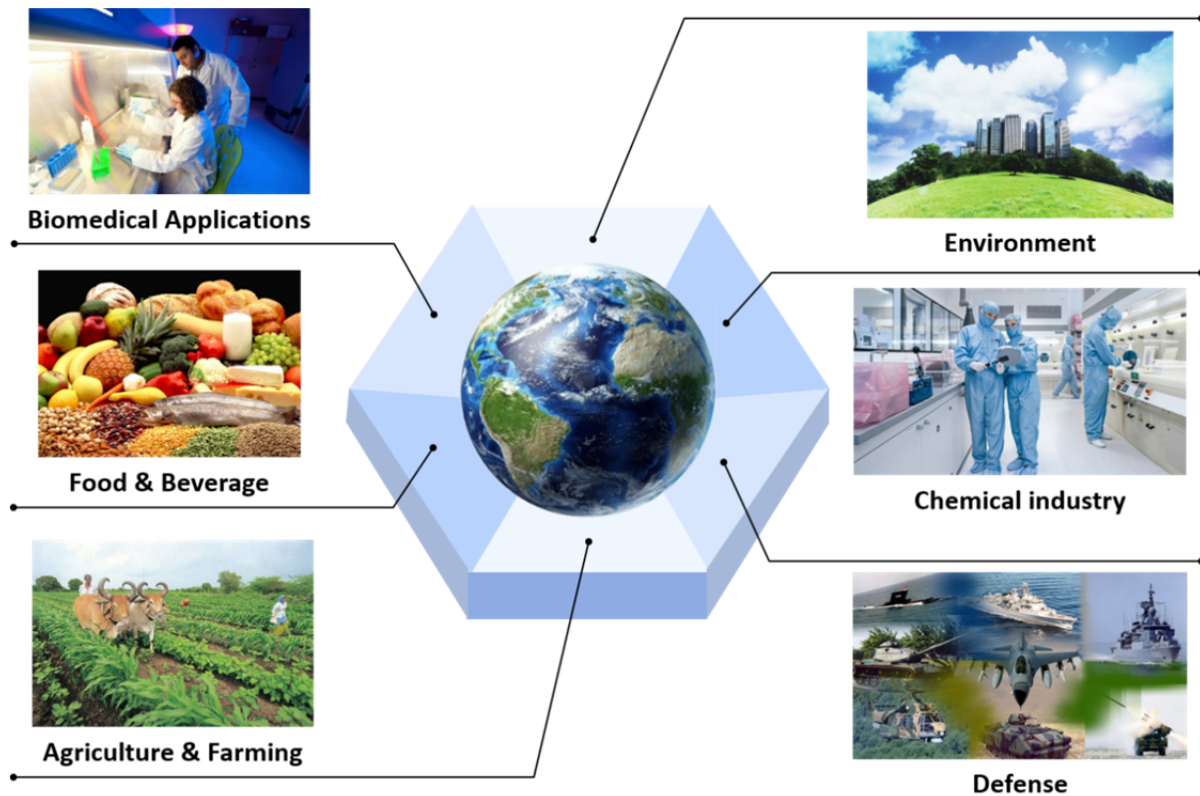


**Figure 3.1** Needs to gas sensing platform at various field such as biomedical, food & beverage, agriculture & Farming, environment chemical industry, and military defense.

The Pd material is a highly selective  $H_2$  gas sensing material. Over the last decade, however, there has been an increasing demand for chemical and gas sensing platform in many applications, including biomedical applications, food & beverage safety, environmental monitoring, the chemical industry and military defense systems [78-82]. The gases of interest are  $CH_4$ ,  $CO$ ,  $H_2$ ,  $H_2S$ ,  $NO_2$ ,  $SO_2$  and various volatile organic compounds (VOCs) such as acetone, benzene, ethanol, methanol and toluene. Some gases are harmful and hazardous in parts-per-million (ppm) due to their toxicity, corrosiveness, and noxious effects [83-85].

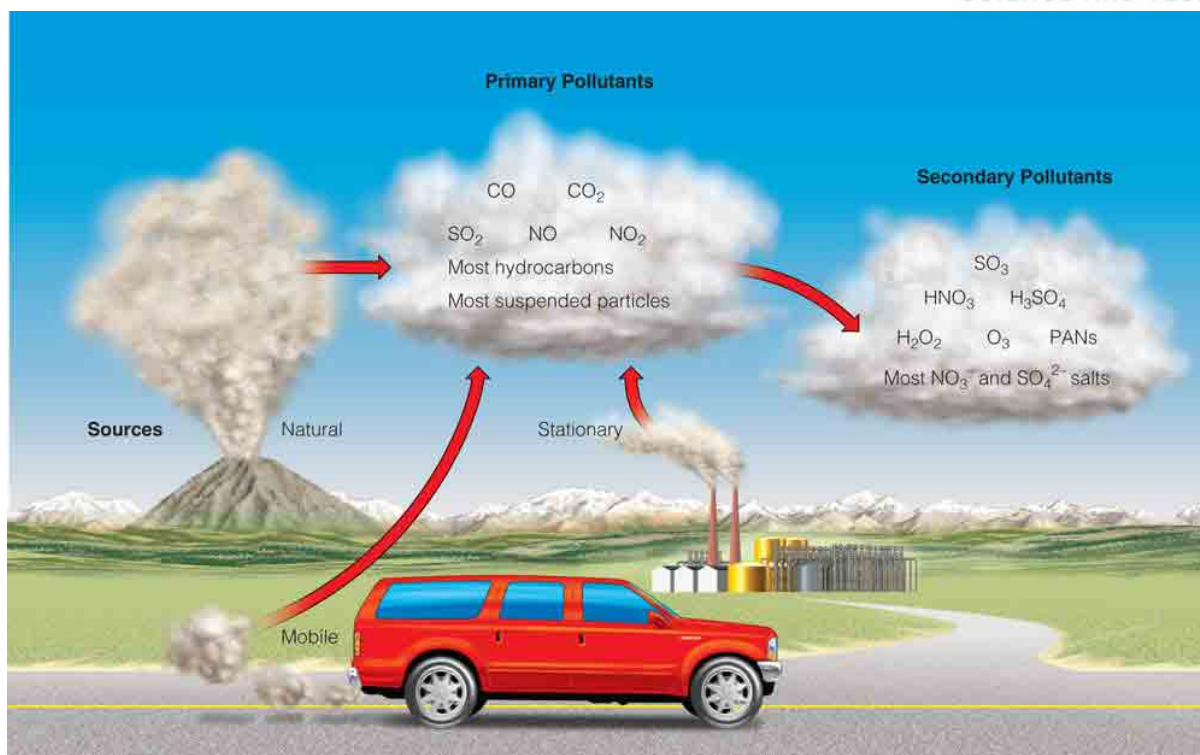


**Figure 3.2** Some primary air pollutants react with other chemicals in the air to make secondary air pollutants.

Depending on the nature of the gas, there are two type pollutants; primary and the secondary pollutants [86-88]. The primary pollutants are directly affected air pollutants such as H<sub>2</sub>S, NH<sub>3</sub>, CO<sub>2</sub>, SO<sub>2</sub>, NO, petroleum steam, diesel, kerosene, liquefied petroleum gas (LPG), dust particles etc., and then, the secondary pollutants are affected indirectly such as NO<sub>2</sub>, SO<sub>3</sub>, O<sub>3</sub>, ketones, sulfuric acid (H<sub>2</sub>SO<sub>4</sub>) etc. Exposure to toxic and noxious gas contaminants could be affected by heart and respiratory diseases, lung cancer, decreased hemoglobin, nervous system damage, mental retardation, digestive and reproductive system impairments, blindness, forgetfulness and hypertension etc [89-93]. Leakages of these pollutants can cause serious health problems if they reach a critical level of up to 100 ppm [86-87]. Therefore, the gas sensor needs to improve the gas sensitivity and selectivity. Lower limit of detection (LOD) and high gas selectivity are notable performances in gas sensing platforms with long term use and stable chemical and thermal properties over time, gas

sensitivity, low power consumption, fast gas response and recovery time [94-97]. Current social requirements for the gas sensing platforms are for small, low-cost, portable and easy-to-use gas sensors with wireless connectivity [98].

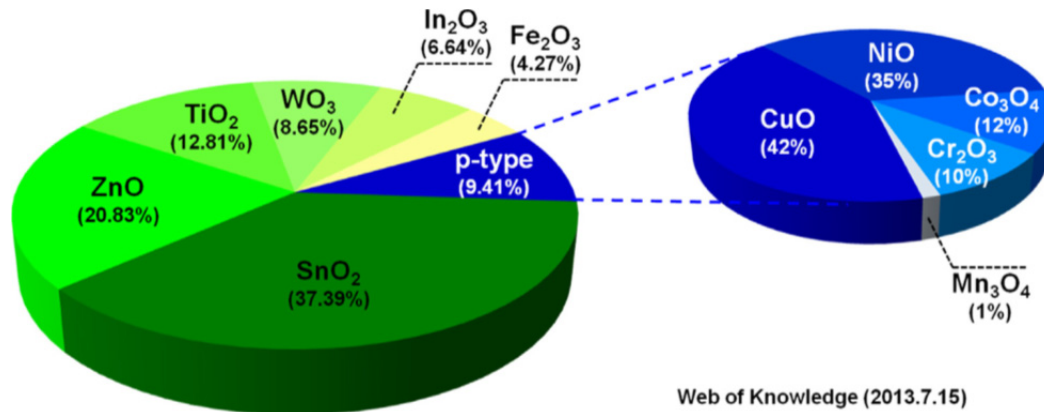


**Figure 3.3** Researches on n-type and p-type metal oxide semiconducting nanostructure for use as the gas sensor from H. Kim et. al. [99].

Metal oxide based gas sensing platforms are ideal for overcoming the social needs of gas sensing platforms [100-104]. The operating principle of the metal oxide based gas sensing platform is based on the reduction of the ambient or the change in electrical properties depending on the oxidizing gas concentration. Metal oxide based gas sensing platforms have many advantages such as fast gas sensing response, simple implementation, low cost and stable chemical and thermal characteristics for long term use. Nonetheless, there are still some problems with metal oxide-based gas sensing platforms, such as high operating temperatures of over 200 °C and above and long operating times of gas sensing response and recovery [105-107]. High operating temperatures would cause significant operating hazards and limited use when gas detection is not suitable for the green energy community. Despite the high operating temperature, metal oxide based gas sensing platforms have long been developed due to the advantages of fast gas sensing response time [108]. Fast gas detection time is important for users to detect warning alarms in advance of hazardous gas exposure

[109-111]. To effectively expose ambient gases to metal oxides, previously dominant metal oxide films have been developed by nanowires, nano-flakes or nanoparticles, and larger surface to volume ratios could improve gas sensing response and recovery times owing to the larger surface-to-volume ratio in the nano-structure. Although some researchers have developed for a variety of nano-structures based on the metal oxides, it is difficult to predict a larger surface-to-volume ratio in the metal oxide nano-structures. This is because there is a dead surface area in the substrate-bound structure that does not surrounds the gas.

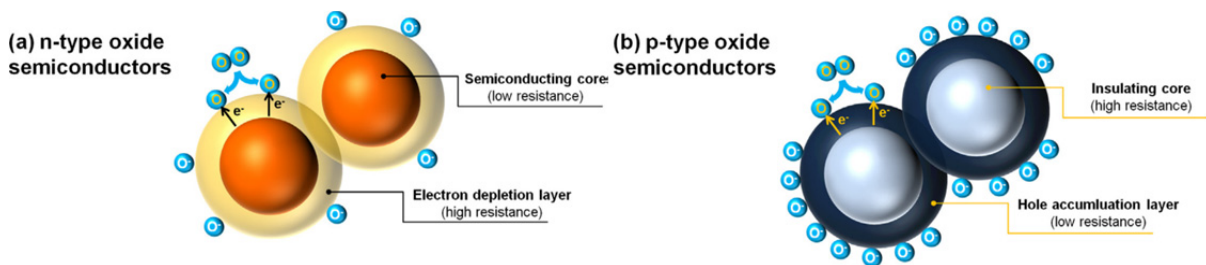


**Figure 3.4** Gas sensing mechanisms of electronic core-shell structures in (a) n-type and (b) p-type metal oxide semiconducting nanomaterials from H. Kim et. al. [99].

Hierarchical nanowires have a high aspect ratio in the form of metal oxide nanowires in the field of the gas sensing. The surface area of the layered metal oxide nanowires formed in the substrate-bounded structure is smaller than the theoretical surface area of the layered metal oxide nanowires because of the dead surface area between the layered metal oxide nanowires and the substrate [114].

However, the hierarchical metal oxide nanowires formed in the suspended structure have higher gas sensing properties than the substrate-bound structure because the dead surface area of the hierarchical metal oxide nanowires in the suspended structure is smaller than that of the substrate-bound structure. In addition, the ambient gas is more affected by the suspended structure due to the no-slip condition at the bottom of the substrate. There are many advantages to stationary structures, but it is difficult to create suspended

structures without expensive nano-fabrication such as e-beam lithography and FIB milling [115-116]. Metal oxide nanowires for the gas sensing platforms using a suspended structure have been developed in two type; metal oxide nanowires networked between two electrodes and hierarchical metal oxide nanowires randomly deposited in the posts [114, 117]. Two types of hierarchical metal oxide nanowires have high gas sensing properties, but wafer level fabrication for gas sensing platforms is difficult. Carbon-MEMS is a wafer level batch fabrication process consisting of the photolithography and the pyrolysis. Suspended carbon nanowires made from the carbon-MEMS have high young's modulus, monolithic structure and longitudinal tensional stress [4, 118].

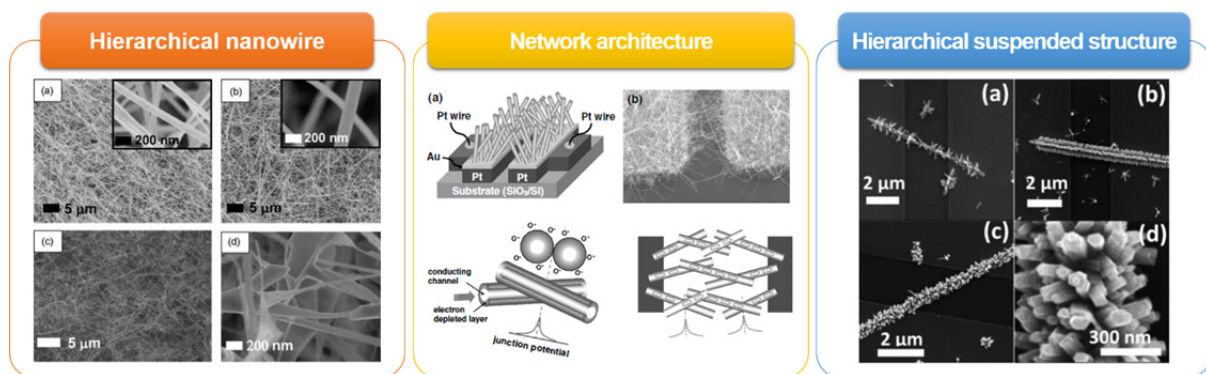


**Figure 3.5** Categorization of gas sensing platform based on semiconducting nanowire to enhance the gas sensing response such as hierarchical nanowire from Y. Zhang et. al.[112], network architecture from Y. Choi et. al.[113], and hierarchical suspended structure from M. R. Alenezi et. al.[114].

In this study, we developed a highly sensitive gas sensing platform based on the hierarchical ZnO nanowires grown in the circumferential direction of the suspended glassy carbon nanowires. We fabricated the suspended glassy carbon nanowires by the carbon-MEMS and fabricated the hierarchical ZnO nanowires forests using the hydrothermal method consisting of the seed layer process and the growth process. For selective deposition processes, a stepped photoresist patterning process was carried out using the positive

photoresists in the suspended glassy carbon nanowires for the selective open. After the selective deposition process, the growth process proceeds, the photoresist is removed, and the selective ZnO nanowires forests are grown on the suspended glassy carbon nanowires. In order to increase the effect of the gas sensing material of the ZnO nanowires forests on the suspended glassy carbon nanowires, the electrical properties of the suspended carbon nanowires were modulated by the controlling the pyrolysis conditions of the temperature. The electrical resistance was linearly changed with the concentration of the surround gases.

### 3.2 Fabrication & Experimental

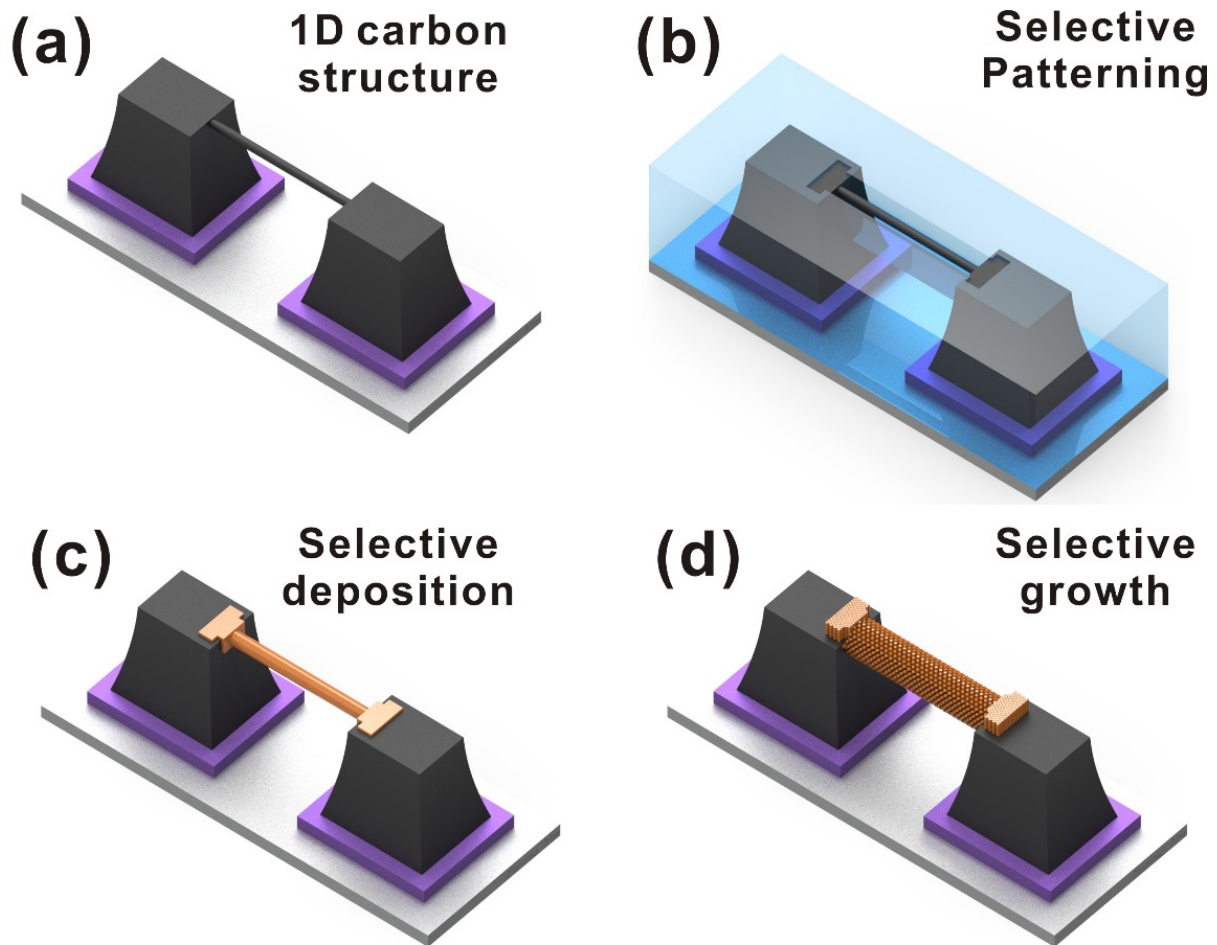


**Figure 3.6** Fabrication steps for hierarchical ZnO nanowires forests grown on a suspended single glassy carbon nanowire for use as gas sensing platforms.

The fabrication steps for a ZnO nanowires forests grown circumferentially on the suspended glassy carbon nanowire are illustrated in Figure 3.6 and 3.7. Before the fabricating glassy carbon structure, 1- $\mu\text{m}$ -thick  $\text{SiO}_2$  layer was grown on a 6-inch Si wafer (p-type, boron, 5-20  $\Omega\cdot\text{cm}$ , 660 – 700  $\mu\text{m}$  thick; LG Siltron Co., Ltd., Republic of Korea) using the wet oxidation process. The  $\text{SiO}_2/\text{Si}$  substrate was cleaned in a hot piranha solution ( $\text{H}_2\text{SO}_4 : \text{H}_2\text{O}_2 = 4 : 1$ ) and a dehydration process was performed on a hot plate at 200  $^\circ\text{C}$  for 5 min. The negative photoresist of 45- $\mu\text{m}$ -thick (SU-8 2050, MicroChem. Corp., USA) was coated using

the spin-coating machine on the SiO<sub>2</sub>/Si substrate and soft-baked at 95 °C for 10 min, a coated negative photoresist layer was exposed to a UV dose (230 mJ cm<sup>-2</sup>) to make the post structures that support a suspended negative photoresist microwire. A second UV exposure of a low UV dose (16 mJ cm<sup>-2</sup>) was performed to selectively polymerize between the pre-exposed post structures. A suspended negative photoresist microwire structure was formed by the development process after the post-exposure bake process. A suspended negative photoresist microwire structure was converted into a suspended glassy carbon nanowire structure using the polymer pyrolysis process owing to the high volume decreasing ratio. ZnO nanowire was made by the autoclave process consisting of the seed process and the growth process. Before the ZnO seed layer deposition process, a positive photoresist of 14-μm-thick (AZ 4330, AZ Electronic Materials, USA) was coated on these substrate to the selective open. To selective deposit the ZnO seed layer on a suspended glassy carbon nanowire, a positive photoresist layer was exposed to a low dose (50 mJ cm<sup>-2</sup>) for selective be etched by the developing solution. After the development process, a positive photoresist was covered without a suspended glassy carbon nanowire. The ZnO layer of 20-nm-thick was deposited on a selective suspended glassy carbon nanowire and a positive photoresist using the rf-sputtering process (SRN-120, Sorona Co., Ltd., Republic of Korea) and a positive photoresist was removed using the acetone (J.T. Baker Chemical Co., Ltd., USA). The growth process was made in 10 mM zinc nitrate hexahydrate (Zn(NO<sub>3</sub>)<sub>2</sub> · 6H<sub>2</sub>O) with 10 mM hexamethylene tetramine ((CH<sub>2</sub>)<sub>6</sub>N<sub>4</sub>) using the autoclave system owing to high pressure and higher temperature better than water evaporation degree of 100 °C.

Microstructures of a circumferentially grown hierarchical ZnO nanowires forests on a suspended glassy carbon nanowire were characterized using the X-ray diffraction measurement (XRD, D/MAX2500V/PC, Rigaku Co., Japan), the SEM (Quanta 200, FEI Company, USA) and HRTEM (JEM-2100F, JEOL Ltd., Japan). To characterize the crystal



structure by the XRD measurement, hierarchical ZnO nanowires was grown on the carbon/quartz substrate to remove the single crystal peak generated by the SiO<sub>2</sub>/Si substrate. TEM samples of a circumferentially grown hierarchical ZnO nanowires forests on a substrate-bound glassy carbon nanowire were prepared using a FIB milling machine (Helio 450HP, FEI company, USA).

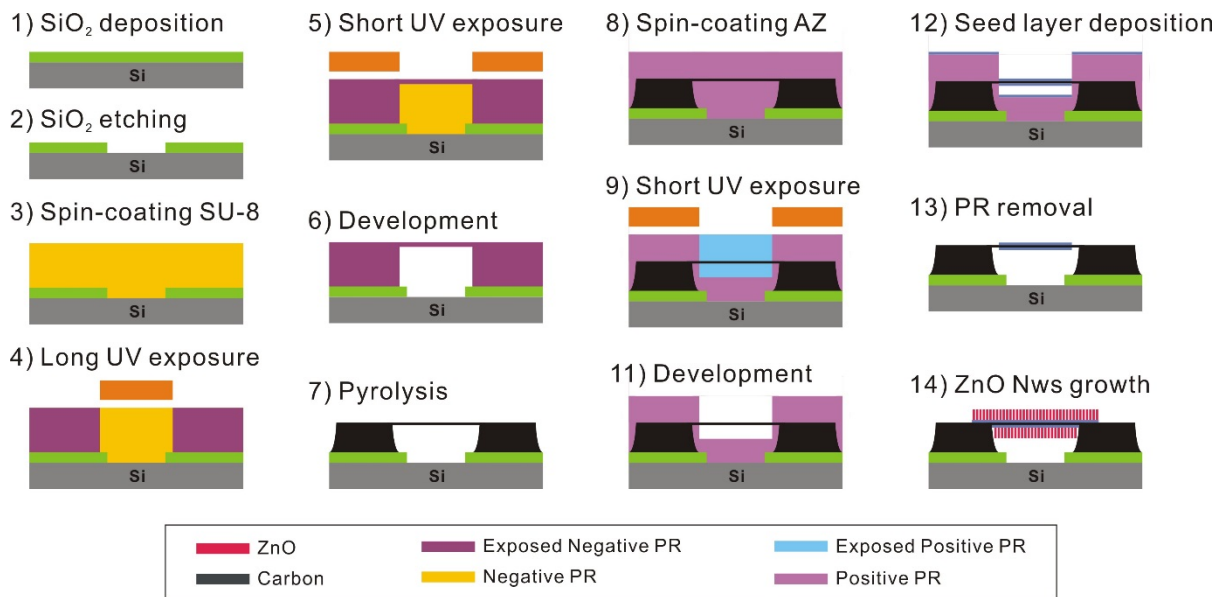


**Figure 3.7** Steps for fabricating a suspended ZnO nanowires forests/glassy carbon nanowire to apply to the gas sensing platform.

Various gas detection responses such as NO<sub>2</sub>, CO, H<sub>2</sub>, SO<sub>2</sub>, C<sub>6</sub>H<sub>6</sub> and CH<sub>4</sub> were measured at atmospheric pressure in a chamber. Before the gas detection, the chamber was purged by several vacuum pumping and N<sub>2</sub> gas purging cycles. Gas concentrations were controlled by mixing 0.1 % concentration and N<sub>2</sub> using a gas flow meter (GMC 1200, ATOVAC, Republic of Korea). The electrical resistance change was characterized using a source meter (Keithely 2401, Keithley Instruments, Inc., USA) in various gas concentration with N<sub>2</sub> gas.

### 3.3 Results & discussion

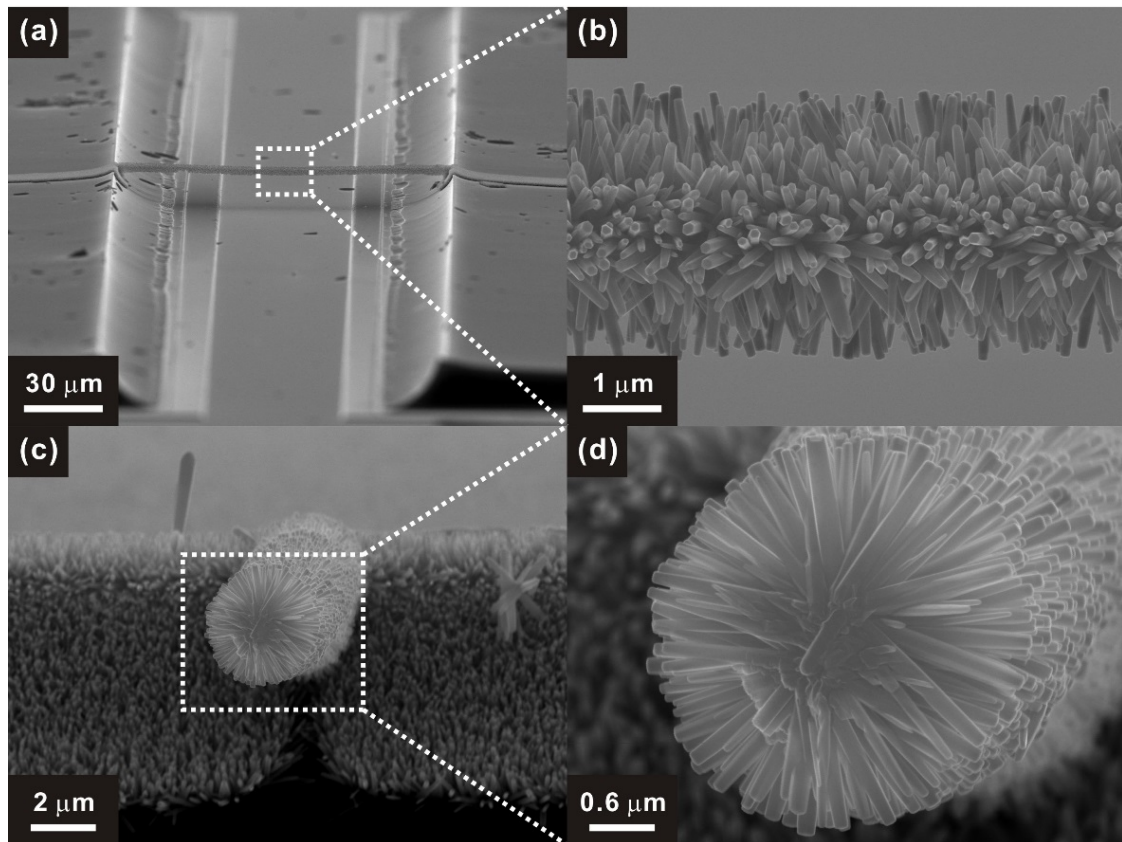


**Figure 3.8** SEM images of the hierarchical ZnO nanowires forests grown on selectively the suspended single glassy carbon nanowire; (a, b) bird-view, (c, d) cross-section view.

Hierarchical ZnO nanowires forests have grown perfectly and circumferentially and selectively on the suspended glassy carbon nanowire without the bottom surface of the Si substrate. The diameter and length of hierarchical ZnO nanowires forests are about 50 ~ 70-nm-width and 1.1 ~ 1.5- $\mu\text{m}$ -length on a suspended glassy carbon nanowire of 150-nm-diameter and 119.5- $\mu\text{m}$ -length. The hybrid structure of a hierarchical ZnO nanowires forests grown circumferentially on a suspended glassy carbon nanowire is expected to improve the gas sensing platform with a high density of hierarchical ZnO nanowires forests. As described in the experimental section, the ZnO layer was selectively deposited on a suspended glassy carbon nanowire. The etched  $\text{SiO}_2$  area on the  $\text{SiO}_2/\text{Si}$  substrate served to remove the ZnO

nanowire particles made by the growth process.

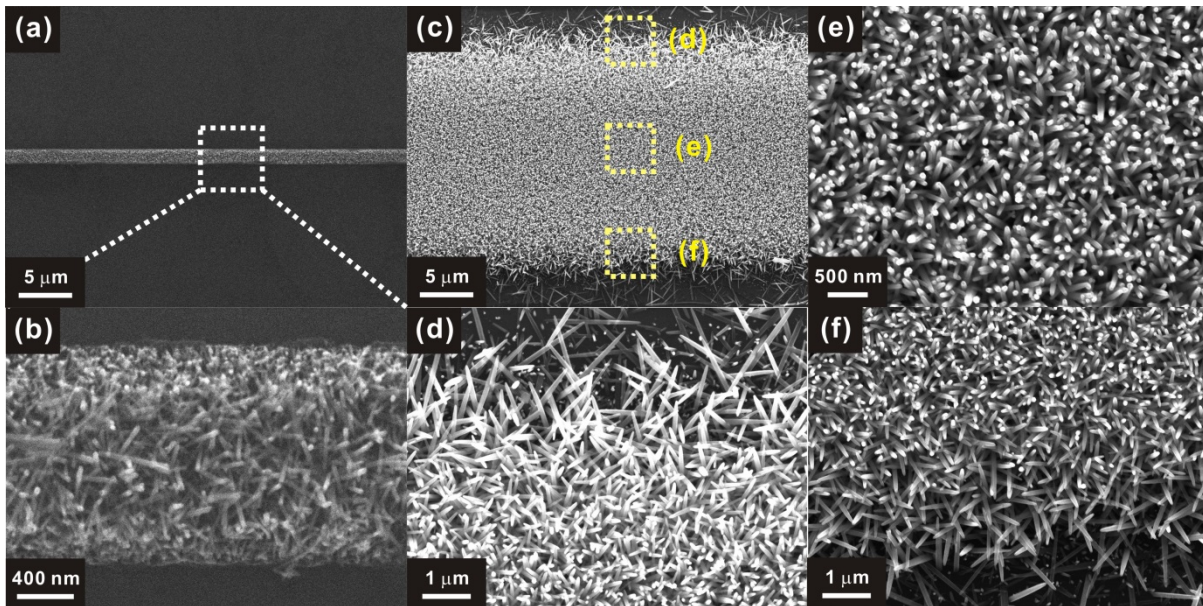


**Figure 3.9** SEM images of substrate-bound ZnO nanowires forests grown on (a, b) a 1- $\mu\text{m}$ -width and (c-f) a 20- $\mu\text{m}$ -width ZnO seed lines. The seed lines are 100- $\mu\text{m}$ -length.

ZnO nanowires were grown on the substrate to characterize the effect of the geometric characteristics of the ZnO nanowires forests grown between the suspended structure and the substrate-bound structure. As described in the previous paragraph, ZnO nanowires are selectively aligned over 1D carbon nanostructures without the need to rely on very precise alignment because the alignment accuracy is determined by the carbon nanowire length, not by width. However, due to limitations in alignment accuracy, it is almost impossible to produce substrate-bound carbon nanowires selectively coated with ZnO nanowires forests. Instead, we created a ZnO nanowires forests grown on the substrate without a carbon nanowire backbone. First, a ZnO seed layer is patterned in the form of a line (length = 100  $\mu\text{m}$ ) on the substrate and then ZnO nanowires are grown using the same hydrothermal process as the suspended ZnO nanowires forests as shown in Figure 3.9. The growth pattern of ZnO nanowires forests depends on the lateral position of the ZnO seed line.

At the 20- $\mu\text{m}$ -width ZnO seed line, the nanowires were grown vertically and firmly in the middle of the seed line, as shown in Figure 3.9 (e). On the other hand, ZnO nanowires grow radially and less dense at the edge of the seed line, as shown in Figure 3.9 (d, f). This position-dependent growth pattern is due to the fact that the diffusion of hydrothermal solution occurs vertically in the middle region of the seed layer and radial diffusion occurs at the edge parts. This radial diffusion is dominant over a narrow ZnO seed layer (width = 1  $\mu\text{m}$ ), so that the portion of ZnO nanowires grown radially increases. Thus, the overall ZnO nanowires forests are formed less tightly, allowing for better gas accessibility. As described in the fabrication section, the Si substrate was exposed underneath the suspended nanowire. Thus, the hydrophobicity of the Si substrate prevented spontaneous precipitation of ZnO nanostructures produced in the bulk growth solution.

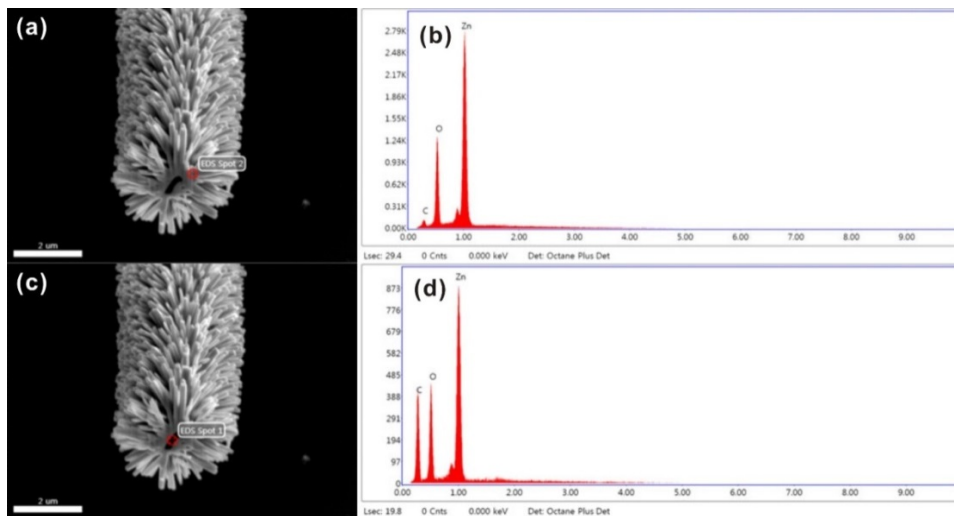


**Figure 3.10** Point chemical analysis spectrum acquired from a suspended ZnO nanowires forests/glassy carbon nanowire; (a, b) ZnO nanowires grown on a suspended glassy carbon nanowire, (c, d) core glassy carbon nanowire.

The chemical composition of ZnO nanowires grown on the suspended carbon nanowire was characterized using EDS as shown in Figure 3.10. According to the EDS data, ZnO nanowires consist mainly of zinc (Zn) and oxygen (O) in a ratio of 1:1. The carbon

composition significantly increases in the cores of the ZnO nanowires forests with carbon nanowire embedded therein.

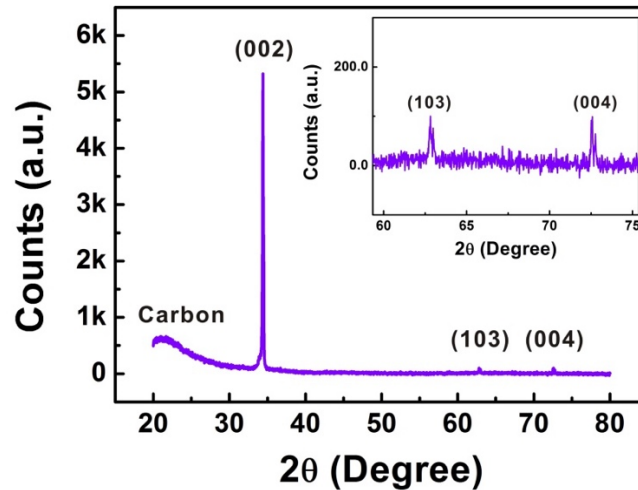


**Figure 3.11** XRD pattern of ZnO nanowires grown on a glassy carbon structure using hydrothermal method.

Conventional XRD measurements based on theta-2theta method were performed to confirm that the aligned ZnO nanowires on the glassy carbon structure were orientated in the c-axis. The diffraction peaks could be easily indexed into a hexagonal crystal structure of the wurtzite structure having a cell constants ( $a = 0.325$  nm,  $c = 0.521$  nm; JCPDS card : 00-036-1451) [119]. A small but negligible diffraction peak was found along the direction (103), which shows some deviation from the c-axis. The full width half maximum (FWHM) of the diffraction peak in the direction of (002) and the ratio of (002)/(103) are  $0.125^\circ$  and 53.25 respectively. In the ZnO crystals, the growth rates are  $[0001] > [01\bar{1}1] > [01\bar{1}0] > [000\bar{1}]$  in the hydrothermal growth process [120]. In addition, the HMTA plays an important role in helping the heterogeneous growth of ZnO nanowires on the ZnO nucleation surface [121-125]. Because the crystal growth rate of ZnO nanowires is different, the crystal growth of ZnO nanowires is affected by the substrate though the ZnO materials are an anisotropic crystal structure [126-128]. As the glassy carbon structure with a hexagonal carbon structure,

ZnO nanowires grown on a glassy carbon structure have a large c-axis crystal growth direction. The diffraction pattern represents two peaks with higher intensities of (002) and (004) which are multiples of the c-axis growth direction of the ZnO materials. In addition, peaks from impurities such as Zn are not detected in the diffraction pattern and exhibit high purity products.

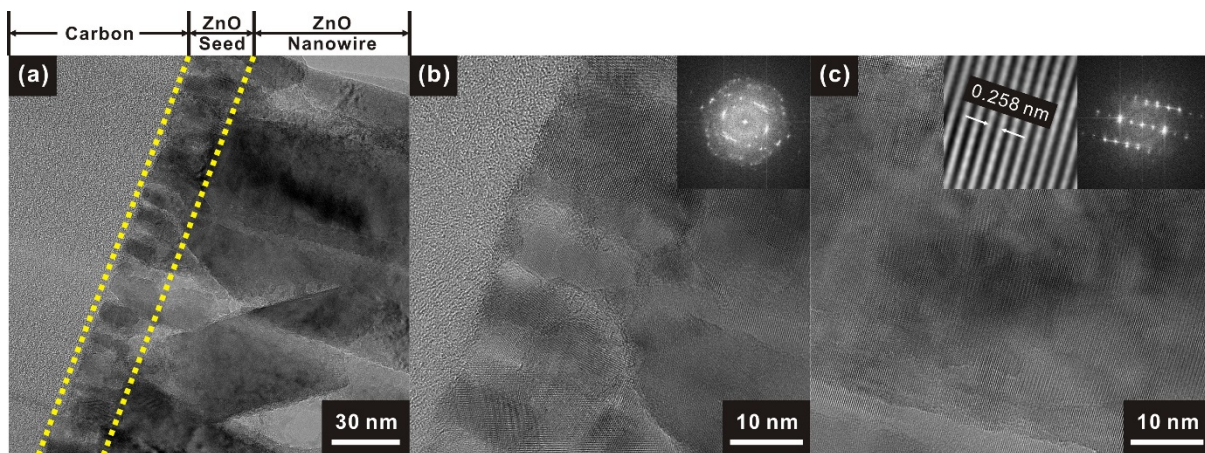


**Figure 3.12** TEM analysis of a ZnO nanowires/ZnO seed layer/carbon structure. (a, b) HREM images of (b) ZnO seed layer and (c) ZnO nanowire inserted the diffraction pattern and inverse FFT image.

Figure 3.12 shows the TEM image taken from the ZnO nanowires forests/ZnO seed layer/carbon/SiO<sub>2</sub>/Si sample prepared using the FIB milling. The ZnO nanowires have a structurally homogeneous and complete single crystal structure because the ZnO crystal lattice is well oriented in the part of the ZnO nanowires. Figure 3.10 (b) shows the HRTEM image showing that the ZnO nanowires are the wurtzite crystal structure referred the JCPDS card (00-036-1451). The interplanar spacing at the crystalline plane is 0.258 nm, which represents the distance between (002) planes and shows excellent growth along the [0002] direction of the c-axis. The ZnO seed layer prepared by the rf-sputtering method has a part between the amorphous part and the single crystal part. As described in Figure 3.8 (b), the

hydrothermal method for ZnO nanowires growth does not require an annealing process after the seed layer deposition process because the amorphous phase is converted into a crystalline phase in the ZnO nanowires growth process, so the substrate is important to grow the ZnO nanowires. Since the glassy carbon structure fabricated using carbon-MEMS has a short-range ordered crystal structure and a hexagonal structure, there is almost no discrepancy between the ZnO nanowires and the glassy carbon structure, so the high aspect ratio of ZnO is influenced by the glassy carbon structure.

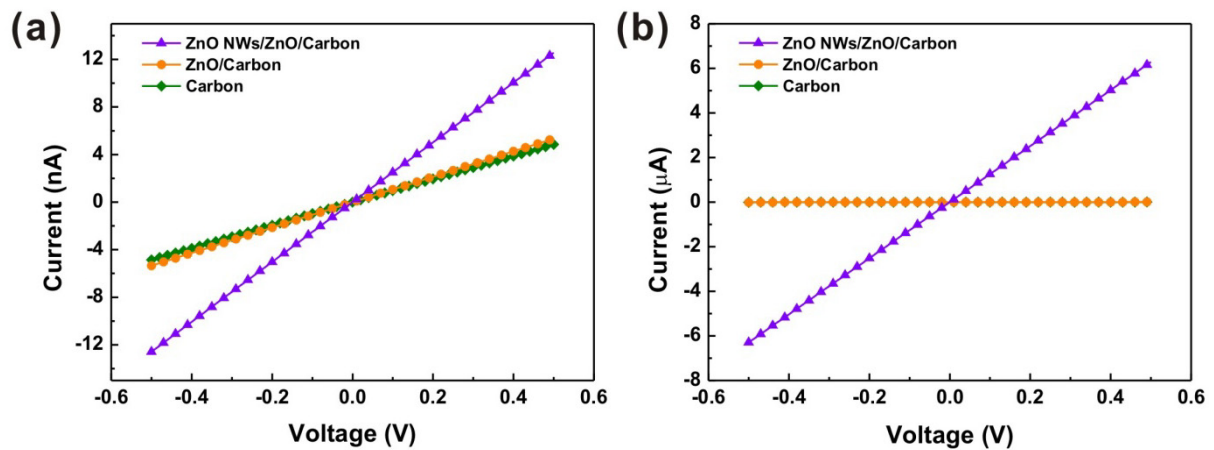
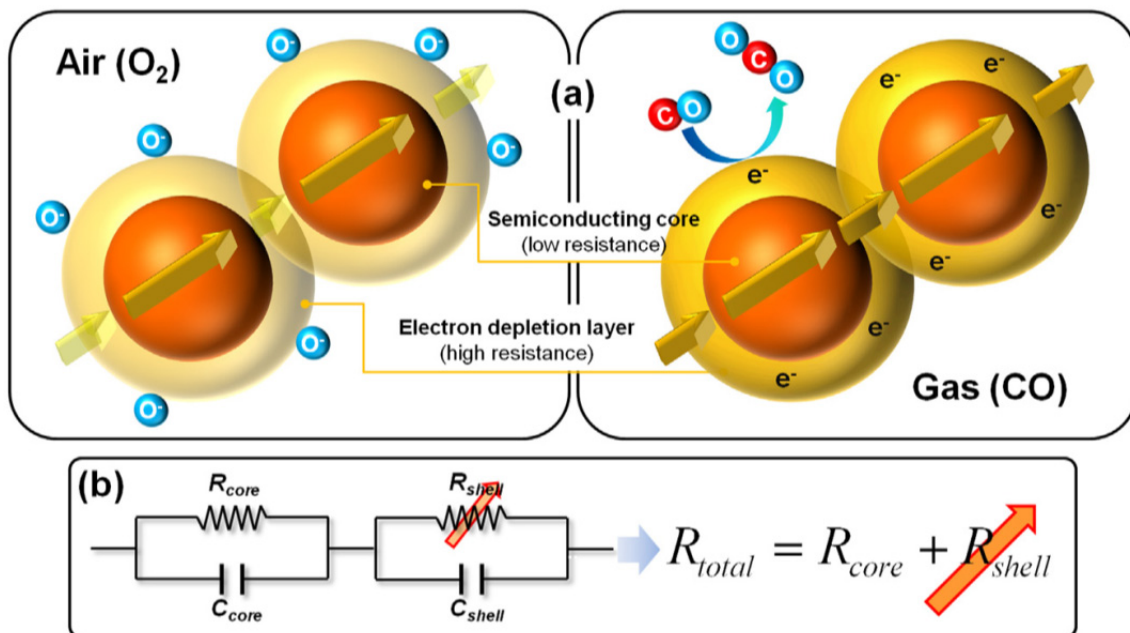


**Figure 3.13** I-V characteristics of ZnO nanowires grown on a suspended single carbon nanowire (olive line : carbon nanowire, orange line : ZnO seed layer/carbon nanowire, violet line : ZnO nanowires/ZnO seed layer/carbon nanowire) at (a) room temperature and (b) 200 °C.

The electrical characteristics of a ZnO nanowires forests grown circumferentially on a suspended carbon nanowire are showed at Figure 3.13. Suspended carbon nanowires have the ohmic contacts measured by the I-V characteristics. Because the electrical conductivity of the glassy carbon structure made by the carbon-MEMS is affected by the polymer pyrolysis conditions of the temperature, the electrical resistance of the suspended carbon nanowires is increased for the application of ZnO nanowires-based gas sensing

platforms [129]. After the ZnO seed layer was deposited selectively on a suspended carbon nanowire at 20-nm thickness using the rf-sputtering process, there is not change at the I-V characteristics. After the ZnO nanowires growth process based on the hydrothermal method, the electrical resistance was decreased at 2.4 times at room temperature. There is a slight difference between the ZnO nanowires and the glassy carbon nanowire, but the metal oxide based gas sensing platform would be applied because of the large electrical resistance at 200 °C, as shown in Figure 3.13. This change in ZnO nanowire growth induction resistance increased to ~ 320 times at the gas sensing temperature (200 °C), as shown in Figure 3.13 (b). Therefore, it would be assumed that the influence of glassy carbon nanowires on gas sensing is negligible. In addition, when the electrical resistance decreases dramatically after ZnO nanowires growth, the nanowires grown in the circumferential direction are well interconnected along the suspended carbon nanowires.



**Figurer 3.14** Gas sensing mechanisms and equivalent electrical circuit based on n-type metal oxide semiconducting materials from H. Kim et. al. [99].

The main charge-transfer mechanism of Si-based semiconductor materials can be



manipulated by appropriate doping of donor or acceptor. On the other hand, the main charge carriers are either doped with alkali cations in the wide bandgap oxide based semiconductor material or determined in an oxygen non-stoichiometric manner [130]. The concentration of charge carriers in semiconductor materials used in the gas sensing platform can be changed or adjusted to the appropriate range at the sensing temperature to achieve a high gas response and to control the electrical properties of the semiconductor material. The doping can be used to control the major charge carrier concentration of the gas sensing material since the oxygen non-stoichiometry can not be changed at a fixed operating temperature [131-132].

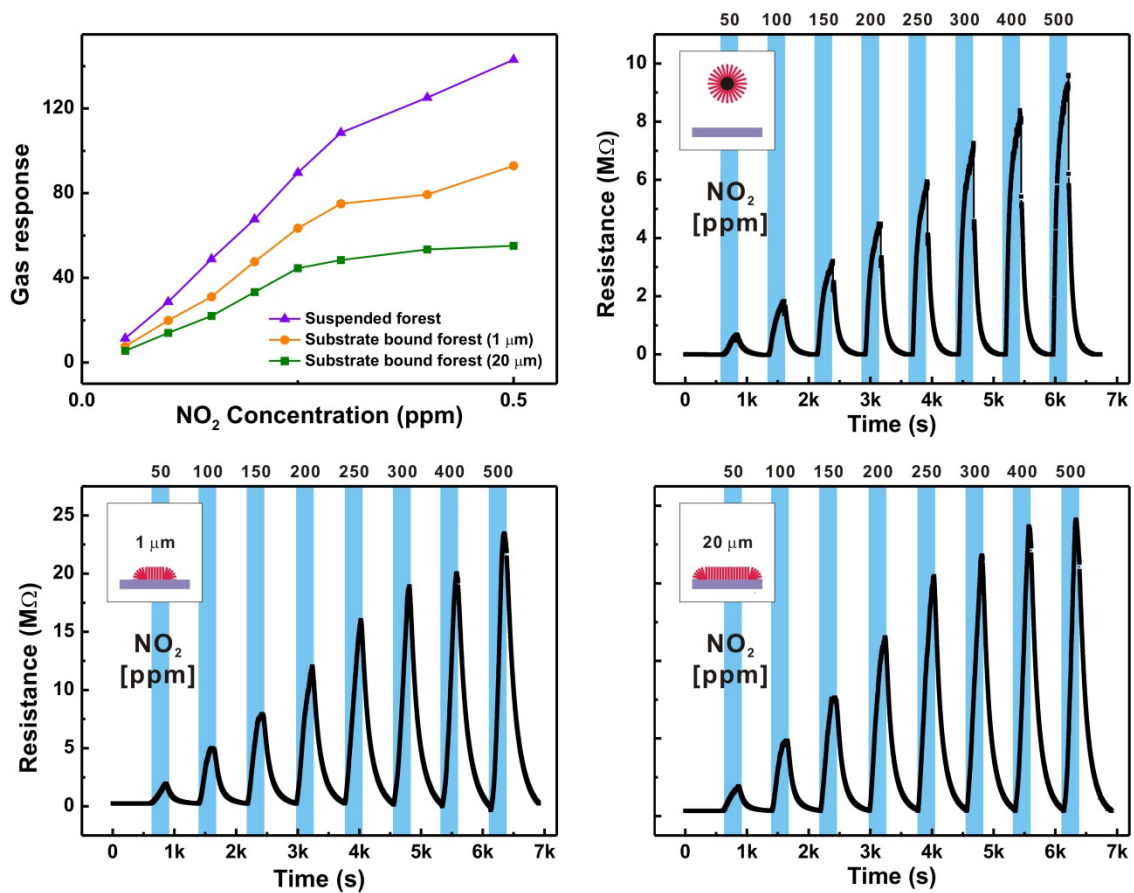


**Figure 3.15** (a) Gas responses at various NO<sub>2</sub> concentrations of the suspended ZnO nanowires forests and substrate-bound ZnO nanowires forests. Resistance changes at various NO<sub>2</sub> concentrations of (b) the suspended ZnO nanowires forests and substrate-bound ZnO nanowires forests grown on (c) a 1-μm-width and (d) a 20-μm-width pads.

Oxygen molecules in semiconductor materials adsorb to the surface of n-type metal oxide semiconductor materials such as SnO<sub>2</sub> and ZnO and ionize into oxygen species by taking electrons near the surfaces [133-134]. It is known that the adsorption species of oxygen ion is dominant at less than 150 °C, between 150 and 400 °C, and over 400 °C [134]. This principal for the formation of an electronic core-shell structure; an n-type semiconductor region in the particle core, and an electrical resistance in the shell. Although the n-type metal oxide semiconductor material forms an electric core-shell layer adsorbed by oxygen, its conduction characteristics are significantly different. The electrical resistance of the n-type metal oxide semiconductor materials is mostly determined by the electrical resistance shell-shell contact formed between the particles in the n-type metal oxide semiconductor material. Therefore, an equivalent circuit could be described as an electrical series connection between a semiconductor core ( $R_{\text{core}}$ ) and a resistive inter-particle contact ( $R_{\text{shell}}$ ) [135-138].

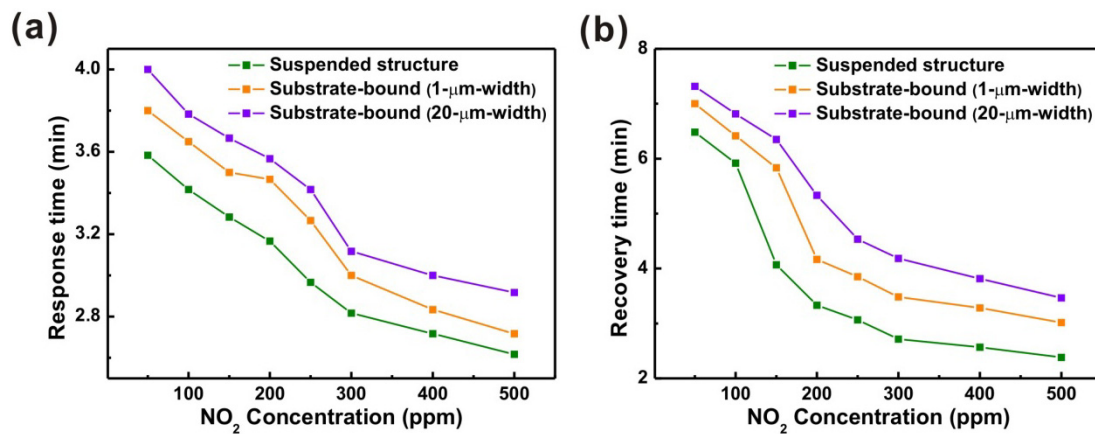
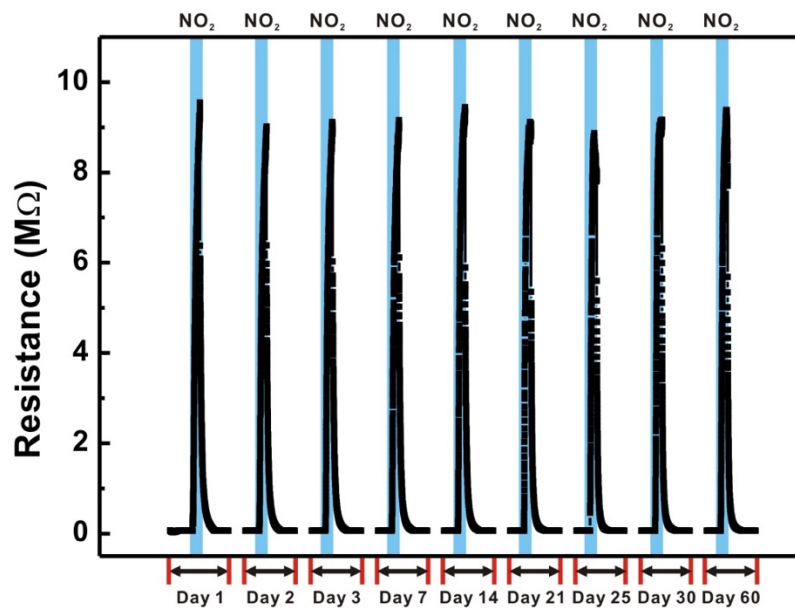


**Figure 3.16** (a) Gas responses of a ZnO nanowires forests/carbon nanostructure versus various concentrations of NO<sub>2</sub>. (b) Response time and recovery time versus various NO<sub>2</sub> gas concentrations.

When a gas sensing platform based on an n-type metal oxide semiconductor material is exposed to a reducing gas (CH<sub>4</sub>, CO, H<sub>2</sub>, SO<sub>2</sub>, C<sub>6</sub>H<sub>6</sub>), an ionized anion such as O<sup>2-</sup>, O<sup>-</sup> and O<sup>2-</sup> is injected into the core from the semiconductor material to reduce the electrical

conductivity in proportion to the concentration of the reducing gas. Thus, the high gas response to the transfer concentration of the reducing gas in the n-type metal oxide semiconductor material is due to a significant change in the chemical resistance between the particles. In contrast, when the gas sensing platform is exposed to oxidizing gas ( $\text{NO}_2$ ), the ionizing anion reacts in the reduction mechanism and the electrical carrier is reduced due to the reduction mechanism.



**Figurer 3.17** Long term stability of the gas sensing platform based on ZnO nanowires forests grown on a suspended carbon nanowire: the gas response and recovery behaviors for 500 ppb  $\text{NO}_2$  were tested in the period of 60 days.

Gas sensing properties of a gas sensing platform based on the ZnO nanowires forests grown circumferentially on a suspended glassy carbon nanowire were characterized by measuring the electrical resistance change according to various  $\text{NO}_2$  concentrations (50 ppb - 500 ppb). As shown in Figure 3.15, the electrical resistance of ZnO nanowires forests increases with the concentration of  $\text{NO}_2$  gas; this reflects the general nature of n-type semiconductor-based gas sensors such as ZnO nanowires for oxidizing gases such as  $\text{NO}_2$

since the  $\text{NO}_2$  is oxidizing gas and ZnO is n-type semiconductor. The sensor showed a high gas response (=change in resistance after gas injection / resistance before gas injection) even at very low concentration ( $\sim 11.4$  for 50 ppb  $\text{NO}_2$ ). This high gas sensing capability will probably be due to the long crystalline and high crystallinity of the ZnO nanowires grown on the suspended carbon nanowire [44]. The gas response increases linearly to 500 ppb with a sensitivity of  $30.21 \text{ ppb}^{-1}$  and the gas response resumes linear increase with concentration at a sensitivity ( $2.88 \text{ ppb}^{-1}$ ) lower than the first linear gas concentration range (50 – 500 ppb). This is because as the concentration of  $\text{NO}_2$  increases, the available sites of the ZnO nanowires surfaces become saturated and the electrical resistance of the ZnO nanowires forests approaches the electrical resistance of the suspended glassy carbon nanowire ( $\sim 190 \text{ M}\Omega$  at  $200^\circ\text{C}$ ).

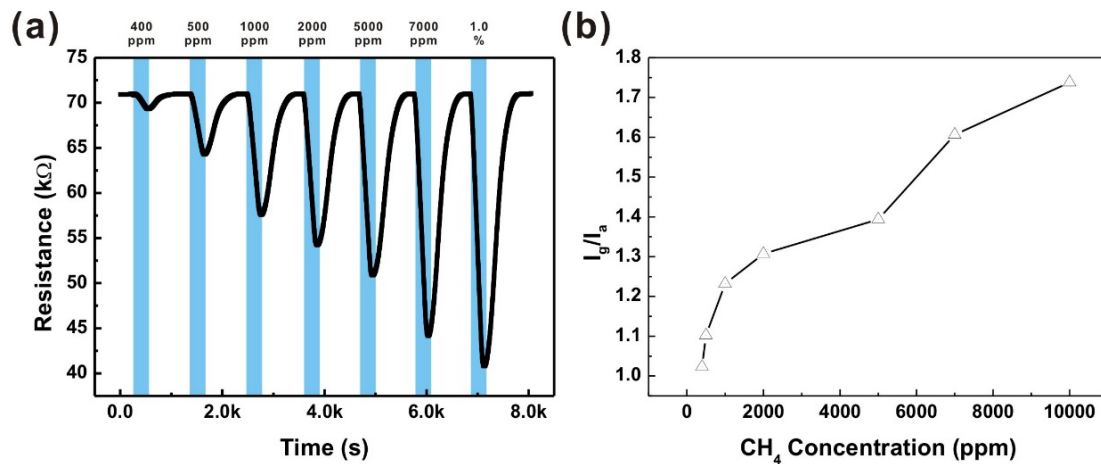


**Figure 3.18** Gas sensing characteristics of a ZnO nanowires forests/carbon nanostructure based gas sensor for various  $\text{CH}_4$  gas concentration mixed in dried air at  $200^\circ\text{C}$ .

The impact of the interrupted gas sensor architecture on response and recovery times is also analyzed in Figure 3.16. The gas sensor response time is defined as the time required for the sensor to reach 90 % of the maximum electrical resistance change after the gas exposure. The recovery time is defined as the time to recover 90% of the initial signal

after closing the target gas valve. As shown in Figure 3.16, the response time and the recovery time decrease with the gas concentration in all gas sensor configuration, including suspended structure and substrate-bound structure typed sensors. The suspended structure type sensor showed faster the response and the recovery time than the substrate-bound type sensor. This may also be due to the improved structure and the enhanced mass transfer due to the circumferentially distributed ZnO nanowires.

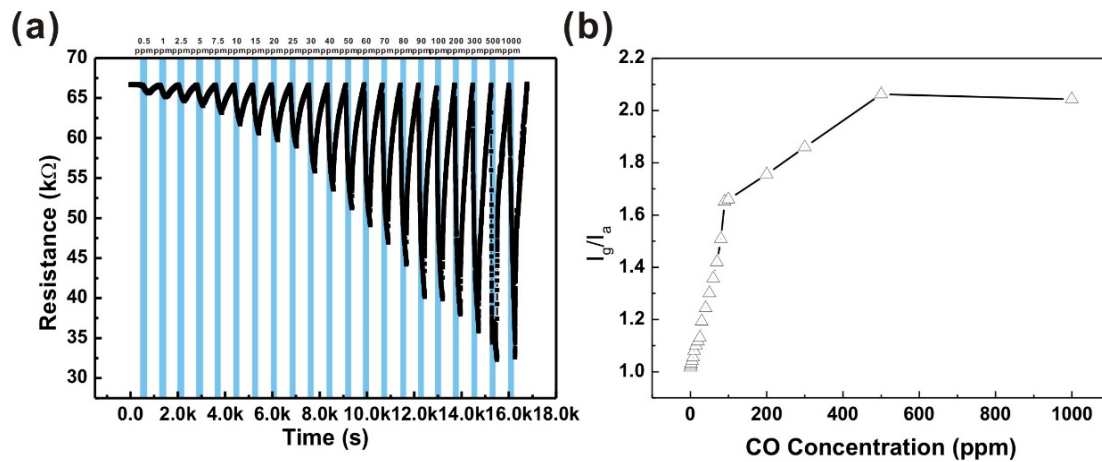


**Figure 3.19** Gas sensing characteristics of a ZnO nanowires forests/carbon nanostructure based gas sensor for various CO gas concentration mixed in dried air at 200 °C.

The long-term stability of the suspended gas sensing platform was investigated by measuring gas response at 500 ppb NO<sub>2</sub> for 2-months, as shown in Figure 3.17. The base resistance of the suspended structure type sensor (the resistance before the gas injection) and the resistance changes at 500 ppb NO<sub>2</sub> of a suspended sensor did not change significantly during the 20month testing period. In long-term stability tests, the gas sensor was stored in the air without humidity control. This confirms that the influence of humidity on the gas sensing material is not significant. The suspended nanowire-type gas sensor showed excellent stability. During the stability test, the gas sensor was stored in the air without humidity control. This confirms the practical applicability of the proposed sensor. Figure 3.18 shows

the gas sensing response measurements from 400 ppm to 1 % at various concentrations  $\text{CH}_4$  gas. Unlike the reducing gas of  $\text{NO}_2$  gas, the electrical conductivity is improved by the oxidizing gas such as  $\text{CH}_4$ ,  $\text{CO}$ ,  $\text{C}_6\text{H}_6$ ,  $\text{H}_2$ ,  $\text{SO}_2$ . The increasing rate in the electrical conductivity is linearly reduced by the gas concentrations of  $\text{CH}_4$  mixed in dry air at  $200^\circ\text{C}$ . The linear curve of the existing hierarchical ZnO nanowires forests/glassy carbon nanowire is 400 ppm to 1% and the LOD is about 381 ppm of the  $\text{CH}_4$  gas concentration.

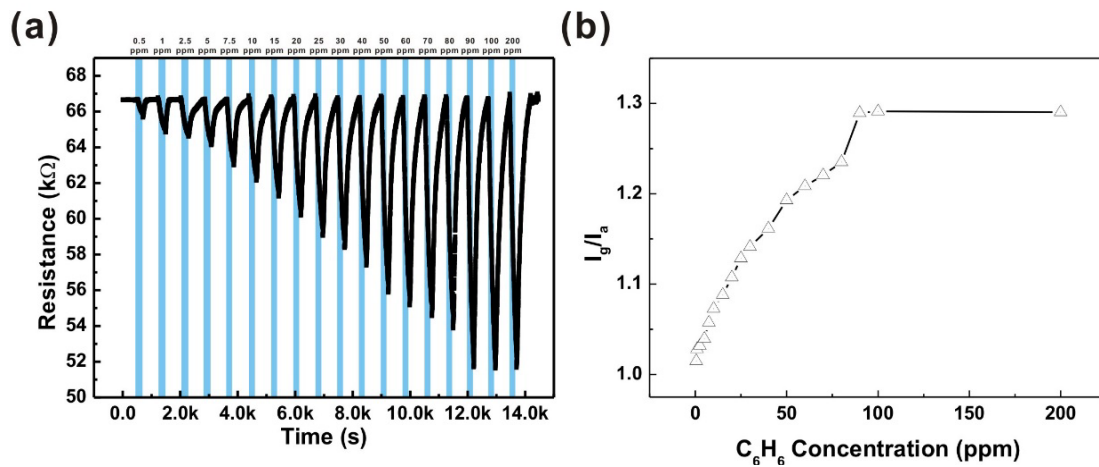


**Figure 3.20** Gas sensing characteristics of a ZnO nanowires forests/carbon nanostructure based gas sensor for various  $\text{C}_6\text{H}_6$  gas concentration mixed in dried air at  $200^\circ\text{C}$ .

Figure 3.19 illustrates gas sensing response measurements at various gas concentrations of the CO from 500 ppb to 1,000 ppm. As shown in Figure 3.19 (b), there are two types of linear curves for the gas sensing response depending on the gas concentration. One linear curve is at a low concentration of CO gas from 500 ppb to 90 ppm and the other linear curve is at a high concentration from 100 ppm to 500 ppm. However, at higher concentrations of 500 ppm CO gas, the maximum CO gas sensing value of the suspended hierarchical ZnO nanowires forests/glassy carbon nanowire is 500 ppm because of the similar CO gas response between 500 ppm and 1,000 ppm. The increasing rate in the electrical conductivity decreases linearly with the gas concentration of  $\text{O}_2$  mixed with dry air at  $200^\circ\text{C}$ .

The linear curve of the suspended hierarchical ZnO nanowires forests/glassy carbon nanowire is 500ppb to 90 ppm and the LOD is about 1.05 ppm of the CO gas concentration.

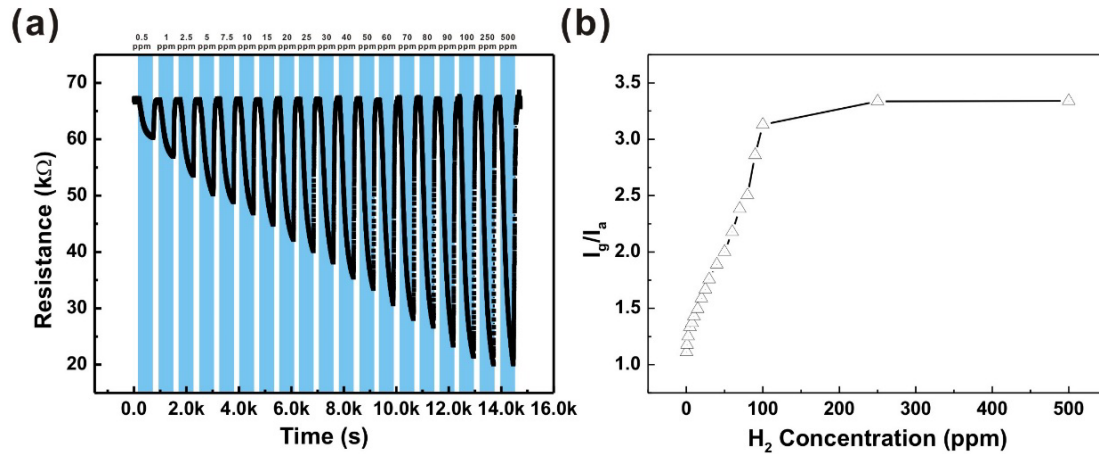


**Figure 3.21** Gas sensing characteristics of a ZnO nanowires forests/carbon nanostructure based gas sensor for various  $H_2$  gas concentration mixed in dried air at  $200\text{ }^\circ\text{C}$ .

Figure 3.20 shows gas sensing response measurements at various gas concentrations of  $C_6H_6$  from 500 ppb to 200 ppm. The  $C_6H_6$  gas sensing response increases linearly from 500 ppb to 90 ppm. Above a 100 ppm  $C_6H_6$  gas concentration, the gas sensing response is similar. The increasing rate in the electrical conductivity is linearly reduced by the gas concentration of  $C_6H_6$  mixed in dry air at  $200\text{ }^\circ\text{C}$ . The linear curve of the suspended hierarchical ZnO nanowires forests/glassy carbon nanowires is 500 ppb to 90 ppm and the LOD is about 1.28 ppm of the  $C_6H_6$  gas concentration.

Figure 3.21 illustrates gas sensing response measurements at various  $H_2$  gas concentrations from 500 ppb to 500 ppm.  $H_2$  gas sensing response based on the suspended hierarchical ZnO nanowires forests/glassy carbon nanowire increases linearly from 500 ppb to 100 ppm. When the  $H_2$  gas concentration is higher than 100 ppm, the  $H_2$  gas sensing reaction is not detected. The gas sensing response is increased linearly with the  $H_2$  gas concentration with dry air at  $200\text{ }^\circ\text{C}$ . The linear curve of the suspended hierarchical ZnO

nanowires forests/glassy carbon nanowire is 500 ppb to 100 ppm, and the LOD is about 0.39 of the H<sub>2</sub> gas concentration.

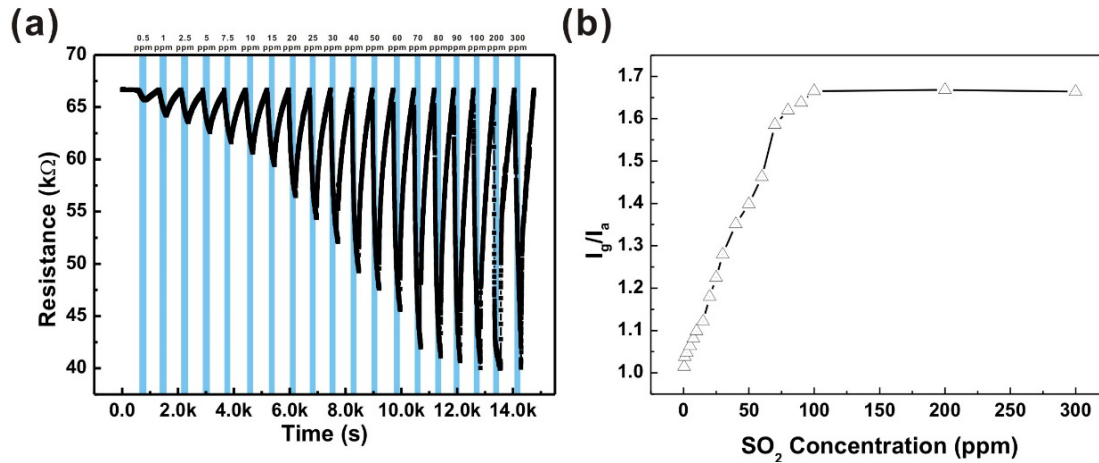


**Figure 3.22** Gas sensing characteristics of a ZnO nanowires forests/carbon nanostructure based gas sensor for various SO<sub>2</sub> gas concentration mixed in dried air at 200 °C.

Figure 3.22 shows the gas sensing response measurements at various gas concentration of SO<sub>2</sub> from 500 ppb to 300 ppm. The SO<sub>2</sub> gas sensing response increases linearly from 500 ppb to 100 ppm. When the SO<sub>2</sub> gas concentration is higher than 100 ppm, the SO<sub>2</sub> gas sensing response is similar. The SO<sub>2</sub> gas sensing response is increased linearly at SO<sub>2</sub> gas concentrations from 500 ppb to 100 ppm with dry air at 200 °C. The LOD is about 0.89 ppm of the SO<sub>2</sub> gas concentration.

The gas selectivity based on the suspended hierarchical ZnO nanowires forests/glassy carbon nanowire is shown as Figure 3.23. Gas sensing response is similar at 2.5 ppm C<sub>6</sub>H<sub>6</sub>, CO, H<sub>2</sub>, SO<sub>2</sub> and is about 1.1. However, NO<sub>2</sub> gas sensing response is most achieved. The CH<sub>4</sub> gas response is the lowest, but the gas sensing platform has a gas selectivity of CH<sub>4</sub>.



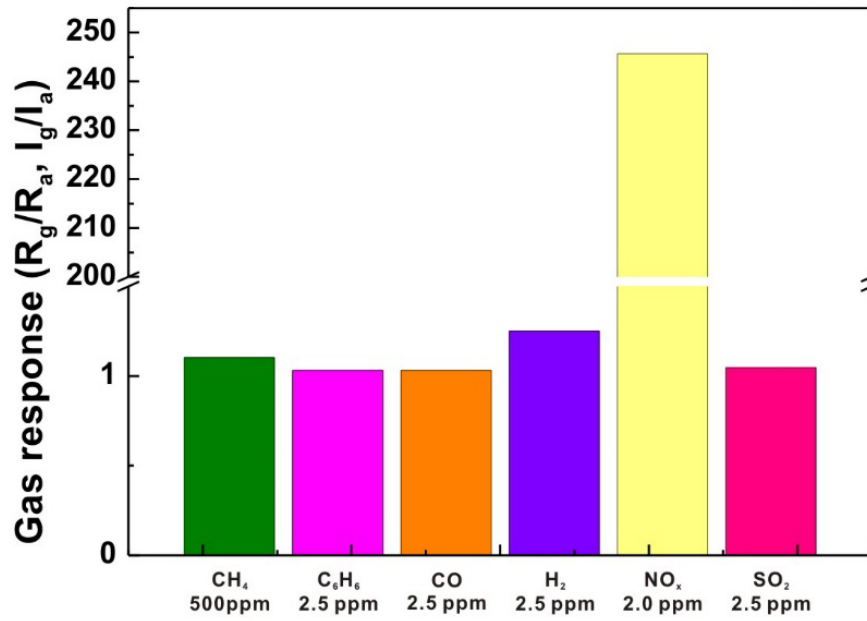


**Figure 3.23** Gas selectivity based on a suspended hierarchical ZnO nanowires forests/glassy carbon nanowire in dried air at 200 °C.

# 4

## **Suspended 1D metal oxide nanostructure integrated the nano- heater**

*In this chapter, a suspended 1D metal oxide nanostructure grown on the HfO<sub>2</sub>/glassy carbon nanowire will be introduced to apply the gas sensing platform integrated the internal heater. Also, fabrication steps and material property will be given.*

## 4 Suspended 1D metal oxide nanostructure integrated the nano-heater

### 4.1 Background

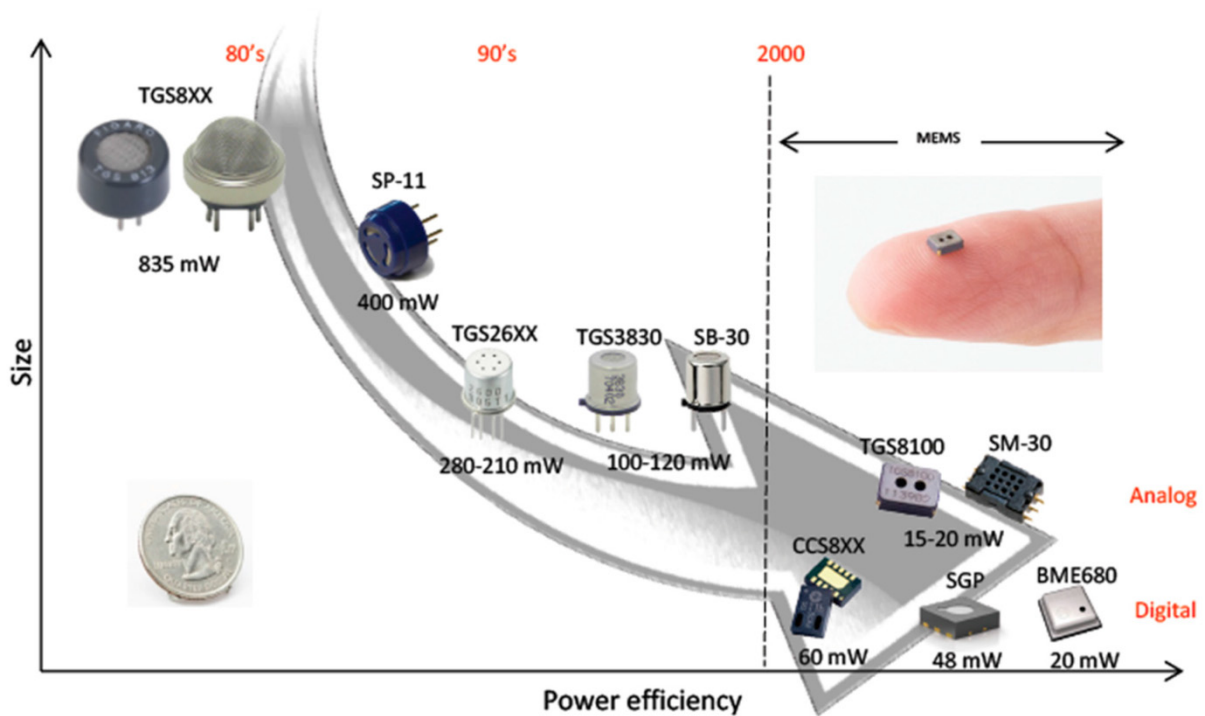


**Figure 4.1** Development of metal oxide semiconductor gas sensors in size and power efficiency from J. Burgues et. al. [135].

Metal oxide nanowires have excellent gas sensing materials. However, high operating temperatures are required for gas sensing platforms. The main source of power consumption of the metal oxide semiconductor gas sensor is a resistor that heats the sensing surface to promote an efficient redox reaction between the adsorbed gas molecules and the metal oxide [133, 134]. For portable gas sensing platforms, the research groups developed a gas sensing platform based on the metal oxide nanowires incorporating a heating system using the MEMS manufacturing [135-145]. Using the MEMS fabrication, a portable

gas sensing platforms was developed in the micro-structure. Even if the society is satisfied with the size of the gas sensing platform, it is difficult to apply the gas sensing platform in the industry due to the high power consumption of the heating system. As well as, due to limited power consumption and the intended intermittent device operation, continuous power supply is not possible in many battery-operated applications. When gas sensing technology is implemented in smartphones, users could evaluate air quality anywhere. Geo-tagging and Internet of Thing (IoT) could be done simultaneously to build a fine-grain air pollutions map of all measurement data using built-in localization and connectivity features or smartphones and wearables. The power consumption of the metal oxide semiconductor gas sensor represents 3.14 % of the total smartphone power usage or, 45 minutes of battery life reduction. For example, the recently introduced SGP sensor (sensirion AG) integrates several metal oxide semiconductor gas sensors on the same chip to increase power consumption to 48 mW. This represents 10 % of the smartphone's power consumption or 2 hours and 15 minutes of battery life. Obviously, power consumption needs to be further reduced. In additional, suspended structure has been developed because it is difficult to transfer the heating space to another space to reduce the power conduction of the heating system [139].

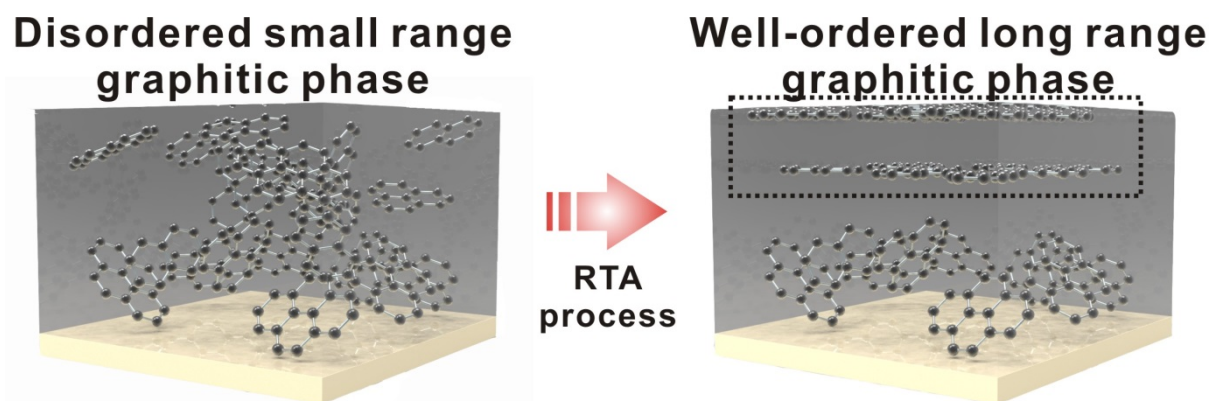


**Figure 4.2** Schematic showing the increase in the degree of alignment of the graphitic phase owing to the RTA process.

**Table 3.** Power consumption using the metal oxide semiconductor gas sensor integrated the MEMS heating system.

No.	Sensing materials	Heating materials	Power consumption	Reference
1	SnO <sub>2</sub>	Pt/Ti	66 mW (325 °C)	[146]
2	SnO <sub>2</sub> -Pd	Pt/Ti	18 mW (300 °C)	[147]
3	SnO <sub>2</sub>	Pt/Ti	34.2 mW (400 °C)	[148]
4	SnO <sub>2</sub>	Pt/Ti	15 mW (400 °C)	[149]
5	SnO <sub>2</sub>	Pt/Ti	7.7 mW (20 °C)	[150]
6	SnO <sub>2</sub> -Pd, WO <sub>3</sub>	Pt/Ti	15.5 mW (150 °C)	[151]
7	SnO <sub>2</sub>	Pt/Ti	30 mW (350 °C)	[107]
8	ZnO, V <sub>2</sub> O <sub>5</sub> , SnO <sub>2</sub> , WO <sub>3</sub>	Pt/Ti	2 mW (300 °C)	[152]

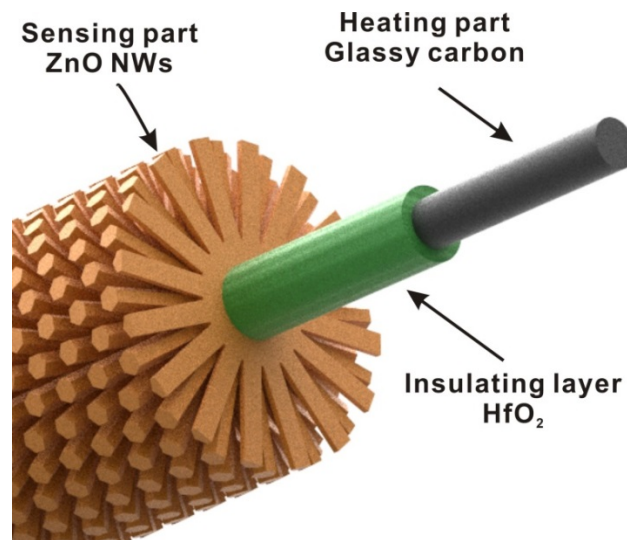


**Figure 4.3** Schematic image of detailed our gas sensing platforms based on the suspended hierarchical metal oxide nanostructures grown on the HfO<sub>2</sub>/glassy carbon nanowire integrated the heating system.

We designed a gas sensing platform based on the metal oxide nanowire incorporating a suspended glassy carbon heating nanostructure. However, it is difficult to

apply the heating nanostructure to the electrical conductivity of the glassy carbon structure. The researchers have developed a pre-treatment process to improve electrical conductivity, such as various doping and annealing processes, to overcome the relatively low electrical conductivity of the glassy carbon structure. Negative photoresist of SU-8 with the CNT was patterned into nanowires using electro-spinning and this wires were pyrolyzed [153]. This CNT doping improved the graphite phase and the electrical conductivity reached  $\sim 3.1 \times 10^6$  S/m, much higher than the graphite. However, this doping process requires conformal mixing of CNTs and the photoresist, which must be maintained during the post-polymer-patterning process. Unlike the doping process, the annealing process is widely used for various materials including metal oxide semiconductors [154, 155]. It has been reported that the electrical conductivity of pyrolytic carbon processed using the CVD is improved at three times, and the crystallization and the thermal stability are enhanced [155]. In addition to electrical conductivity, other material properties such as crystallization and thermal stability could be enhanced through the annealing process and the doping process [154].

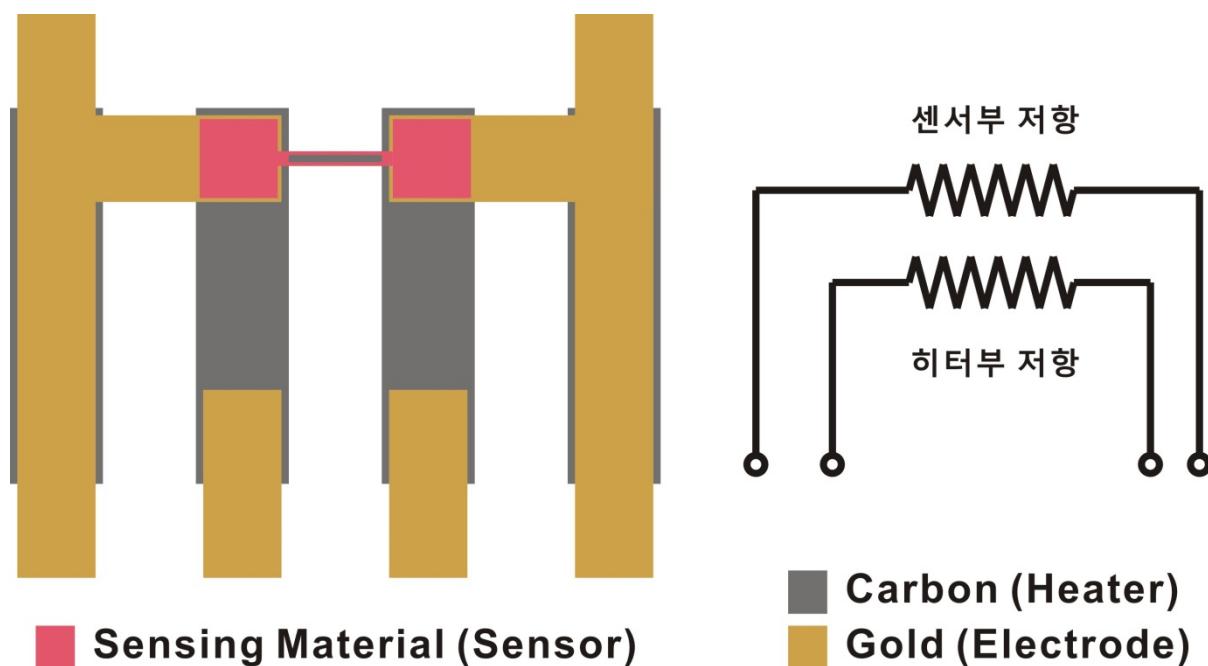


**Figure 4.4** Schematic image of our gas sensing platforms and an electrical circuit.

A metal oxide gas sensing platform with the heating system is also the connection between the sensing part of the metal oxide nanowires and the heating part, as shown in Figure 4.4. The connecting material is in electrical insulation and low thermal insulating property. Primarily, high electrical insulating materials have high thermal insulating property owing to similar conducting mechanisms in the ceramic materials. Thin insulating materials with high dielectric constant are the best way to apply the connection between the metal oxide nanowire and the suspended carbon nano-heater, but the insulation properties are affected by the density. There are various insulating deposition processes such as plasma enhanced chemical vapor deposition (PECVD), atomic layer deposition (ALD) and rf-sputtering process [156-159]. During these insulating deposition processes, the rf-sputtering process yields the lowest density insulating material. The processing time of PECVD is faster than that of ALD process, but insulating materials made of ALD have the highest density. In addition, various high permittivity materials such as  $\text{HfO}_2$  and  $\text{Al}_2\text{O}_3$  produced by the ALD have been developed [157-159].

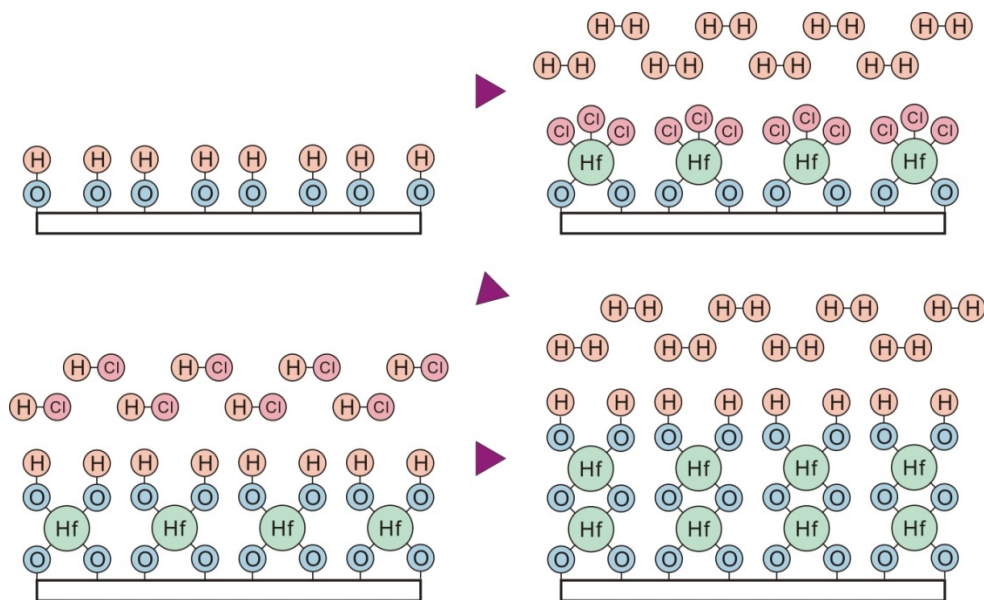


**Figure 4.5** Schematics of mechanisms of the  $\text{HfO}_2$  deposition fabricated by the atomic layer deposition process.

The ALD process is a vapor phase deposition process capable of producing thin films having various materials at the high density. The ALD process consists of a gas surface reaction and a purge process. Gas surface reactions are called “half-reactions” and are synthesized in the surface area. During the half-reaction, the precursor is charged into the chamber under a vacuum of less than 1 torr, and the precursor is converted to the by-products through a self-limiting process that does not leave a thin layer on the surface confinement zone [159]. A non-reactive gas such as N<sub>2</sub> or Ar is then purged in the chamber to remove any unreacted precursor that has no surface area. This process is a cyclic process that mixes the half reaction and the purge process. The thickness of the insulation thickness is affected by the number of cycles and the synthesis temperature.

Hierarchical metal oxide nanowires such as ZnO, In<sub>2</sub>O<sub>3</sub>, CuO and SnO<sub>2</sub> have been developed to provide candidate materials for gas sensing materials due to their high surface to volume ratio, reasonable detection limits, and a wide range of detectable gases such as NO<sub>2</sub>, CO, CO<sub>2</sub>, H<sub>2</sub>, NH<sub>3</sub> [99, 114, 160-163]. Among the hierarchical metal oxide nanowires, ZnO nanowires showed better detection performance than one-dimensional nanowires [114, 162]. However, the effects of the hierarchical metal oxide nanowires could be maximized when the hierarchical nanowires are located away from the substrate-bound, structure and the batch fabrication techniques for the complex structures of a suspended structure have not yet been well developed.

In this study, we developed a metal oxide gas sensing platform incorporating a heating system. Our gas sensing platforms consists of the sensing part, the insulating layer and the heating part. Various metal oxide nano-structures such as ZnO, CuO were synthesized using the hydrothermal method consisting of the seed deposition process and the growth process. To selectively deposit a metal oxide seed layer on a suspended nanowire, a positive



photoresist was coated and the place of a suspended nanowire was only opened [150]. The growth was carried out using an autoclave system. In addition, the hydrothermal method compatible with the CMOS process is used to grow the hierarchical metal oxide nanowire relatively at a low temperature. As an insulating layer, the  $\text{HfO}_2$  layer was deposited using an ALD process. The suspended glassy carbon nanowires were synthesized using carbon-MEMS. This section demonstrates the perfect integration of the suspended hierarchical metal oxide nanowires grown circumferentially on  $\text{HfO}_2$ /glassy carbon nanowire, adding a heating system that uses only batch fabrication process to ensure high gas sensing capability and excellent manufacturability.

## 4.2 Fabrication & Experimental

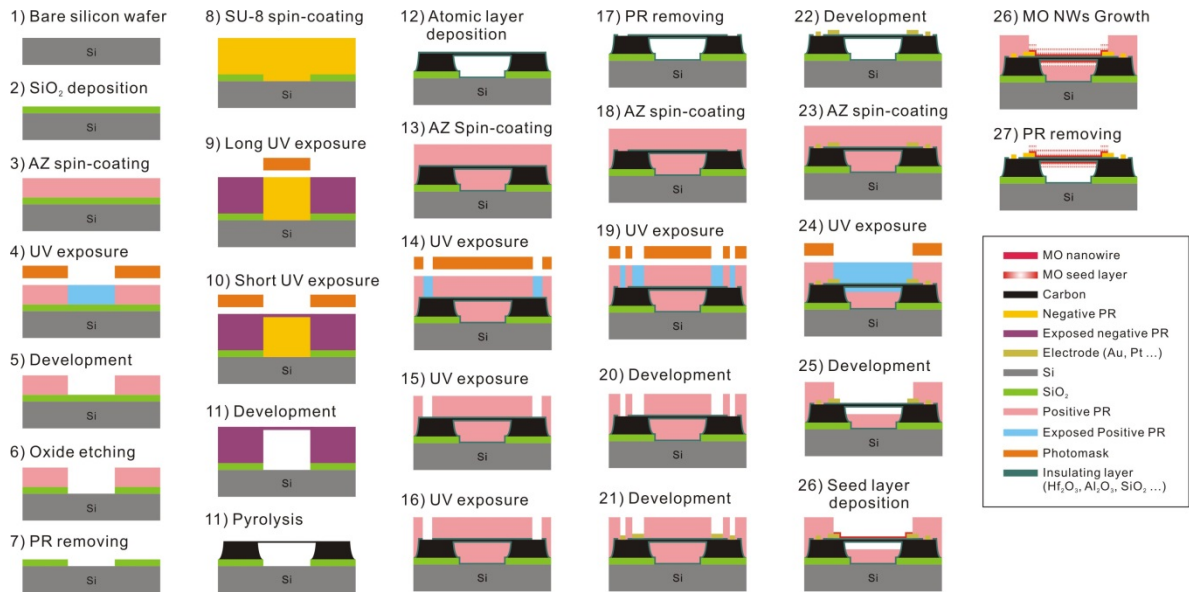


**Figure 4.6** Fabrication steps for a suspended hierarchical ZnO nanowires forests/HfO<sub>2</sub>/glassy carbon nanowire for use as gas sensor integrated a heating system.

The fabrication steps for the suspended hierarchical metal oxide nanostructures grown on the HfO<sub>2</sub>/glassy carbon nanowire integrated an internal heating system are illustrated in Figure 4.5. Before the fabricating an internal heating system using a glassy carbon structure, 1- $\mu$ m-thick SiO<sub>2</sub> layer was deposited on a 6-inch Si wafer (p-type, boron, 5-20  $\Omega$ -cm, 660 – 700  $\mu$ m thick; LG Siltron Co., Ltd., Republic of Korea) using the wet oxidation process based on a thermal oxidation. The SiO<sub>2</sub>/Si substrate was cleaned using a hot piranha solution (H<sub>2</sub>SO<sub>4</sub> : H<sub>2</sub>O<sub>2</sub> = 4 : 1) and a dehydration process was performed on a hot plate at 200 °C for 5 min. A positive photoresist of 1.2- $\mu$ m-thick (AZ-5214E, AZ Electronic Materials, USA) was coated using the spin-coating machine and based at 105 °C for 2 min. After the patterning process using the UV-expose process (100 mJ cm<sup>-2</sup>), the SiO<sub>2</sub> patterns were made using the BOE solution (J. T. Baker, Chemical Co., Ltd., USA). A negative photoresist of 48.5- $\mu$ m-thick (SU-8 2050, MicroChem. Corp., USA) was coated

using the spin-coating machine on the SiO<sub>2</sub>/Si substrate and soft-baked at 95 °C for 11 min, a negative photoresist structure was made using a UV expose (230 mJ cm<sup>-2</sup>) that support a suspended negative photoresist microwire. A second UV exposure (16 mJ cm<sup>-2</sup>) was performed to selectively polymerize between the pre-exposed post structures to make a suspended photoresist microwire. A suspended negative photoresist microwire was formed by the development process. A suspended negative photoresist microwire structure was converted into a suspended glassy carbon nanowire structure using the polymer pyrolysis process because of the high volume decreasing ratio. A suspended glassy carbon nanowire was progressed by the annealing process with 1000 °C and 5.0 x 10<sup>-6</sup> torr for 4 min at the RTA, as described at Figure 4.6. In the RTA system, the fabricating temperature was measured using a k-type thermocouple that directly connected to the sample stage during the RTA process (accuracy ± 5 %).

Hierarchical metal oxide nanostructures forests were made by the autoclave process. Before the metal oxide seed layer deposition process, a positive photoresist of 14-μm-thick (AZ 4330, AZ Electronic Materials, USA) was coated on these substrate to the selective open. To selective deposit the metal oxide seed layer on a suspended glassy carbon nanowire, a positive photoresist layer was exposed to a low dose (50 mJ cm<sup>-2</sup>) better than the database sheet to be etched selectively by the developing solution. After the development process, a positive photoresist was covered without a suspended glassy carbon nanowire. To make the multiplex gas sensor based on the CuO & ZnO nanostructures, a 20-nm-thick ZnO and CuO seed layer was deposited on a selective suspended glassy carbon nanowire and a positive photoresist structure using the rf-sputtering process (SRN-120, Sorona Co., Ltd., Republic of Korea) and a positive photoresist was removed using the acetone (J.T. Baker Chemical Co., Ltd., USA). First growth process was progressed to make the CuO nanoflakes on the suspended HfO<sub>2</sub>/glassy carbon nanowire in 10 mM Copper (II) nitrate trihydrate

( $\text{Cu}(\text{NO}_3)_2 \cdot 6\text{H}_2\text{O}$ ) with 10 mM hexamethylene tetramine ( $(\text{CH}_2)_6\text{N}_4$ , HMTA) using the autoclave system owing to the high pressure and higher temperature better than water evaporation degree of 100 °C. And then, second growth process was progressed to make the ZnO nanowires on the suspended  $\text{HfO}_2$ /glassy carbon nanowire in 10 mM zinc nitrate hexahydrate ( $\text{Zn}(\text{NO}_3)_2 \cdot 6\text{H}_2\text{O}$ ) with 10 mM HMTA ( $(\text{CH}_2)_6\text{N}_4$ ) using the autoclave system [163].

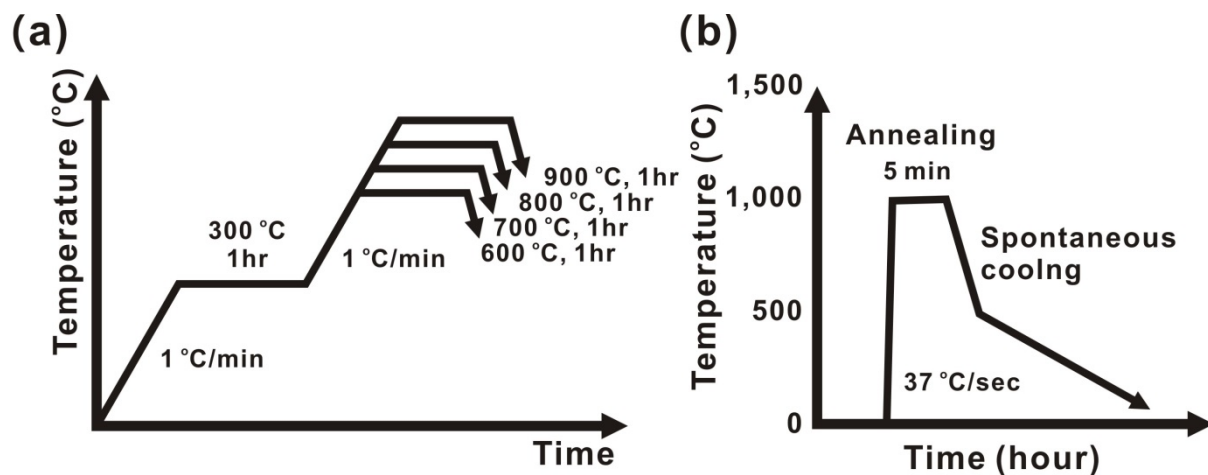


**Figure 4.7** (a) Pyrolysis condition for the glassy carbon structure fabrication and (b) RTA process condition for the enhancement of the electrical conductivity.

Microstructures of a suspended hierarchical metal oxide nanostructure grown on the  $\text{HfO}_2$ /glassy carbon nanowire were characterized using the SEM and HRTEM. TEM samples of a circumferentially grown hierarchical metal oxide nanostructure forests on a substrate-bound  $\text{HfO}_2$ /glassy carbon nanowire were prepared using a FIB milling machine. Characteristics of the insulating property of the breaking down voltage of the  $\text{HfO}_2$  layer deposited on a glassy carbon nanowire using the ALD process were measured by a source meter (Keithely 6517B, Keithley Instruments, Inc., USA). The heating property of the heating structure of a suspended glassy carbon is predicted based on the electrical characteristics depending on the temperature of the external heater of the hot plate.

Various gas detection responses such as NO<sub>2</sub>, CO, H<sub>2</sub>, SO<sub>2</sub>, C<sub>6</sub>H<sub>6</sub> and CH<sub>4</sub> were measured at atmospheric pressure in a chamber was purged by the N<sub>2</sub> gas purging. Gas concentrations were controlled by mixing 0.1 % concentration and N<sub>2</sub> using a gas flow meter (GMC 1200, ATOVAC, Republic of Korea). The gas sensing property was measured without an external heater using a source meter (Keithely 2401, Keithley Instruments, Inc., USA) in various gas concentrations with N<sub>2</sub> gas.

### 4.3 Results & discussion

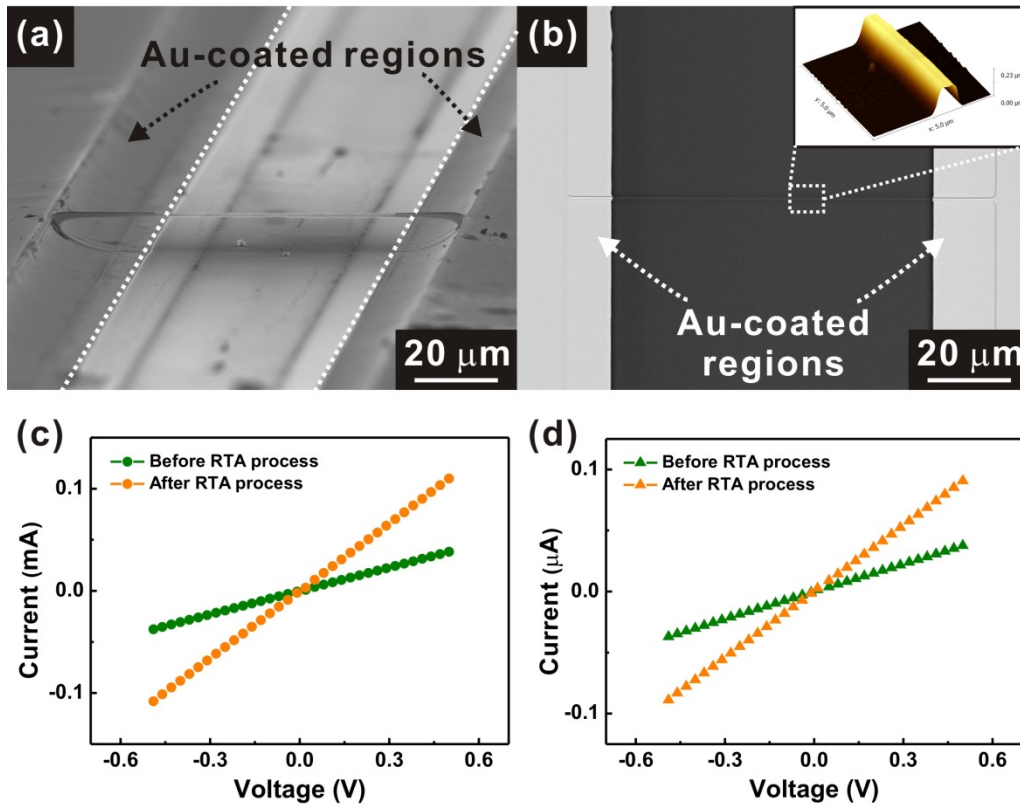


**Figure 4.8** SEM images of (a) a suspended and (b) a substrate-bound carbon nanowire. I-V characteristics of (c) a suspended and (d) a substrate bound nanowire.

Various carbon nano-structures such as the suspended glassy carbon nanowire and the substrate-bound glassy carbon nanowire can be easily fabricated using carbon-MEMS. Suspended glassy carbon nanowires experienced shrinkage due to tensile stresses due to volume reduction during the polymer pyrolysis process. The volume reduction ratios is  $\sim 97\%$  in a suspended carbon nanowires, while the volume decreasing ratio is  $\sim 88\%$  without decreasing the length and width at the substrate-bound nanowire due to the van-deer-wall force between the photoresist pattern and the substrate at the photolithography and the block must remove some of the molecules generated by the polymer pyrolysis process. Therefore, substrate-bound carbon nano-structure was prepared as a trapezoidal structure after the

polymer pyrolysis process.

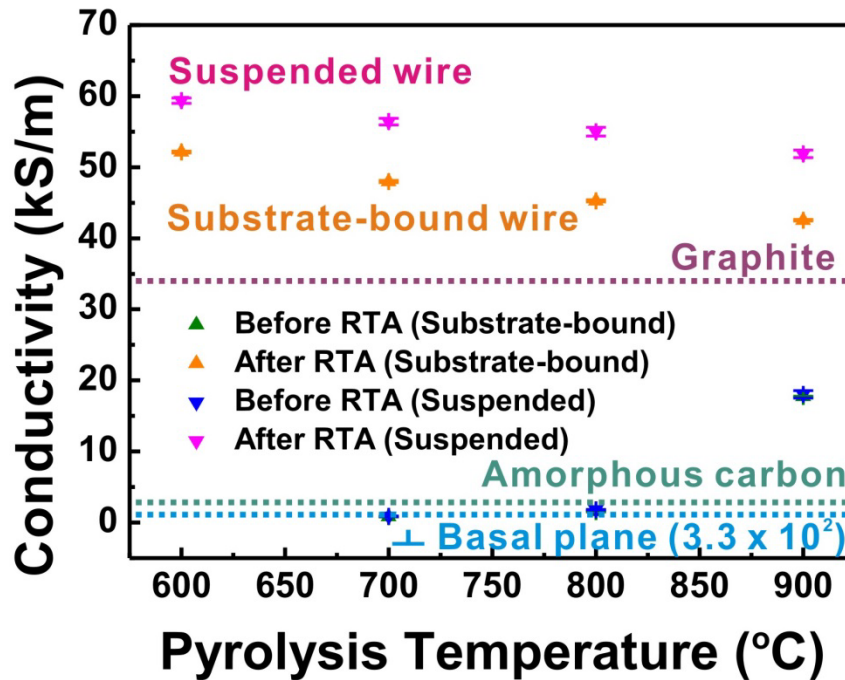


**Figure 4.9** Electrical conductivities of a suspended and a substrate-bound glassy carbon nanowire at pyrolysis condition before and after the RTA process.

The 4-probe measurement method is useful tool for measuring the electrical conductivity because the effect of the voltage drop effect on the resistance of the nanowire is reduced by the compensated voltage. The wire-like structure consisting of wire and pad is the structure optimized for measuring electrical conductivity without the 4-probe measurement method [164]. However, the difference between center and edge in the suspended glassy carbon nanowires was caused by the volume reduction of the posts supporting the suspended glassy carbon nanowires during the polymer pyrolysis. To improve the accuracy of electrical conductivity in the suspended glassy carbon nanowires, the gold layer was deposited only at the edges of the suspended glassy carbon nanowires by electron beam evaporation without changing the length of the glassy carbon nanowires. In addition, the electrical conductivity changed greatly according to the thermal decomposition conditions of the polymer such as

the treatment temperature, and the voltage drop effect was reduced in the post.

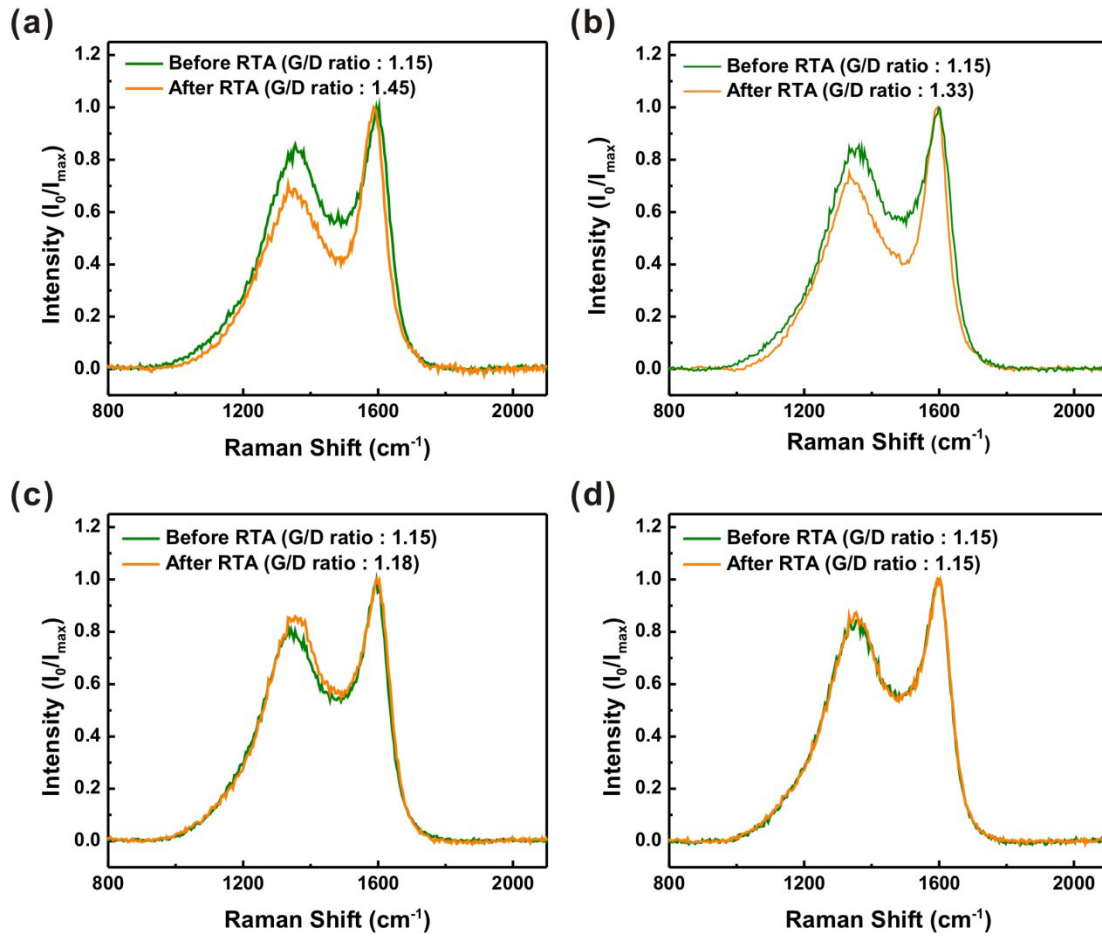


**Figure 4.10** Raman spectrum of a glassy carbon structure before (green line) and after RTA process (orange line) consisting of (a) 600 °C, (b) 700 °C, (c) 800 °C, and (d) 900 °C .

The electrical properties of various glassy carbon nanostructures have ohmic contacts in Figure 4.8 (c-d). In order to improve the electrical conductivity of various glassy carbon nanostructures, an annealing process was carried out, and the electrical conductivity was changed without changing the shape by the annealing process. Strengthening rates of various glassy carbon nanostructures have been changed according to the polymer pyrolysis conditions at the process temperature. The difference in electrical conductivity of the various glassy carbon nanostructures was not found before the annealing process, but the difference between the glassy carbon nanowires hanging after the annealing process and the substrate-



bonded glassy carbon nanowires was calculated to be 14%.

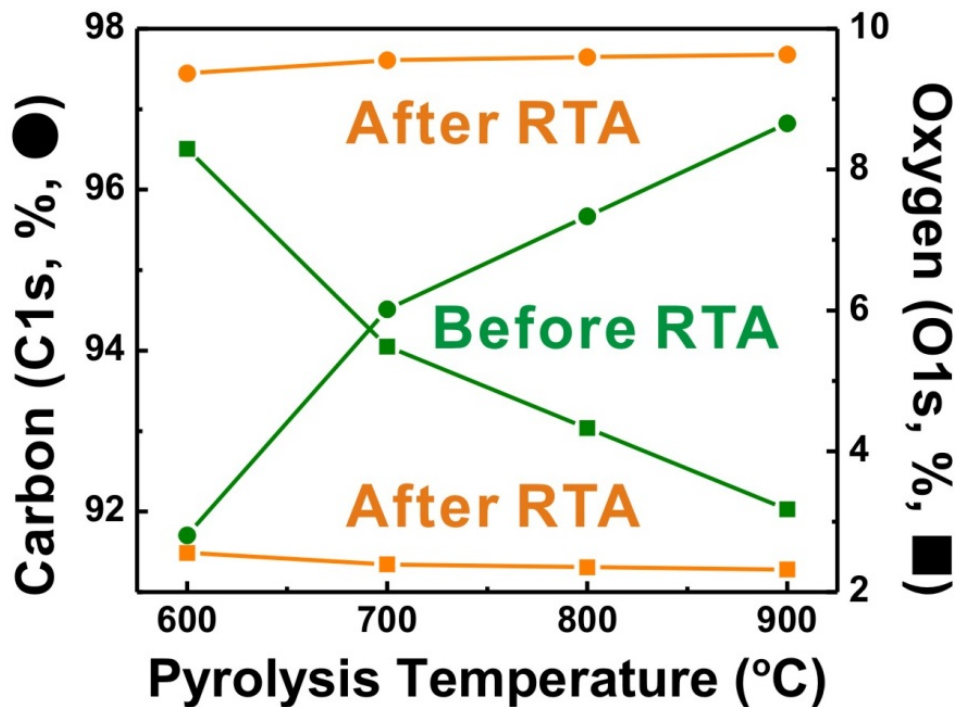


**Figure 4.11** XPS analysis a glassy carbon structure before (green line) and after RTA process (orange line) consisting of (a) 600 °C, (b) 700 °C, (c) 800 °C, and (d) 900 °C .

Carbon nanostructures were characterized by Raman spectroscopy in order to explain the microstructure and graphitization in carbon nanostructures. The D-band and the G-band peak of the glassy carbon material are the same when the temperature is changed in the polymer pyrolysis process [37-39, 42]. Some researchers have shown that carbon materials with a D/G ratio of  $\sim 0.87$  can be successfully used as electrode materials [42]. The ratio of D/G after annealing depends on the temperature of the polymer pyrolysis process. In addition, the full width half maximum (FWHM) of the G-band peak is increased by the pyrolysis temperature after the RTA process. Crystallite size in the glassy carbon structure is estimated by the intensity ratio between G-band and D-band depending on Tuinstra & Koenig relation and is increased by the pyrolysis temperature. The electrical conductivity of the carbon structure was enhanced by the increased graphite phase and crystallite size.

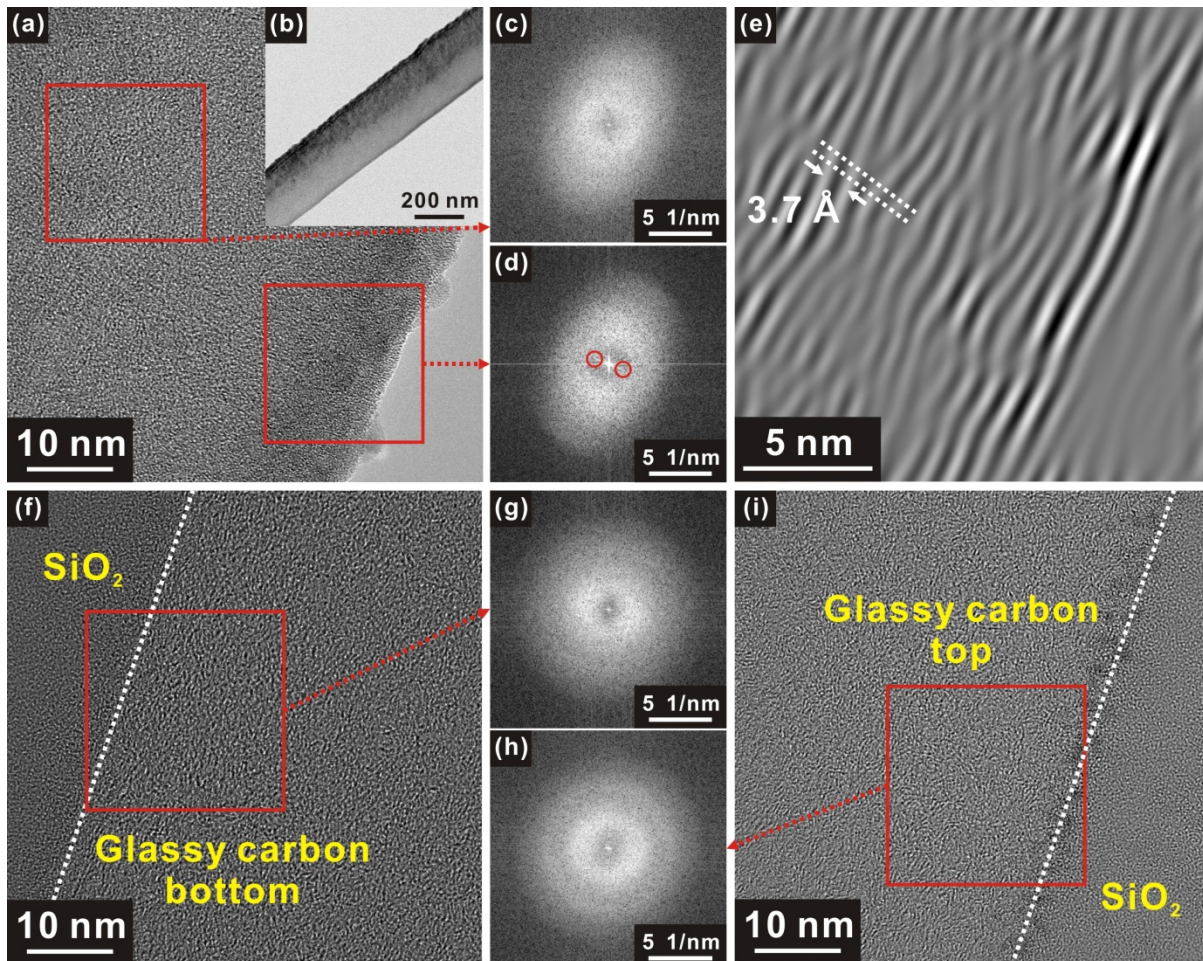


**Figure 4.12** (a, b) TEM image, (c, d) diffraction pattern, and (e) inverse FFT of a suspended glassy carbon nanowire after the RTA process. (f, i) TEM image, (g, h) diffraction pattern of a substrate-bound glassy carbon nanowire.

The oxygen/carbon composition ratio is important for carbon materials produced using the polymer pyrolysis process. Chemical composition was characterized by XPS analysis as shown in Figure 4.11. The oxygen/carbon composition ratio in the glassy carbon structure prepared by carbon-MEMS is about 0.03 [44]. Before the RTA process, the composition of carbon increased and the composition of oxygen decreased with the thermal decomposition temperature of polymer. After the RTA process, the carbon and oxygen compositions are similar without changing the polymer pyrolysis temperature. The electrical conductivity of the glassy carbon structure improves as the oxygen composition decreases

after the RTA process. The increasing graphite phase is indicated by the rate of reduction of the oxygen/carbon composition ratio. The oxygen atoms interconnected by carbon atoms were arranged by a graphene healing mechanism [165-167]. Oxygen atoms that are interconnected by carbon atoms are easier to align than carbon atoms, not interconnected oxygen atoms because of the low binding energy.

**Table 4.** Categorization of the breaking down voltage of the insulating materials such as  $\text{Al}_2\text{O}_3$ ,  $\text{HfO}_2$ ,  $\text{SiO}_2$ .

Insulating Material	$\text{Al}_2\text{O}_3$	$\text{HfO}_2$	$\text{SiO}_2$
Breaking down Voltage	5.97 V (20 nm)	11.82 V (20 nm)	13.2 V (200 nm)
Insulating property	29.9 mV/nm	59.1 mV/nm	6.6 mV/nm

The electrical conductivity of the glassy carbon structure was altered by the polymer pyrolysis temperature and the RTA characterized by Raman spectroscopy and XPS analysis. However, using Raman spectroscopy and XPS analysis, it is difficult to find the cause of the other electrical conductivity between suspended and substrate-bound glassy carbon nanowires. We have found that the electrical conductivity of suspended glassy carbon nanowires is higher than that of substrate-bonded glassy carbon nanowires. And the crystallinity of carbon atoms in these carbon nanostructures was analyzed by TEM analysis. Aligned carbon atoms are predominantly present in the surface area than in the center in suspended carbon nanowires characterized by the inverse diffraction pattern tool, as shown in Figure 4.12. In addition, since the surface area is larger after the RTA process, the oxygen atoms are more likely to escape from the surface portion than the center portion due to the presence of more carbon atoms aligned in the suspended carbon nanowires. There is a similar

ratio between the suspended and the substrate-bound glassy carbon nanowire, such as electrical conductivity and surface area. In other words, the reason for improving the electrical conductivity is the decreasing oxygen atom and the increasing sp<sup>2</sup> structure after the annealing process. In addition, the ordered carbon atoms are more electrically conductive than the substrate-bonded glassy carbon nanowires because they are more present in the surface portion than the center portion of the suspended glassy carbon nanowires.

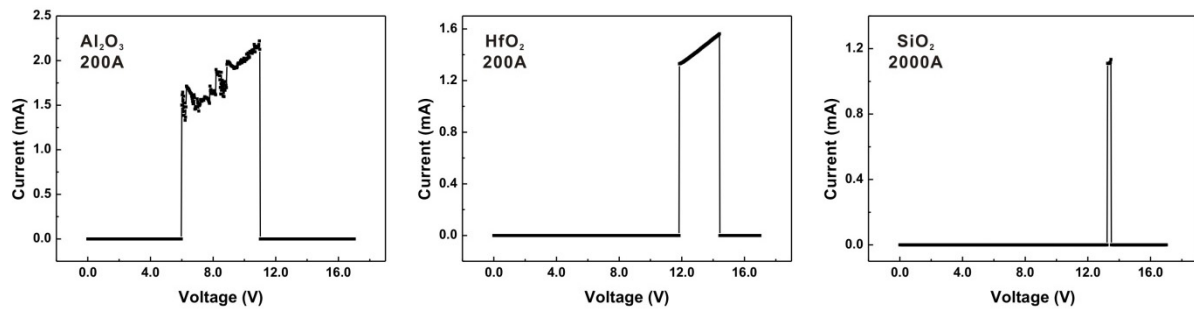


**Figure 4.13** Breaking down voltages of various insulating materials such as Al<sub>2</sub>O<sub>3</sub>, HfO<sub>2</sub>, SiO<sub>2</sub> deposited on a suspended single glassy carbon nanowire.

The insulating properties of HfO<sub>2</sub> deposited on suspended glassy carbon nanowires were characterized using measurements of the breakdown voltage. The insulating layer of the 20-nm-thick HfO<sub>2</sub> layer fabricated by the ALD process serves as a separation between the sensing part and the heating part during the electrical connection. The breakdown voltage is determined by the performance of the internal heater of the heating system. In other words, despite the excellent properties of the glassy carbon structure, it has a low breakdown voltage and can not be used in a gas sensing platform. Our breakdown voltage of the gas detection platform was measured directly in the suspended hierarchical ZnO nanowires forests/HfO<sub>2</sub>/glassy carbon nanowires, as shown in Figure 4.13. I-V characteristic shows the breakdown voltage of the HfO<sub>2</sub> layer between the suspended hierarchical ZnO nanowires forests structure and glassy carbon in the Figure 4.13. One peak

is a breakdown voltage and the other is a breakable glassy carbon nanowire. The breakdown voltage is approximately 11.82V. Other insulating materials such as SiO<sub>2</sub> and Al<sub>2</sub>O<sub>3</sub> were measured to compare the breakdown voltages of the HfO<sub>2</sub> layers we selected. SiO<sub>2</sub> material is known as an insulating material based on a MEMS process, and conducted by PECVD. Al<sub>2</sub>O<sub>3</sub> materials are also known as insulating materials and have gone through the ALD process to directly compare the insulation material of HfO<sub>2</sub>. The breakdown voltage of a 200-nm-thick SiO<sub>2</sub> material is about 13.23 V, and the 20-nm-thick Al<sub>2</sub>O<sub>3</sub> material is about 5.94 V. The breakdown voltage of the SiO<sub>2</sub> material is high, but the insulating material on this gas sensing platform has high thermal conductivity. Generally, the insulating material is low thermal conductivity. A thin insulating layer is also important to apply an insulating layer to the gas sensing platform. The insulation properties for the thickness of the HfO<sub>2</sub> material are the highest and are about 59.1 mV / nm.

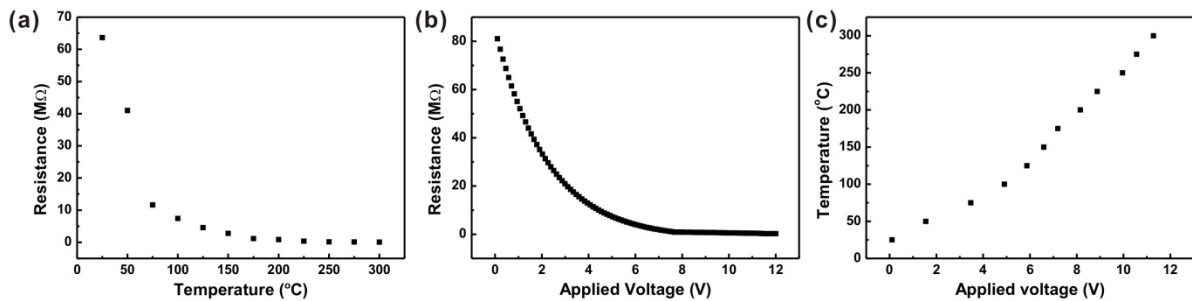


**Figure 4.14** The electrical resistance of (a) a suspended glassy carbon, (b) hierarchical ZnO nanowires forests changed by the temperature of an external heater. The electrical resistance of hierarchical ZnO nanowires forests depending on the applied voltage of a suspended glassy carbon nanowire. (d) The predicted temperature of an internal heater by the applied voltage of a suspended glassy carbon structure.

The electrical resistance of the layered ZnO nanowire is characterized by the temperature that predicts the performance of the heating structure of glassy carbon using an

external heater (see Figure 4. 14). By increasing the temperature using an external resistor, the electrical resistance has decreased exponentially. The electrical resistance was measured by the applied voltage on the suspended glassy carbon nanowires. At 9.0 V, the electrical resistance of the ZnO nanowire was about 874.18 kΩ, and an external heater was used to predict a temperature of about 200 ° C depending on the electrical resistance depending on the temperature.

Joule heating of the suspended glassy carbon nanowire was calculated by numerical simulation (COMSOL Multiphysics) [168]. The suspended glassy carbon nanowire having a thickness of 120 μm and a diameter of 300 nm were placed on a SiO<sub>2</sub>/Si substrate (1-μm-thickness SiO<sub>2</sub> deposited on the Si substrate thickness; 600-μm-thickness, area of 1.5 mm x 1.5 mm). The temperature of the SiO<sub>2</sub>/Si substrate on the top and side walls was set as insulation and the bottom was fixed at room temperature (293.15 K). The suspended glassy carbon nanowires were 59,000 S/m at room temperature and the temperature dependence of electrical conductivity was modeled as follows:

$$\sigma = \sigma_0 \frac{1}{\{1 + \alpha(T - T_0)\}} \quad (5)$$

where  $\sigma_0$  is the electrical conductivity at room temperature,  $\alpha$  is the temperature coefficient of resistance, T is the temperature, and  $T_0$  is the room temperature (293.15 K). Other material properties have been cited in the research papers [169-171]. Electrical bias was applied across the circuit and heat was generated at the suspended glassy carbon nanowire based on a Joule heating model. The heat was dissipated primarily by conductive heat transfer to the column supporting the suspended glassy carbon nanowire and by convective heat transfer to the atmospheric environment on the suspended glassy carbon nanowire device. Figure 4.15 shows the simulation results of the suspended glassy carbon

nanowire's joule heating by the numerical simulation. A maximum temperature of 523.15 K was observed at the center of the suspended glassy carbon nanowire when an electrical bias of 9 V was applied. The suspended type structure generated a lot of heat even when a small electrical bias is applied because the heat is hard to transfer convective at the air [172]. The suspended structure is an optimal structure in the power consumption part as the gas sensing platform based on the metal oxide nanowires. We compared the actual temperature with the simulated temperature based on the indirectly measured values of the electrical resistance of the ZnO nanowire grown on the suspended  $\text{HfO}_2$ /glassy carbon nanowire depending on the temperature of the oven. The temperature difference was about 20 %, and the temperature increase curve was similar between the actual temperature and the simulated temperature. This difference arises from the measurement method and could be accurately predicted if only the temperature correction is correct. This gas sensing platform is about the 1.5 mW in the power consumption and this value is the ultra-low power consumption in the gas sensing society and is suitable for the gas sensor based on the internet of things (IoT) [173].

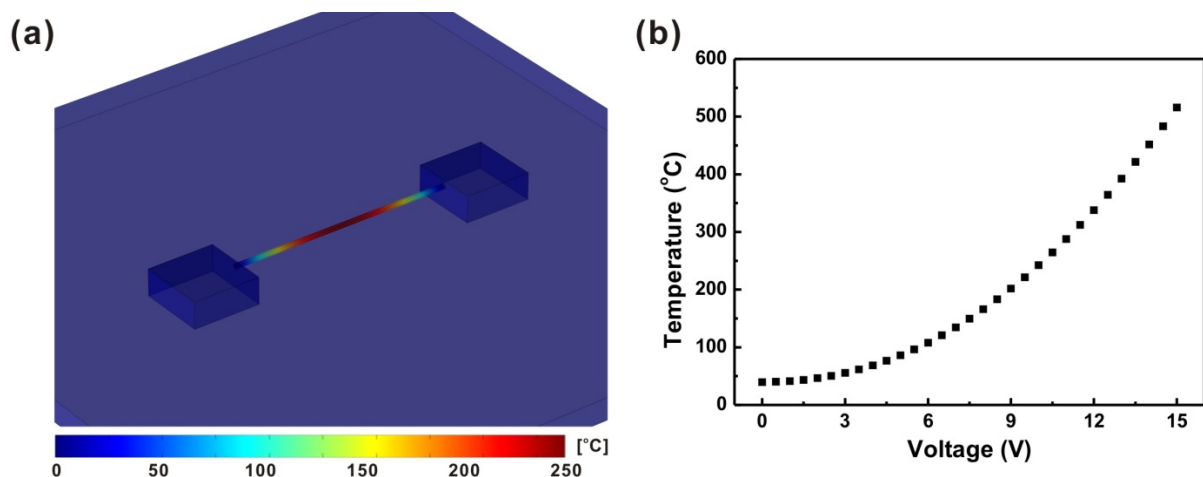


**Figure 4.15** (a) Simulation results of the temperature profile based on the Joule heating model at the suspended nano-structure. Temperature changes of the suspended nanowire depending on the applied voltage.

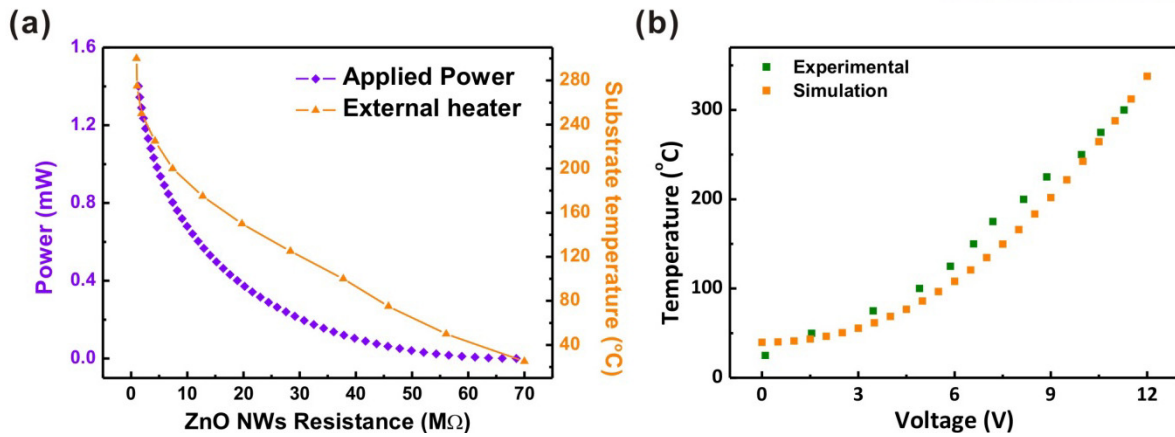


**Figure 4.16** (a) Resistance changes of ZnO nanowires forests grown on the HfO<sub>2</sub>/carbon nanowire with respect to (left) power consumption of the carbon nanowire heater and (right) temperature of the external heater. (b) Comparison of the temperature between the simulation results and experimental results at the suspended nano-structure.

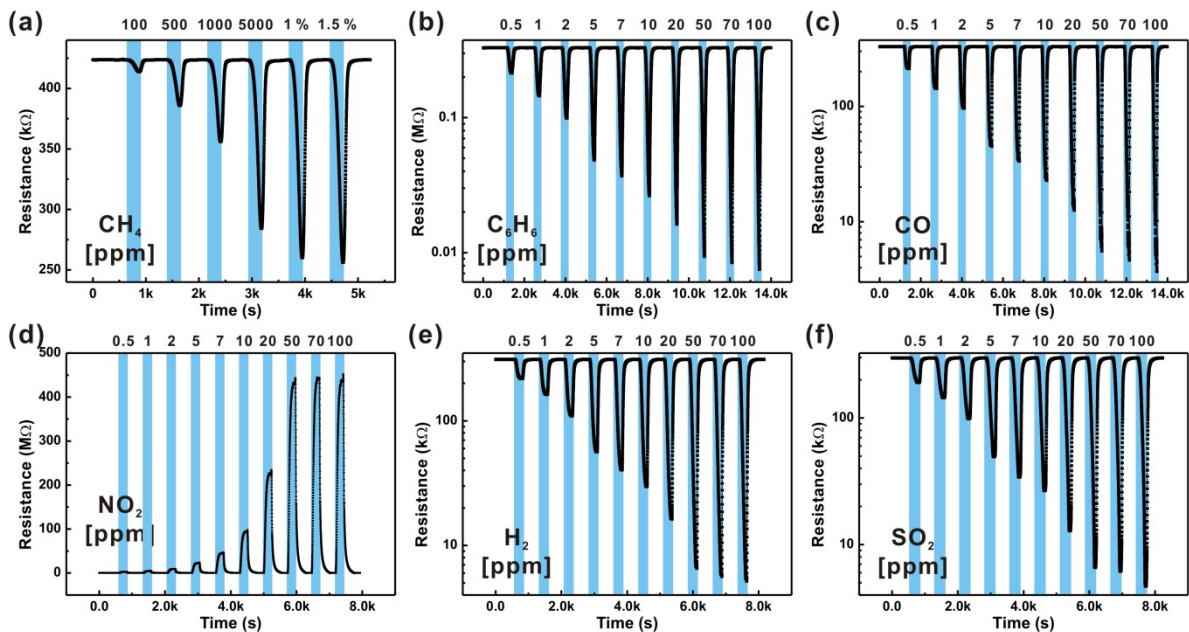


**Figure 4.17** Gas sensing characteristics of the ultralow-power consumption gas sensor of suspended hierarchical ZnO nanowire forests/HfO<sub>2</sub>/carbon nanostructure for various gases such as CH<sub>4</sub>, C<sub>6</sub>H<sub>6</sub>, CO, NO<sub>2</sub>, H<sub>2</sub> and SO<sub>2</sub> and gas concentrations mixed in dried air at 1.5-mW power heated at the suspended carbon nanostructure.



The gas sensing properties of the ultra-low power consumption gas sensing platform of the suspended hierarchical ZnO nanowires forests grown on the HfO<sub>2</sub>/glassy carbon nanowire were characterized by measuring the electrical resistance change in response to various gases and gas concentrations (NO<sub>2</sub> : 50 ppb - 500 ppm, CO, C<sub>6</sub>H<sub>6</sub>, H<sub>2</sub>, SO<sub>2</sub> : 500 ppb – 500 ppm, CH<sub>4</sub> : 100 – 1.5 %).

As shown in Figure 4.17, the electrical resistance of the suspended hierarchical ZnO nanowires forests increases with the concentration of NO<sub>2</sub> gas. The sensor showed high gas response even at very low concentration (7.36 for 50 ppb NO<sub>2</sub>). The gas response increases linearly to 500 ppm with a sensitivity of 79 ppb<sup>-1</sup> and the gas response is lower than the suspended hierarchical ZnO nanowire without the external heater because the external heater is larger than the gas sensing platform, so the mass transfer of the target gas is more increased by the external heater.

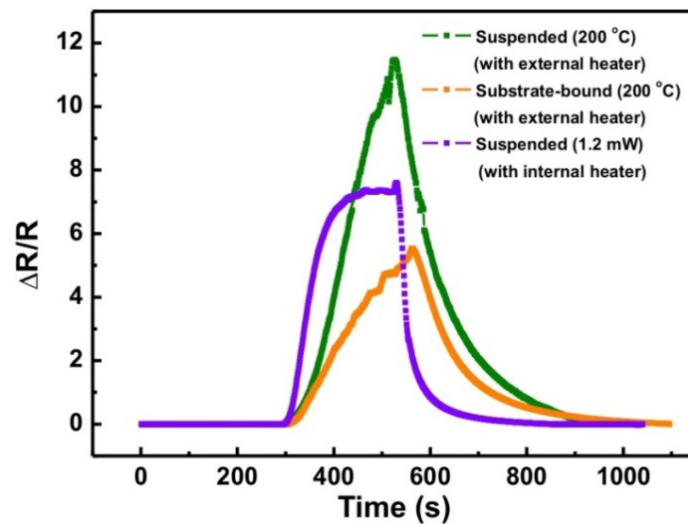


**Figure 4.18** Gas responses at 50 ppb NO<sub>2</sub> gas consisting of internal heater and external heater of a suspended and substrate-bound ZnO nanowire structure.

However, the response & recovery time is decreased. Although the mass transfer of the target gas is decreased without external heater, the heat is generated from the core at

the ultra-low power consumption gas sensing platform and the gas closed to the core is more effective transferred to the environment.

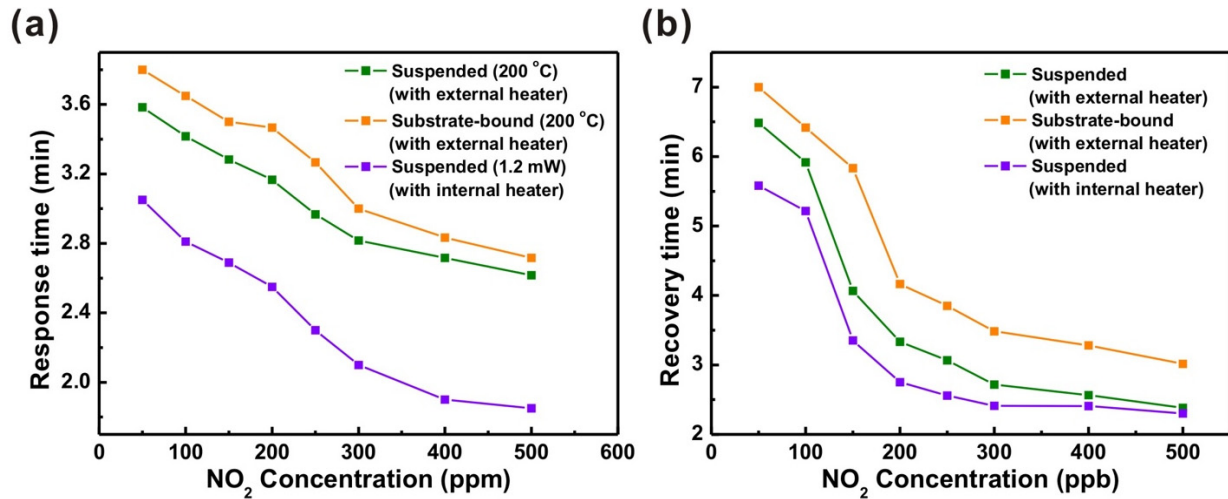


**Figure 4.19** Response time and recovery time versus various NO<sub>2</sub> gas concentration using internal and external heater (between suspended and substrate-bound structure) to compare gas sensing characteristics from 50 to 500 ppb.

The ultra-low power consumption gas sensing platform is more suitable for the gas sensing platform based on the metal oxide nanostructure than using external heater. Therefore, the ultra-low power consumption gas sensing platform is the best suspended structure effect in the mass transfer of the gases and power consumption. The ultra-low power consumption gas sensing platform based on the ZnO nanowires is the best gas response of the NO<sub>2</sub> gas. However, the other gas response without CH<sub>4</sub> is similar. To enhance the gas selectivity, the ultra-low power consumption gas sensing platform based on the ZnO, CuO nanostructure is measured the gas response depending on the operating temperature of the internal heating of the suspended glassy carbon nanowire in accordance with the various gases such as and gas concentrations. Gas response was changed by the operating temperature and materials. We suggested the multiplex gas sensing platform based on the metal oxide nanostructure to enhance the gas selectivity because metal oxide gas sensor is high response but low gas

selectivity. Only ZnO, CuO nanostructures, it is possible to make the multiplex gas sensing platform using the selectively controlling the heater performance because the gas response is changed by the operating temperature. However, although the gas response is changed by the heating performance, the difference among the gases such as CO, SO<sub>2</sub>, H<sub>2</sub>, C<sub>6</sub>H<sub>6</sub> is small. To overcome the gas selectivity based on the metal oxide gas sensing platform, we applied to the Principal component analysis (PCA). After that, it is possible to the enhanced gas selectivity.

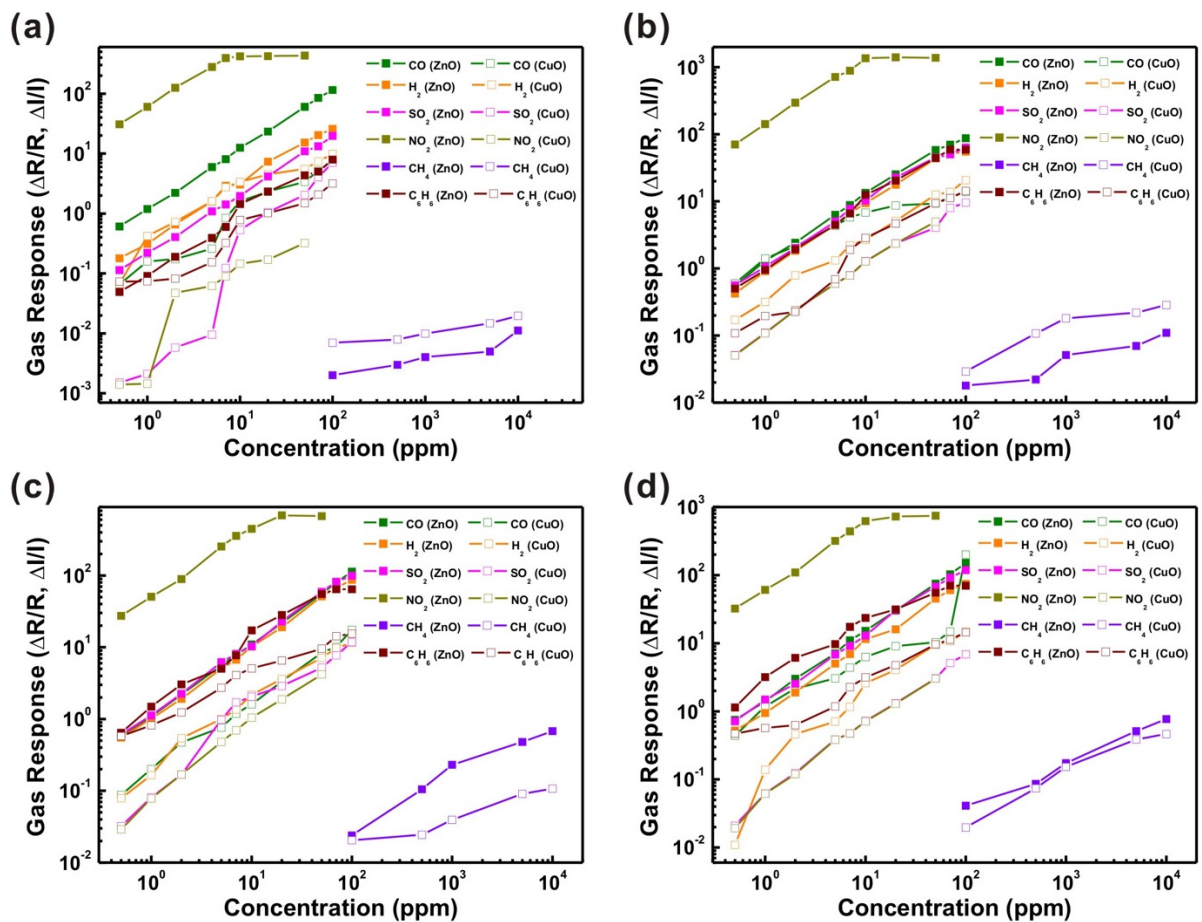


**Figure 4.20** Gas sensing characteristics of the suspended hierarchical metal oxide nanowires such as ZnO and CuO grown on selectively HfO<sub>2</sub>/carbon nanowire at various gases and gas concentrations depending on the heater power consumption such as (a) 0.8 mW, (b) 1.4 mW, (c) 2.4 mW and (d) 3.1 mW.

Gas sensing pattern recognition according to the gas concentrations of 6 gases in

the signal processing logic process, the preprocessing technique and the response characteristics analysis of single sensor and sensor array signals are required and pattern extraction is performed for each sensor signal. The 6 gas sensing arrays such as CH<sub>4</sub>, C<sub>6</sub>H<sub>6</sub>, CO, H<sub>2</sub>, NO<sub>2</sub>, SO<sub>2</sub> were tested and the data set, which is the experimental results, was measured according to the gas concentrations.

Gas response using relative parameter

Data set  $[i, j] = A_{ij}$

( $i$  = Number of gas response according to the target gas,  $j$  = Number of gas sensor)

**Table 5.** Relative parameters ( $R_g/R_a$ ) of 6 gas sensor array for the target gas response.

Temperature Gas [ppm]		ZnO nanowire				CuO nanoflake			
		150	200	250	300	150	200	250	300
CO	0.5	0.623	0.646	0.638	0.572	1.066	1.601	1.088	1.437
	1	0.457	0.434	0.480	0.417	1.159	2.413	1.201	2.183
	2	0.310	0.293	0.313	0.250	1.174	3.135	1.474	3.165
	5	0.144	0.137	0.152	0.124	1.259	5.311	1.759	4.038
	7	0.110	0.102	0.113	0.083	1.844	6.774	2.184	5.374
	10	0.074	0.069	0.084	0.062	2.599	7.796	2.599	7.282
	20	0.041	0.038	0.044	0.032	3.324	9.694	4.332	10.028
	50	0.016	0.017	0.018	0.013	4.384	10.337	9.438	11.339
	70	0.012	0.014	0.012	0.010	6.166	12.600	11.166	15.865
100	0.009	0.011	0.009	0.007	8.592	14.782	18.592	200.581	
H <sub>2</sub>	0.5	0.848	0.703	0.645	0.657	1.067	1.171	1.079	1.011
	1	0.763	0.525	0.497	0.514	1.420	1.318	1.166	1.138
	2	0.603	0.354	0.344	0.346	1.727	1.789	1.540	1.462
	5	0.385	0.183	0.165	0.166	2.604	2.320	2.001	1.705
	7	0.257	0.131	0.130	0.126	3.757	3.209	2.354	2.165
	10	0.246	0.097	0.089	0.080	4.365	3.677	3.185	3.594
	20	0.120	0.053	0.050	0.059	5.492	6.139	4.609	5.062
	50	0.062	0.022	0.019	0.022	6.555	13.592	8.123	10.570
	70	0.047	0.019	0.015	0.016	8.398	14.818	10.727	11.723
100	0.037	0.018	0.011	0.013	10.843	21.738	12.612	15.639	
SO <sub>2</sub>	0.5	0.898	0.640	0.620	0.585	1.002	1.051	1.032	1.021
	1	0.819	0.485	0.471	0.401	1.002	1.110	1.081	10.062
	2	0.712	0.331	0.308	0.282	1.006	1.239	1.169	1.124
	5	0.478	0.166	0.139	0.128	1.010	1.595	1.982	1.387
	7	0.415	0.114	0.110	0.099	1.123	1.790	2.703	1.475
	10	0.336	0.089	0.088	0.072	1.529	2.281	3.046	1.721
	20	0.194	0.042	0.042	0.032	2.048	3.371	3.892	2.311
	50	0.084	0.022	0.017	0.014	3.046	5.041	6.232	4.056
	70	0.070	0.020	0.012	0.011	5.044	8.972	8.710	6.119
100	0.048	0.015	0.010	0.008	8.039	10.559	12.872	7.879	
NO <sub>2</sub>	0.5	31.927	71.65	28.34	33.32	0.999	0.952	0.972	0.981
	1	61.311	143.04	51.468	61.46	0.999	0.902	0.927	0.942
	2	126.118	297.60	90.360	110.33	0.955	0.807	0.856	0.893
	5	280.310	715.92	254.40	320.35	0.942	0.628	0.676	0.723
	7	393.978	890.15	356.76	440.41	0.918	0.559	0.589	0.678
	10	419.540	1362.71	447.80	620.31	0.873	0.439	0.489	0.584
	20	424.793	1399.35	692.60	724.51	0.855	0.298	0.347	0.436
	50	433.910	1380.95	674.40	746.37	0.757	0.167	0.193	0.249
CH <sub>4</sub>	100	0.998	0.982	0.977	0.961	1.010	1.029	1.021	1.020
	500	0.997	0.978	0.905	0.921	1.008	1.107	1.024	1.074
	1000	0.998	0.951	0.812	0.853	1.007	1.180	1.039	1.153
	5000	0.995	0.935	0.675	0.662	1.015	1.219	1.091	1.387
	10000	0.999	0.901	0.595	0.565	1.020	1.286	1.107	1.465
C <sub>6</sub> H <sub>6</sub>	0.5	0.953	0.665	0.609	0.467	1.074	1.109	1.579	1.470
	1	0.916	0.512	0.402	0.239	1.074	1.195	1.816	1.567
	2	0.840	0.342	0.248	0.141	1.082	1.225	2.233	1.627
	5	0.718	0.183	0.165	0.094	1.154	1.691	3.725	2.181
	7	0.625	0.131	0.114	0.055	1.323	2.905	5.111	3.261
	10	0.410	0.074	0.055	0.041	1.781	3.851	6.070	4.148
	20	0.300	0.047	0.034	0.031	2.012	5.671	7.543	5.779
	50	0.188	0.022	0.018	0.018	2.489	10.361	10.583	10.644
	70	0.167	0.017	0.015	0.014	3.078	12.251	15.254	12.356
100	0.112	0.017	0.015	0.014	4.163	15.301	16.500	15.487	

Each gas sensor responds to the gas concentration of the test gases. Gas response of the ultra-low power consumption gas sensor array for the experimental results is shown in the form of  $R_g/R_a$ , as shown in the Table 4. Where  $R_g$  is the resistance to the test gas and  $R_a$  is the resistance of the sensor in dry air. Gas response of the gas sensor array is important for analyzing the output signals of metal-oxide gas sensors because it could display the linearity of sensors according to the gas concentrations. However, in order to clearly indicate the relative gas sensitivity and selectivity of the gas sensors with respect to the target gas and to extract the pattern form of the sensors for the sensing gas for gas recognition, it is necessary to preliminarily process individual sensor signals and pre-processing is needed.

Gas response of each gas sensor arrays with respect to the target gas would be expressed using the equation using the logarithm of the gas response among the method for indicating the gas sensitivity of each gas sensor with respect to the target gas.

$$S_{ij} = \ln \left| \frac{R_g}{R_a} \right| \quad (5)$$

where  $S_{ij}$  is relative sensitivity,  $i$  is number of gas response to the target gas and  $j$  is number of the gas sensor. Each gas response (relative sensitivity) for the tested gas shown in Table 5 above would be expressed as relative sensitivity to the tested gases using the equation (5), as shown in Table 5. Table 5 shows the relative sensitivity of each sensor in the gas sensor array depending on the gas concentrations of various gases.

**Table 6.** Relative sensitivities ( $S_{ij}$ ) of gas sensor array to the tested gases.

Temperature Gas [ppm]		ZnO nanowire				CuO nanoflake			
		150	200	250	300	150	200	250	300
CO	0.5	0.474	0.436	0.449	0.559	0.063	0.470	0.084	0.362
	1	0.783	0.834	0.734	0.874	0.147	0.881	0.183	0.781
	2	1.170	1.228	1.162	1.387	0.161	1.143	0.388	1.152
	5	1.940	1.987	1.881	2.090	0.230	1.670	0.565	1.396
	7	2.206	2.285	2.177	2.486	0.612	1.913	0.781	1.682
	10	2.603	2.670	2.479	2.783	0.955	2.054	0.955	1.985
	20	3.188	3.266	3.120	3.434	1.201	2.271	1.466	2.305
	50	4.112	4.078	4.036	4.331	1.478	2.336	2.245	2.428
	70	4.456	4.261	4.398	4.640	1.819	2.534	2.413	2.764
100	4.755	4.485	4.737	5.023	2.151	2.693	2.923	5.301	
H <sub>2</sub>	0.5	0.165	0.353	0.439	0.420	0.064	0.158	0.076	0.011
	1	0.270	0.645	0.699	0.665	0.351	0.276	0.153	0.130
	2	0.507	1.040	1.066	1.061	0.546	0.582	0.432	0.380
	5	0.955	1.700	1.800	1.796	0.957	0.842	0.694	0.533
	7	1.360	2.035	2.043	2.069	1.324	1.166	0.856	0.773
	10	1.401	2.338	2.417	2.527	1.474	1.302	1.158	1.279
	20	2.118	2.929	2.998	2.829	1.703	1.815	1.528	1.622
	50	2.786	3.805	3.957	3.835	1.880	2.609	2.095	2.358
	70	3.063	3.948	4.222	4.115	2.128	2.696	2.373	2.462
100	3.294	4.028	4.480	4.324	2.383	3.079	2.535	2.750	
SO <sub>2</sub>	0.5	0.108	0.447	0.478	0.537	0.001	0.050	0.031	0.021
	1	0.200	0.723	0.754	0.913	0.002	0.104	0.078	2.309
	2	0.340	1.107	1.178	1.265	0.006	0.214	0.156	0.117
	5	0.738	1.797	1.974	2.057	0.009	0.467	0.684	0.327
	7	0.880	2.169	2.208	2.316	0.116	0.582	0.994	0.389
	10	1.089	2.424	2.431	2.633	0.425	0.825	1.114	0.543
	20	1.639	3.164	3.174	3.448	0.717	1.215	1.359	0.838
	50	2.478	3.832	4.099	4.234	1.114	1.618	1.830	1.400
	70	2.653	3.932	4.415	4.528	1.618	2.194	2.164	1.811
100	3.031	4.168	4.610	4.782	2.084	2.357	2.555	2.064	
NO <sub>2</sub>	0.5	3.463	4.272	3.344	3.506	0.001	0.049	0.029	0.019
	1	4.116	4.963	3.941	4.118	0.001	0.103	0.075	0.060
	2	4.837	5.696	4.504	4.703	0.046	0.214	0.156	0.113
	5	5.636	6.574	5.539	5.769	0.060	0.465	0.392	0.324
	7	5.976	6.791	5.877	6.088	0.085	0.581	0.529	0.389
	10	6.039	7.217	6.104	6.430	0.136	0.822	0.716	0.538
	20	6.052	7.244	6.540	6.585	0.157	1.211	1.057	0.829
	50	6.073	7.231	6.514	6.615	0.279	1.790	1.646	1.390
	100	0.002	0.018	0.024	0.040	0.010	0.029	0.020	0.019
CH <sub>4</sub>	500	0.003	0.022	0.100	0.083	0.008	0.102	0.024	0.071
	1000	0.002	0.050	0.208	0.160	0.007	0.166	0.039	0.142
	5000	0.005	0.068	0.393	0.412	0.015	0.198	0.087	0.327
	10000	0.001	0.104	0.519	0.571	0.019	0.251	0.102	0.382
	0.5	0.048	0.407	0.496	0.762	0.071	0.103	0.457	0.386
C <sub>6</sub> H <sub>6</sub>	1	0.087	0.669	0.912	1.429	0.072	0.178	0.597	0.449
	2	0.174	1.073	1.396	1.961	0.079	0.203	0.803	0.487
	5	0.331	1.697	1.802	2.368	0.143	0.525	1.315	0.780
	7	0.470	2.031	2.168	2.909	0.280	1.066	1.631	1.182
	10	0.891	2.604	2.898	3.199	0.577	1.348	1.803	1.423
	20	1.203	3.063	3.374	3.479	0.699	1.735	2.021	1.754
	50	1.673	3.815	4.031	4.034	0.912	2.338	2.359	2.365
	70	1.790	4.093	4.176	4.265	1.124	2.506	2.725	2.514
100	2.188	4.094	4.182	4.263	1.426	2.728	2.803	2.740	

Gas response of the individual gas sensors has shown that they response well the tested gases. However, the gas sensitivity in the use of real gas sensors varies linearly with the gas concentrations and it is difficult to distinguish the signals of the gas sensor according to the distribution of experimental results owing to different range of gas sensing signals. This makes it difficult to extract a pattern showing the nature of the tested gas for the gas sensors, and does not have sufficient gas selectivity when applying n algorithm that recognizes the target gas. In order to solve these problems and enhance the gas selectivity, it is necessary to (1) limit the range of the gas response to individual gas sensors, (2) to remove noise from the individual gas sensors, and (3) the following normalization algorithm is used for pattern extraction (concentration independent).

$$S'_{ij} = \frac{S_{ij}}{\sum_{i=1}^n S_n} \quad (5)$$

where  $S_{ij}$  is % normalization response,  $i$  is number of gas response to the target gas and  $j$  is number of the gas sensor. The gas sensitivity of the sensor are calculated from the normalized pattern data for the target gases, as shown in Table 6 through the above normalization algorithm.



**Table 7.** Normalized pattern data by preprocessing of gas sensor array signals.

Temperature Gas [ppm]		ZnO nanowire				CuO nanoflake			
		150	200	250	300	150	200	250	300
CO	0.5	0.163	0.151	0.155	0.193	0.022	0.162	0.029	0.125
	1	0.150	0.160	0.141	0.168	0.028	0.169	0.035	0.150
	2	0.150	0.158	0.149	0.178	0.021	0.147	0.050	0.148
	5	0.165	0.169	0.160	0.178	0.020	0.142	0.048	0.119
	7	0.156	0.162	0.154	0.176	0.043	0.135	0.055	0.119
	10	0.158	0.162	0.150	0.169	0.058	0.125	0.058	0.120
	20	0.157	0.161	0.154	0.170	0.059	0.112	0.072	0.114
	50	0.164	0.163	0.161	0.173	0.059	0.093	0.090	0.097
	70	0.163	0.156	0.161	0.170	0.067	0.093	0.088	0.101
100	0.148	0.140	0.148	0.157	0.067	0.084	0.091	0.165	
H <sub>2</sub>	0.5	0.098	0.209	0.260	0.249	0.038	0.094	0.045	0.006
	1	0.085	0.202	0.219	0.209	0.110	0.087	0.048	0.041
	2	0.090	0.185	0.190	0.189	0.097	0.104	0.077	0.068
	5	0.103	0.183	0.194	0.194	0.103	0.091	0.075	0.058
	7	0.117	0.175	0.176	0.178	0.114	0.100	0.074	0.066
	10	0.101	0.168	0.174	0.182	0.106	0.094	0.083	0.092
	20	0.121	0.167	0.171	0.161	0.097	0.103	0.087	0.092
	50	0.119	0.163	0.170	0.164	0.081	0.112	0.090	0.101
	70	0.122	0.158	0.169	0.165	0.085	0.108	0.095	0.098
100	0.123	0.150	0.167	0.161	0.089	0.115	0.094	0.102	
SO <sub>2</sub>	0.5	0.064	0.267	0.286	0.321	0.001	0.030	0.019	0.012
	1	0.039	0.142	0.148	0.180	0.000	0.021	0.015	0.454
	2	0.078	0.253	0.269	0.289	0.001	0.049	0.036	0.027
	5	0.092	0.223	0.245	0.255	0.001	0.058	0.085	0.041
	7	0.091	0.225	0.229	0.240	0.012	0.060	0.103	0.040
	10	0.095	0.211	0.212	0.229	0.037	0.072	0.097	0.047
	20	0.105	0.203	0.204	0.222	0.046	0.078	0.087	0.054
	50	0.120	0.186	0.199	0.205	0.054	0.079	0.089	0.068
	70	0.114	0.169	0.189	0.194	0.069	0.094	0.093	0.078
100	0.118	0.162	0.180	0.186	0.081	0.092	0.100	0.080	
NO <sub>2</sub>	0.5	0.236	0.291	0.228	0.239	0.000	0.003	0.002	0.001
	1	0.237	0.286	0.227	0.237	0.000	0.006	0.004	0.003
	2	0.239	0.281	0.222	0.232	0.002	0.011	0.008	0.006
	5	0.228	0.265	0.224	0.233	0.002	0.019	0.016	0.013
	7	0.227	0.258	0.223	0.231	0.003	0.022	0.020	0.015
	10	0.216	0.258	0.218	0.230	0.005	0.029	0.026	0.019
	20	0.204	0.244	0.220	0.222	0.005	0.041	0.036	0.028
	50	0.193	0.229	0.207	0.210	0.009	0.057	0.052	0.044
	100	0.012	0.110	0.146	0.248	0.061	0.177	0.126	0.120
CH <sub>4</sub>	500	0.007	0.053	0.242	0.200	0.019	0.247	0.058	0.173
	1000	0.003	0.064	0.269	0.207	0.009	0.215	0.050	0.184
	5000	0.003	0.045	0.261	0.274	0.010	0.132	0.058	0.217
	10000	0.001	0.054	0.266	0.293	0.010	0.129	0.052	0.196
	0.5	0.018	0.149	0.182	0.279	0.026	0.038	0.167	0.141
C <sub>6</sub> H <sub>6</sub>	1	0.020	0.152	0.208	0.325	0.016	0.041	0.136	0.102
	2	0.028	0.174	0.226	0.318	0.013	0.033	0.130	0.079
	5	0.037	0.189	0.201	0.264	0.016	0.059	0.147	0.087
	7	0.040	0.173	0.185	0.248	0.024	0.091	0.139	0.101
	10	0.060	0.177	0.197	0.217	0.039	0.091	0.122	0.096
	20	0.069	0.177	0.195	0.201	0.040	0.100	0.117	0.101
	50	0.078	0.177	0.187	0.187	0.042	0.109	0.110	0.110
	70	0.077	0.176	0.180	0.184	0.048	0.108	0.117	0.108
	100	0.090	0.168	0.171	0.175	0.058	0.112	0.115	0.112

To analyze gas mixture data using pattern recognition algorithm, gas sensor signal patterns for mixed gas were extracted and principal PCA was applied. PCA is one of the multivariate data processing method that reduce dimension to low dimension while maintaining information at high dimension for experimental results consisting of multidimensional feature vectors. The feature data is expressed based on a reference axis existing as many as the number of dimensions of the feature vector. Two-dimensional data are expressed based on two reference axes. As a result, reducing the dimension could be thought of as reducing the number of reference axis. To reduce 10-dimensional data to 4 dimensions, it means to reduce the reference axis from 10 to 4. Therefore, the principal axis corresponding to the principal component of the multivariate data could be obtained by statistical methods, and the dimension could be reduced by projecting the feature vector  $x$  in the direction of the obtained main axis.

PCA refers to relocating the feature vector by transforming the reference axis into a set of uncorrelated variables from the perspective of reducing the variance of the correlated variables. The method and sequence of pattern recognition algorithm applying PCA applied to this paper are summarized in Table 7.

**Table 8.** Pattern recognition algorithms with the PCA process.

No	Vale	Equation	Purpose
1	Normalizing data	$S_{ij} = \ln \left  \frac{R_g}{R_a} \right $ $S'_{ij} = \frac{S_{ij}}{\sum_{i=1}^n S_n} \times 100[\%]$	Data acquisition and pre-processing
↓			
2	Average vector [ $\mu$ ]	$\mu = \frac{1}{N} \sum_{n=1}^N x_n$	The average vector calculation of the obtained data
↓			
3	Covariance Matrix [ $\Sigma$ ]	$\Sigma = \sum_{n=1}^N (x_n - \mu)(x_n - \mu)^T$	Covariance matrix calculation
↓			
4	Eigenvalue and Eigen vector [ $\lambda$ ], [ $u$ ]	$\Sigma = U \Lambda U^T$	Eigen vector calculation
↓			
5	Feature Vector [ $u$ ]	Selecting the 2 values of eigen vector	Feature vector configuration
↓			
6	Final Data	$\{\text{Final Data}\} = \{\text{Row Feature Vector}\} \\ * \{\text{Row Data Adjust}\}$	Final data calculation
↓			
7	Principal value plot		

As shown in Figure 4.20, PCA plots in this system are well discriminated against the six gases in the system. Therefore, through the gas sensor array, 6 kinds of gas could be separated through the PCA and the disadvantage of metal oxide gas sensor can be overcome.

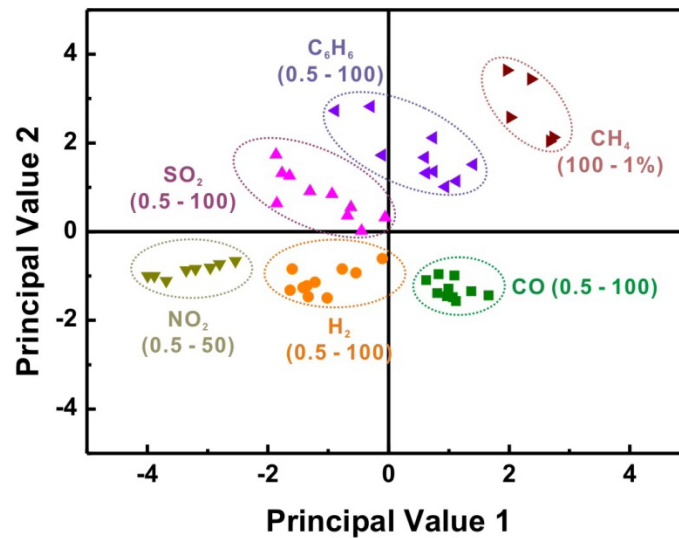


**Figure 4.21** Discrimination of six gases by the ultralow-power consumption gas sensor at four temperatures using static response.

Environmental humidity is an important factor affecting the performance of metal oxide gas sensors by the development of many humidity gas sensors based on metal oxides. Details of the adsorption of water on the surface of metal oxide nanostructures and the mechanism of sensing water vapor could be seen in [174-175]. Water adsorbing on the metal oxide does not donate electrons to the sensing layers. The reaction between surface oxygen and water molecules reduces the baseline resistance of the gas sensor, and results in a decrease of the gas response. Moisture adsorption significantly reduces the gas response of the metal oxide gas sensing platforms, as shown in Figure 4.22. Furthermore, prolonged exposure to a humid environment will gradually form chemically adsorbed  $OH^-$  on the surface of the metal oxide nanostructures, causing a gradual deterioration of the gas response of the gas sensor [175]. However, the surface hydroxyl groups could be removed by starting

desorption at about 400 °C and heating the hydroxyl ion to a temperature of 400 °C or higher. The ultra-low power consumption gas sensing platform based on the ZnO nanowire measured the gas response in the 1-ppm-NO<sub>2</sub> depending on the humidity. Gas response is decreased at 50.3 % in the 85 %-RH better than the 35 %-RH. To remove the OH<sup>-</sup> on the surface of the metal oxide nanostructure, the suspended glassy carbon nano-heater was applied to the electrical voltage at about 12 V for 2 minutes, and then the gas response of the ultra-low power consumption gas sensing platform was measured again, and the initial state was returned.

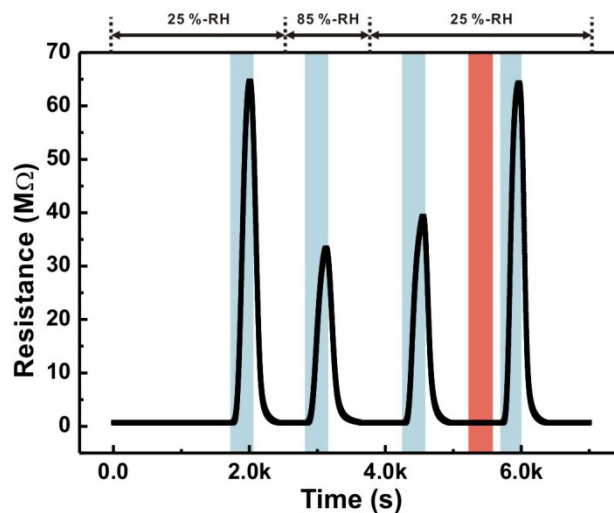


**Figure 4.22** Influence of humidity response to nitrogen dioxide. Real time difference of gas response depending on humidity and overcoming gas response through heating.

The long-term stability of the ultra-low power consumption gas sensing platform was also investigated by measuring gas response at 500 ppb NO<sub>2</sub> for 7 days test period as shown in Figure 4.22. The base resistances (the resistance before the gas injection) and the resistance changes at 500 ppb NO<sub>2</sub> of a suspended sensor did not change significantly for 1-month test period. In the long-term stability test, the sensor was stored in the air without humidity control. The suspended nanowire type sensor exhibited good stability. During the stability test, the sensor was stored in the air without humidity control. This confirms the

practical applicability of the presented sensor.

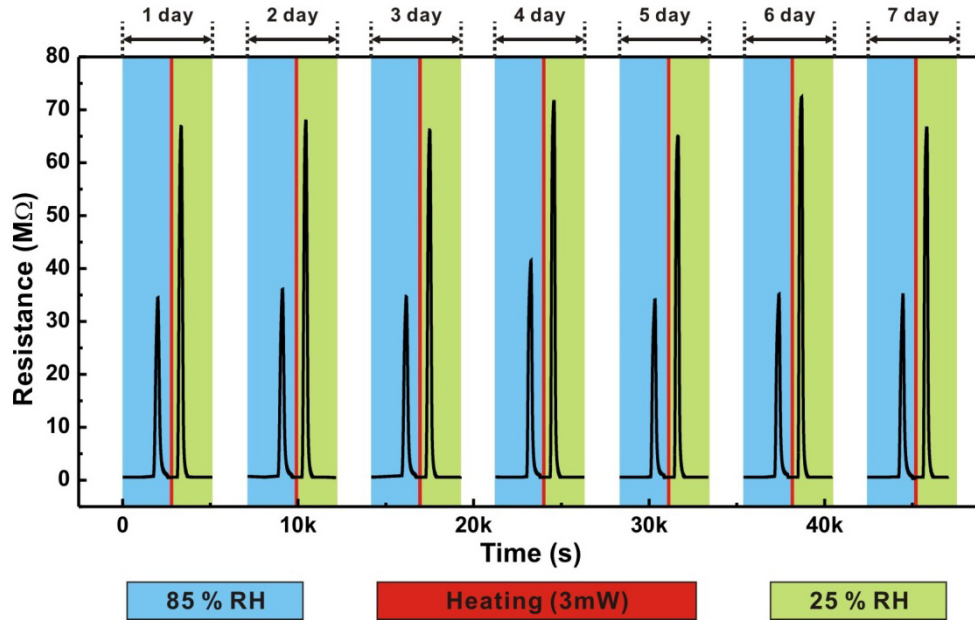


**Figure 4.23** Long-term stability of the ultralow-power-consumption gas sensor based on suspended 1D metal oxide nanostructure: the gas response and recovery behaviors for 500 ppb NO<sub>2</sub> were tested for a period of 7 days.

# 5

## Conclusions

*Finally, conclusion of this thesis will be  
recapitulated in this chapter*

## 5 Conclusions

In this thesis, a new metal oxide nanowire based gas sensor having ultralow power consumption at a suspended carbon nanowire structure was developed. This sensing platform was fabricated using only wafer level batch manufacturing processes such as carbon-MEMS, atomic layer deposition, and hydrothermal growth processes. Carbon-MEMS process consists of UV-lithography and the pyrolysis. The pyrolysis process involves significant volume reduction and converts the photoresist micro-structure to a glassy carbon nano-structure. Glassy carbon has many advantages such as high thermal and chemical stability, low density and good hardness, thermal & electrical conductivity. However, to complement or replace other carbon allotropes such as graphite, CNT, and graphenes, the electrical conductivity of glassy carbon must be improved. A simple RTA process has been developed that could greatly improve the electrical conductivity of 1D glassy carbon nano-structures produced using carbon-MEMS. To separate the suspended glassy carbon nano-heater and the suspended hierarchical metal oxide nano-structures forests, the insulating layer of the  $\text{HfO}_2$  material is uniformly deposited using an ALD process on the suspended glassy carbon nano-heater. The suspended hierarchical metal oxide nanostructured forests were grown circumferentially on the suspended  $\text{HfO}_2$ /glassy carbon nanowire using a hydrothermal method consisting of seed deposition and growth processes. In the case of the selective metal oxide seed layer deposition process, a short time exposed polymer patterning process was performed using a positive photoresist. After the polymer patterning process, a metal oxide seed layer is deposited using an rf-sputtering system and then a metal oxide nanostructure growth process is performed. The distinguishing architecture of a suspended hierarchical metal oxide nanostructures forests/ $\text{HfO}_2$ /glassy carbon nanostructure ensures efficient mass transport to the metal oxide nanostructure detection points in the gas analyte,



enabling highly sensitive gas detection. In the absence of an external heating system, the ultralow-power-consumption gas sensing platform of a suspended hierarchical 1D metal oxide nanostructures forests/HfO<sub>2</sub>/glassy carbon nanostructure has excellent the gas sensing characteristics.

## REFERENCES

- [1] F. Patolsky, and C. M. Lieber, “Nanowire nanosensors”, *Mater. Today*, vol. 8, pp. 20-28 (2005).
- [2] Z. Wang, S. Lee, K. Koo, and K. Kim, “Nanowire-based sensors for biological and medical applications”, *IEEE Trans Nanobioscience*, vol. 15, pp. 186-199 (2016).
- [3] Y. Cui, Z. Zhong, D. Wang, W. U. Wang, and C. M. Lieber, “High performance silicon nanowire field effect transistors”, *Nano Lett.*, vol. 3, pp. 149-152 (2003).
- [4] M. C. McAlpine, R. S. Friedman, S. Jin, K. Lin, W. U. Wang, and C. M. Lieber, “High-performance nanowire electronics and photonics on glass and plastic substrate”, *Nano Lett.*, vol. 3, pp. 1531-1535 (2003).
- [5] I. Mirebeau, I. N. Goncharenko, P. Cadavez-Peres, S. T. Bramwell, M. J. P. Gingras, and J. S. Gardner, “Pressure-induced crystallization of a spin liquid”, *Nature*, vol. 420, pp. 54-57 (2002).
- [6] Y. Huang, X. Duan, Y. Cui, and C. M. Lieber, “Gallium nitride nanowire nanodevices”, *Nano Lett.*, vol. 2, pp. 101-104 (2002).
- [7] Z. Zhong, D. Wang, Y. Cui, M. W. Bockrath, and C. M. Lieber, “Nanowire crossbar arrays as address decoders for integrated nanosystem”, *Science*, vol. 302 pp.1377 (2003).
- [8] Y. Cui, Q. Wei, H. Park and C. M. Lieber, “Nanowire nanosensors for highly sensitive and selective detection of biological and chemical species”, *Science*, vol. 293, pp. 1289 (2001).
- [9] V. Cimalla, M. Stubenrauch, F. Weise, M. Fischer, K. Tonisch, M. Hoffmann, and P. Ambacher, “Suspended nanowire web”, *Appl. Phys. Lett.*, vol. 90, 101504 (2007).

- [10] F. Zhang, Y. Jiang, X. Liu, J. Meng, P. Zhang, H. Liu, G. Yang, G. Li, L. Jiang, L. Wan, J. Hu, and S. Wang, "Hierarchical nanowire arrays as three-dimensional fractal nanobiointerfaces for high efficient capture of cancer cells", *Nano Lett.*, vol. 16, pp. 766-772 (2016).
- [11] K. M. Lee, S. W. Jung, K. S. Shin, W. H. Kim, M. H. Lee, and W. K. Seong, "Fabrication of suspended silicon nanowire arrays", *Small*, vol. 4, pp. 642-648 (2008).
- [12] H. Wu, Y. Gao, and H. Li, "Controlled synthesis of nickel phosphate hexahedral and flower-like architectures via a simple template-free hydrothermal route", *Cryst. Eng. Comm.*, vol. 12, pp. 3607-3611 (2010).
- [13] J. Choi, and J. Kim, "Highly sensitive hydrogen sensor based on suspended, functionalized single tungsten nanowire bridge", *Sens. Actuators B-Chem.*, vol. 136, pp. 92-98 (2009).
- [14] B. D. Gates, "Self-assembly: Nanowires find their place", *Nat. Nanotech.*, vol. 5, pp.484-485 (2010).
- [15] K. Subannajui, F. Guder, J. Danhof, A. Menzel, Y. Yang, L. Kirste, C. Wang, V. Cimalla, U. Schwarz and M. Zacharias, "An advanced fabrication method of highly ordered ZnO nanowire arrays on silicon substrates by atomic layer deposition", *Nanotechnology*, vol. 23, 235607 (2012).
- [16] T. Stoica, R. Meijers, R. Calarco, T. Richter, and H. Luth, "MBE growth optimization of InN nanowires", *J. Cryst. Growth*, vol. 290, pp. 241-247 (2006).
- [17] H. C. Kuo, T. S. Oh, and P. -C. Ku, "MOCVD growth of vertically aligned InGaN nanowires", *J. Cryst., Growth*, vol. 370, pp. 311-313 (2013).

- [18] R. Juhasz, N. Elfstrom, and J. Linnros, “Controlled fabrication of silicon nanowires by electron beam lithography and electrochemical size reduction”, *Nano Lett.*, vol. 5, pp. 275-280 (2005).
- [19] D. J. Finn, M. Lotya, and J. N. Coleman, “Inkjet printing of silver nanowire networks”, *ACS Appl. Mater. Interfaces*, vol. 7, pp. 9254-9261 (2015).
- [20] T. Martensson, P. Carlberg, M. Borgstrom, L. Montelius, W. Seifert, and L. Samuelson, “Nanowire arrays defined by nanoimprint lithography”, *Nano Lett.*, vol. 4, pp. 699-702 (2004).
- [21] D. Choi, K. Lee, and J. Y. Kim, “Nanotransfer molding of free-standing nanowire and porous nanomembranes suspended on microtrenches”, *ACS Appl. Mater. Interfaces*, vol. 5, pp. 418-424 (2013).
- [22] K. S. Novoselov, A. K. Geim, S. V. Morozov, D. Jiang, Y. Zhang, S. V. Dubonos, I. V. Grigorieva, and A. A. Firsov, “Electric field effect in atomically thin carbon films”, *Science*, vol. 306, pp. 666-669 (2004).
- [23] K. Chung, C. H. Lee, and G. C. Yi, “Transferable GaN layers grown on ZnO-coated graphene layers for optoelectronic devices”, *Science*, vol. 330, pp. 655-657 (2010).
- [24] C. Li, L. Zhao, Y. Mao, W. Wu, and J. Xu, “Focused-ion-beam induced Rayleigh-plateau instability for diversiform suspended nanostructure fabrication”, *Sci. Rep.*, vol. 5, 8236 (2015).
- [25] S. Iijima, “Helical microtubules of graphitic carbon”, *Nature*, vol. 354, pp. 56-58 (1991).
- [26] C. Staii, and A. T. Johnson, Jr., “DNA-decorated carbon nanotubes for chemical sensing”, *Nano Lett.*, vol. 5, pp. 1774-1778 (2005).

- [27] Y. Lin, L. Zhang, H. Mao, P. Chow, Y. Xiao, M. Baldini, J. Shu, and W. L. Mao, “Amorphous diamond: A high-pressure superhard carbon allotrope”, *Phys. Rev. Lett.*, vol. 107, 175504 (2011).
- [28] J. K. Luo, A. J. Flewitt, S. M. Spearing, N. A. Fleck, and W. I. Milne, “Comparison of microtweezers based on three lateral thermal actuator configurations”, *J. Micromech. Microeng.*, vol. 15, pp. 1294-1302 (2005).
- [29] A. Shah, P. Stenberg, L. Karvonen, R. Ali, S. Honkanen, H. Lipsanen, N. Peyghambarian, M. Kuittinen, Y. Svirko, and T. Kaplas, “Pyrolytic carbon coated black silicon”, *Sci. Rep.*, vol. 7, 25922 (2016).
- [30] F. C. Cowlard, and J. C. Lewis, “Vitreous carbon – A new form of carbon”, *J. Mater. Sci.*, vol. 2, pp. 507-512 (1967).
- [31] C. Wang, G. Jia, L. H. Taherabadi, and M. J. Madou, “A novel method for the fabrication of high-aspect ratio C-MEMS structures”, *J. Microelectromech. Syst.*, vol. 14, pp. 348-358 (2005).
- [32] P. J. F. Harris, “Fullerene-related structure of commercial glassy carbon”, *Philos. Mag.*, vol. 84, pp. 3159-3167 (2004).
- [33] L. Soukup, I. Gregora, L. Jastrabik, A. Konakova, “Raman spectra and electrical conductivity of glassy carbon”, *Mater. Sci. Eng. B.*, vol. 11, pp. 355-357 (1992).
- [34] K. Imoto, K. Takahashi, Y. Yamaguchi, T. Komura, J. Nakamura, and K. Murata, “High-performance carbon counter electrode for dye-sensitized solar cell”, *Sol. Energ. Mat. Sol. C.*, vol. 79, pp. 459-469 (2003).
- [35] C. L. Wang, and M. Madou, “From MEMS to NEMS with carbon”, *Biosens.*

- Bioelectron.*, vol. 20, pp. 2181-2187 (2005).
- [36] H. Tian, A. J. Bergren, and R. L. McCreery, “Ultraviolet visible spectroelectrochemistry of chemisorbed molecular layers on optically transparent carbon electrodes”, *Appl Spectrosc.*, vol. 61, pp. 1246-1252 (2007)
- [37] J. I. Heo, D. S. Shim, G. T. Teixidor, S. Oh, M. J. Madou, and H. Shin, “Carbon interdigitated array nanoelectrodes for electrochemical applications”, *J. Electrochem. Soc.*, vol. 158, pp. J76-J80 (2011).
- [38] A. Singh, J. Jayaram, M. Madou, and S. Akbar, “Pyrolysis of negative photoresists to fabricate carbon structures for microelectromechanical systems and electrochemical applications”, *J. Electrochem. Soc.*, vol. 149, pp. E78-E83 (2002).
- [39] J. A. Lee, S. W. Lee, K. Lee, S. I. Park, and S. S. Lee, “Fabrication and characterization of freestanding 3D carbon microstructures using multi-exposures and resist pyrolysis”, *J. Micromech. Microeng.*, vol. 18, 035012 (2008).
- [40] C. S. Sharma, H. Katepalli, A. Sharma, and M. Madou, “Fabrication and electrical conductivity of suspended carbon nanofiber arrays”, *Carbon*, vol. 49, pp. 1727-1732 (2011).
- [41] R. Du, S. Ssenyange, M. Aktary, and M. T. McDermott, “Fabrication and characterization of graphitic carbon nanostructures with controllable size, shape, and position”, *small*, vol. 5, pp. 1162-1168 (2009).
- [42] V. Penmatsa, H. Kowarada, and C. Wang, “Fabrication of carbon nanostructures using photo-nanoimprint lithography and pyrolysis”, *J. Micromech. Microeng.*, vol. 22, 045024 (2012).

- [43] K. Malladi, C. Wang, and M. Madou, "Fabrication of suspended carbon microstructures by e-beam writer and pyrolysis", *Carbon*, vol. 44, pp. 2602-2607 (2006).
- [44] Y. Lim, J. Heo, M. Madou and H. Shin, "Monolithic carbon structures including suspended single nanowires and nanomeshes as a sensor platform", *Nanoscale Res. Lett.*, vol. 8, 492 (2013).
- [45] L. H. Lee, "Mechanisms of thermal degradation of phenolic condensation polymer. II. Thermal stability and degradation schemes of epoxy resins", *J. Polym. Sci. Part A*, vol. 3, pp. 859-882 (1965).
- [46] A. Lyons, C. Wikins, and M. Robbins, "Thin pinhole-free carbon films", *Thin Solid Films*, vol. 103, pp. 333-341 (1983).
- [47] H. Nakagawa, and S. Tsuge, "Studies on thermal degradation of epoxy resins by high-resolution pyrolysis-gas chromatography", *J. Anal. Appl. Pyrolysis*, vol. 12, pp. 97-113 (1987).
- [48] K. S. Chen, and R. Z. Yeh, "Pyrolysis kinetics of epoxy resin in a nitrogen stmosphere", *J. Hazard. Mater.*, vol. 49, pp. 105-133 (1996).
- [49] C. Beyler, and M. Hirschler, "Thermal decomposition of polymers", *In SFPE Handbook of Fire Protection Engineering; National Fire Protection Association: Quincy*, pp. 110-131 (2002).
- [50] C. C. M. Ma, C. Y. Chen, H. C. Kuan, and W. C. Chang, "Processability, thermal, mechanical, and morphological properties of novolac type-epoxy resin-based carbon-carbon composite", *J. Compos. Mater.*, vol. 38, pp. 311-322 (2004).
- [51] B. Mehrotra, R. Bragg, and A. Rao, "Effect of heat treatment temperature (HTT) on

- density, weight and volume of glassy-like carbon (GC)", *J. Mater. Sci.*, vol. 18, pp. 2671-2678 (1983).
- [52] R. Martinez-Duarte, "SU-8 photolithography as a Toolbox for carbon MEMS", *Micromachines*, vol. 5, pp. 766-782 (2014).
- [53] B. Y. Park, L. Taherabadi, C. Wang, J. Zoval, and M. J. Madou, "Electrical properties and shrinkage of carbonized photoresist films and the implications for carbon microelectromechanical systems devices in conductive media", *J. Electrochem. Soc.*, vol. 152, pp. J136-J143 (2005).
- [54] D. B. Williams, and C. B. Carter, "Transmission electron microscopy: a textbook for materials science", 2<sup>nd</sup> ed.: *Springer* (2008).
- [55] Z. Wang, Z. Lu, Y. Huang, R. Xue, X. Huang, and L. Chen, "Characterizations of crystalline structure and electrical properties of pyrolyzed polyfurfuryl alcohol", *J. Appl. Phys.*, vol. 82, pp. 5705-5710 (1997).
- [56] P. Sundberg, R. Larsson, and B. Folkesson, "On the core electron binding energy of carbon and the effective charge of the carbon atom", *J. Electron. Spectrosc.*, vol. 46, pp. 19-29 (1988).
- [57] R. Martinez-Duarte, R. A. Gorkin, K. Abi-samra, and M. J. Madou, "The integration of 3D carbon-electrode dielectrophoresis on a CD-like centrifugal microfluidic platform", *Lab Chip*, vol. 10, pp. 1030-1043 (2010).
- [58] K. Kuriyama, and M. S. Dresselhaus, "An improved technique for determining hardness and elastic modulus using load and displacement sensing indentation experiments" *J. Mater. Res.*, vol. 7, pp. 940-945 (1992)



- [59] B. A. Samuel, R. Rajagopalan, H. C. Foley, and M. A. Haque, “Temperature effects on electrical transport in semiconducting nanoporous carbon nanowires”, *Nanotechnology*, vol. 19, 275702 (2008).
- [60] H. Gu, Z. Wang, and Y. Hu, “Hydrogen gas sensors based on semiconductor oxide nanostructures”, *Sensors*, vol. 12, pp. 5517-5550 (2012).
- [61] M. Lofdahl, M. Eriksson, M. Johansson, and I. Lundstrom, “Difference in hydrogen sensitivity between Pt and Pd field-effect devices”, *J. Appl. Phys.*, vol. 91, pp. 4275-4280 (2002).
- [62] K. J. Jeon, J. M. Lee, E. Lee, and W. Lee, “Individual Pd nanowire hydrogen sensors fabricated by electron-beam lithography”, *Nanotechnology*, vol. 20, pp. 1355021-1355025 (2009).
- [63] C. Perrotton, R. J. Westerwaal, N. Javahiraly, M. Slaman, H. Schreuders, B. Dam, and P. Meyrueis, “A reliable, sensitive and fast optical fiber hydrogen sensor based on surface plasmon resonance”, *Opt. Express*, vol. 21, pp. 382-390 (2013).
- [64] F. Favier, E. C. Walter, M. P. Zach, T. Benter, and R. M. Penner, “Hydrogen sensors and switches from electrodeposited palladium mesowire arrays”, *Science*, vol. 293, pp. 2227-2231 (2001).
- [65] H. H. Choi, J. Lee, K. Dong, B. Ju, and W. Lee, “Noxious gas detection using carbon nanotubes with Pd nanoparticles”, *Nanoscale Res. Lett.*, vol. 88, 605 (2011).
- [66] T. Zhang, S. Mubeen, E. Bekyarova, B. Y. Yoo, R. C. Haddon, N. V. Myung, and M. A. Deshusses, “Poly(m-aminobenzene sulfonic acid) functionalized single-walled carbon nanotubes based gas sensor”, *Nanotechnology*, vol. 18, 165504 (2007).

- [67] K.T. Kim, S.J. Sim, and S.M. Cho, "Hydrogen gas sensor using Pd nanowires electro-deposited into anodized alumina template", *IEEE Sens. J.*, vol. 6, pp. 509-513 (2006).
- [68] D. Yang, L. Valentin, J. Carpena, W. Otano, O. Resto, and L. F. Fonseca, "Temperature-activated reverse sensing behavior of Pd nanowire hydrogen sensors", *Small*, vol. 9, pp. 188-192 (2013).
- [69] D. Yang, J. Carpena-Nunez, L.F. Fonseca, A. Biaggi-Labiosa, and G.W. Hunter, "Shape-controlled synthesis of palladium and copper superlattice nanowires for high-stability hydrogen sensors", *Sci. Rep.*, vol. 4, pp. 1-5 (2014).
- [70] F. Favier, E.C. Walter, M.P. Zach, T. Benter, and R.M. Penner, "Hydrogen sensors and switches from electrodeposited palladium mesowire arrays", *Science*, vol. 293 pp. 2227-2231 (2001).
- [71] F. Yang, D.K. Taggart, and R.M. Penner, "Fast, sensitive hydrogen gas detection using single palladium nanowires that resist fracture", *Nano Lett.*, vol. 9, pp. 2177-2182 (2009).
- [72] F. Yang, S.-C. Kung, M. Cheng, J.C. Hemminger, and R.M. Penner, "Smaller is faster and more sensitive: the effect of wire size on the detection of hydrogen by single palladium nanowires", *ACS Nano*, vol. 4, pp. 5233-5244 (2010).
- [73] H. Yushi, D. Perello, U. Mushtaq, and Y. Minhee, "A single palladium nanowire via electrophoresis deposition used as an ultrasensitive hydrogen sensor", *IEEE T. Nanotechnol.*, vol. 7, pp. 693-699 (2008).
- [74] T. Kiefer, F. Favier, O. Vazquez-Mena, G. Villanueva, and J. Brugger, "A single nanotrench in a palladium microwire for hydrogen detection", *Nanotechnology*, vol. 19, 125502 (2008).

- [75] K. R. Kim, J. Noh, J. M. Lee, Y. J Kim, and W. Lee, “Suppression of phase transitions in Pd thin films by insertion of a Ti buffer layer”, *J. Mater. Sci.*, vol. 46, pp.1597-1601 (2011).
- [76] E. Lee, J. M. Lee, E. Lee, J. Noh, J. H. Joe, B. Jung, and W. Lee, “Hydrogen gas sensing performance of Pd-Ni alloy thin films”, *Thin Solid Films*, vol. 519, pp.880-884 (2011).
- [77] X. Q. Zeng, M. L. Latimer, Z. L. Xiao, S. Panuganti, U. Welp, W. K. Kwok, and T. Xu, “Hydrogen gas sensing with networks of ultrasmall palladium nanowires formed on filtration membrane”, *Nano. Lett.*, vol. 11, pp. 262-268 (2011).
- [78] P. Mirtaheri, T. Omtveit, T. Klotzbuecher, S. Grimnes, O. G. Martinsen, and T. I. Tonnessen, “Miniaturization of a biomedical gas sensor”, *Physiol. Meas.*, vol. 25, pp. 1511-1522 (2004).
- [79] N. Funazaki, A. Hemmi, S. Ito, Y. Asano, Y. Yano, N. Miura, and N. Yamazoe, “Application of semiconductor gas sensor to quality control of meat freshness in food industry”, *Sens. Actuators B-Chem.*, vol. 24-25, pp. 797-800 (1995).
- [80] J. W. Gradner, G. Wei, T. Vincent, K. Volans, P. Tremlett, T. Wotherspoon, and D. C. Dyer, “A gas sensor system for harsh environment applications”, *Procedia Eng.*, vol. 120, pp. 275-278 (2015).
- [81] G. F. Fine, L. M. Cavanagh, A. Afonja, and R. Binions, “Metal oxide semi-conductor gas sensors in environmental monitoring”, *Sensors*, vol. 10, pp. 5469-5502 (2010).
- [82] G. Muller, A. Hackner, S. Beer, and J. Gobel, “Solid-state gas sensors: sensor system challenges in the civil security domain”, *Materials*, vol. 9, 65 (2016).
- [83] A. Ponzoni, D. Zappa, E. Comini, V. Sberveglieri, G. Fablia, and G. Sberveglieri,

- “Metal oxide nanowire gas sensors: application of conductometric and surface ionization architectures”, *Chem. Eng. Trans.*, vol. 30, pp. 31-36 (2012).
- [84] M. Leidinger, T. Sauerwald, W. Reimringer, G. Ventura, and A. Schutze, “Selective detection of hazardous VOCs for indoor air quality applications using a virtual gas sensor array”, *J. Sens. Sens. Syst.*, vol. 3, pp.253-263 (2014).
- [85] S. Some, Y. Xu, Y. Kim, Y. Yoon, H. Qin, A. Kulkarni, T. Kim, and H. Lee, “Highly sensitive and selective gas sensor using hydrophilic and hydrophobic graphenes”, *Sci. Rep.*, vol. 3, 1868 (2013).
- [86] I. Elmi, S. Zampolli, E. Cozzani, F. Mancarella, and G. C. Cardinali, “Development of ultra-low-power consumption MOX sensors with ppb-level VOC detection capabilities for emerging applications”, *Sens. Actuator B-Chem.*, vol. 135, pp. 342-351 (2008).
- [87] Y. Guo, X-Zhang, and G. Han, “Investigation of structure and properties of N-doped TiO<sub>2</sub> thin films grown by APCVD”, *Mater. Sci. Eng. B.*, vol. 135, pp. 83-87 (2006).
- [88] W. W. Nazaroff, and C. J. Weschler, “Cleaning products and air fresheners: exposure to primary and secondary air pollutants”, *Atmos. Environ.*, vol. 38, pp. 2841-2865 (2004).
- [89] X. Chen, M. Cao, Y. Hao, Y. Li, and P. Wang, “A non-invasive detection of lung cancer combined virtual gas sensors array with imaging recognition technique”, *Conf. IEEE Eng. Med. Biol. Soc.*, vol. 6, pp. 5873-5876 (2005).
- [90] Y. Takada, R. Otsuka, and K. Tsukada, “A carbon monoxide sensing film based on hemoglobin allostery”, *J. Biomed., Sci. Eng.*, vol. 7, pp. 173-180 (2014).
- [91] H. Lim, M. Jang, and K. S. Suslick, “Preoxidation for colorimetric sensor array detection of VOCs”, *J. Am. Chem. Soc.*, vol. 133, pp. 16786-16789 (2011).

- [92] N. G. Mphythi, A. S. Adekunle, and E. E. Ebenso, “Electrocatalytic oxidation of epinephrine and norepinephrine at metal oxide doped phthalocyanine/MWCNT composite sensor”, *Sci. Rep.*, vol. 6, 26938 (2016).
- [93] M. Righettoni, A. Amann, and S. E. Pratsinis, “Breath analysis by nanostructured metal oxides as chemo-resistive gas sensors”, *Mater. Today*, vol. 18, pp. 163-171(2015).
- [94] S. Sharma, and M. Madou, “A new approach to gas sensing with nanotechnology”, *Phil. Trans. R. Soc. A*, vol. 370, pp. 2448-2473 (2011).
- [95] X. Chen, C. K. Y. Wong, C. A. Yuan, and G. Zhang, “Nanowire-based gas sensors”, *Sens. Actuator B-Chem.*, vol. 177, pp. 178-195 (2013).
- [96] F. Huber, S. Riegert, M. Madel, and K. Thonke, “H<sub>2</sub>S sensing in the ppb regime with zinc oxide nanowires”, *Sens. Actuator B-Chem.*, vol. 239, pp. 358-363 (2017).
- [97] N. Tiwale, “Zinc oxide nanowire gas sensors: fabrication, functionalization and devices”, *Mater. Sci. Technol.*, vol. 31, pp. 1681-1697 (2015).
- [98] S. Patel, H. Park, P. Bonato, L. Chan, and M. Rodgers, “A review of wearable sensors and systems with application in rehabilitation”, *J. Neuroeng. Rehabil.*, vol. 9, 21 (2012).
- [99] H. Kim, and J. Lee, “Highly sensitive and selective gas sensors using p-type oxide semiconductors: Overview”, *Sens. Actuator B-Chem.*, vol. 192, pp. 607-627 (2014).
- [100] S. M. Kanan, O. M. El-Kadri, I. A. Abu-Yousef, and M. C. Kanan, “Semiconducting metal oxide based sensors for selective gas pollutant detection”, vol. 9, pp. 8158-8196 (2009).
- [101] T. Becker, S. Muhlberger, C. B. Braunmuhl, G. Muller, T. Ziemann, and K. V. Hechtenberg, “Air pollution monitoring using tin-oxide-based microreactor systems”,

- Sens. Actuator B-Chem.*, vol. 69, pp. 108-119 (2000).
- [102] C. Liu, C. Chen, and J. Leu, “Fabrication and CO sensing properties of mesostructured ZnO gas sensors”, *J. Electrochem. Soc.*, vol. 156, pp. J16-J19 (2009).
- [103] S. Peng, G. Wu, W. Song, and Q. Wang, “Application of flower-like ZnO nanorods gas sensor detecting SF<sub>6</sub> decomposition products”, *J. Nanomater.*, vol. 2013, pp. 1-7 (2013).
- [104] R. M. Penner, “Chemical sensing with nanowires”, *Annu. Rev. Anal. Chem.*, vol. 5, pp. 461-485 (2012).
- [105] J. Yun, C. Y. Jin, J. Ahn, S. Jeon, and I. Park, “A self-heated silicon nanowire array: selective surface modification with catalytic nanoparticles by nanoscale joule heating and its gas sensing applications”, *Nanoscale*, vol. 5, pp. 6851-6856 (2013).
- [106] Z. Dai, L. Xu, G. Duan, T. Li, H. Zhang, Y. Li, Y. Wang, Y. Wang, and W. Cai, “Fast-response, sensitive and low-powered chemosensors by fusing nanostructured porous thin film and IDEs-microheater chip”, *Sci. Rep.*, vol. 3, 1669 (2013).
- [107] L. Xu, Z. Dai, G. Duan, L. Guo, Y. Wang, H. Zhou, Y. Liu, W. Cai, Y. Yang, and T. Li, “Micro/nano gas sensors: a new strategy towards in-situ wafer-level fabrication of high performance gas sensing chips”, *Sci. Rep.*, vol. 5, 10507 (2015).
- [108] Y. Liu, J. Parisi, X. Sun, and Y. Lei, “Solid-state gas sensors for high temperature applications – a review”, *J. Mater. Chem. A*, vol. 2, pp. 9919-9943 (2014).
- [109] G. Meng, F. Zhuge, K. Nagashima, A. Nakao, M. Kanai, Y. He, M. Boudot, T. Takahashi, K. Uchida, and T. Yanagida, “Nanoscale thermal management of single SnO<sub>2</sub> nanowire: pico-joule energy consumed molecule sensor”, *ACS Sens.*, vol. 1, pp. 997-

- 1002 (2016).
- [110] P. Wang, S. Chem, C. Su, and Y. Liao, “Direct printed silver nanowire thin film patterns for flexible transparent heaters with temperature gradients”, *RSC Adv.*, vol. 5, pp. 98412-98418 (2015).
- [111] Y. H. Kim, S. J. Kim, Y. Kim, Y. Shim, S. Y. Kim, B. H. Hong, and H. W. Jang, “Self-activated transparent all-graphene gas sensor with endurance to humidity and mechanical bending”, *ACS Nano*, vol. 9, pp. 10453-10460 (2015).
- [112] S. Steinhauer, E. Brunet, T. Maier, G. C. Mutinati, and O. Freudenberg, “Single suspended CuO nanowire for conductometric gas sensing”, *Proc. Eng.*, vol. 47, pp. 17-20 (2012).
- [113] Y. J. Choi, I. S Hwang, K. J. Choi, J. H. Park, and J. H. Lee, “Novel fabrication of an SnO<sub>2</sub> nanowire gas sensor with high sensitivity”, *Nanotechnology*, vol. 19, 095508 (2008).
- [114] M. R. Alenezi, S. J. Henley, N. G. Emerson and S. R. P. Silva, “From 1D and 2D ZnO nanostructures to 3D hierarchical structures with enhanced gas sensing properties”, *Nanoscale*, vol. 6, pp. 235-247 (2014).
- [115] O. Lupan, V. V. Ursaki, G. Chai, L. Chow, G. A. Emelchenko, I. M. Tiginyanu, A. N. Gruzintsev, and A. N. Redkin, “Selective hydrogen gas nanosensor using individual ZnO nanowire with fast response at room temperature”, *Sens. Actuator B-Chem.*, vol. 144, pp. 56-66 (2010).
- [116] W. Tian, Y. Ho, C. Chen, and C. Kuo, “Sensing performance of precisely ordered TiO<sub>2</sub> nanowire gas sensors fabricated by electron-beam lithography”, *Sensors*, vol. 13, pp. 865-874 (2013).

- [117] S. K. Youn, N. Ramgir, C. Wang, K. Subannajui, V. Cimalla, and M. Zacharias, “Catalyst-free growth of ZnO nanowires based on topographical confinement and preferential chemisorption and their use for room temperature CO detection”, *J. Phys. Chem. C*, vol. 114, pp. 10092-10100 (2010).
- [118] Y. Lim, J. Heo, and H. Shin, “Fabrication and application of a stacked carbon electrode set including a suspended mesh made of nanowires and a substrate-bound planar electrode toward for an electrochemical/biosensor platform”, *Sens. Actuator B-Chem.*, vol. 192, pp. 796-803 (2014).
- [119] H. F. McMurdie, M. C. Morris, E. H. Evan, B. Paretzkin, W. Wong-Ng, and C. R. Hubbard, “Standard x-ray diffraction powder patterns from the JCPDS research associatedship”, *Powder Differ.*, vol. 1, pp. 265-275 (1986).
- [120] R. A. Laudise, A. A. Ballman, “Hydrothermal synthesis of zinc oxide and zinc sulfide”, *J. Phys. Chem.*, vol. 64, pp. 688-691 (1960).
- [121] R. Parize, J. Garnier, O. Chaix-Pluchery, C. Verrier, E. Appert, V. Consonni, “Effects of hexamethylenetetramine on the nucleation and radial growth of ZnO nanowires by chemical bath deposition”, *J. Phys. Chem. C*, vol. 120, pp. 5242-5250 (2016).
- [122] V. Strano, R. G. Urso, M. Scuderi, K. O. Iwe, F. Simone, E. Ciliberto, C. Spinella, S. Mirabella, “Double role of HMTA in ZnO nanorods grown by chemical bath deposition”, *J. Phys. Chem. C*, vol. 118, pp. 28189-28195 (2014).
- [123] M. C. Akgun, Y. E. Kalay, H. E. Unalan, “Hydrothermal zinc oxide nanowire growth using zinc acetate dehydrate salt”, *J. Mater. Res.*, vol. 27, pp. 1445-1451 (2012).
- [124] Q. Ahsanulhaq, A. Umar, Y. B. Hahn, “Growth of aligned ZnO nanorods and nanopencils on ZnO/Si in aqueous solution: growth mechanism and structural and optical



- properties”, *Nanotechnology*, vol. 18, 115603 (2007).
- [125] S. Ozturk, N. Kilinc, N. Tasaltin, Z. Z. Ozturk, “Fabrication of ZnO nanowires and nanorods”, *Physica E*, vol. 44, pp. 1062-1065 (2012).
- [126] P. Yang, H. Yan, S. Mao, R. Russo, J. Johnson, R. Saykally, N. Morris, J. Pham, R. He, and H Choi, “Controlled growth of ZnO nanowires and their optical properties”, *Adv. Func. Mater.*, vol. 12, pp. 323-331 (2002).
- [127] L. S. Wang, and X. Z. Wang, “Synthesis of well-aligned ZnO nanowires by simple physical vapor deposition on c-oriented ZnO thin films without catalysts or additives”, *Appl. Phys. Lett.*, vol. 86, 024108 (2005).
- [128] L. C. Campos, S. H. Dalal, D. L. Baptista, R. Magalhaes-Paniago, A. S. Ferlauto, W. I. Milne, L. O. Ladeira, and R. G. Lacerda, “Determination of the epitaxial growth of zinc oxide nanowires on sapphire by grazing incidence synchrotron x-ray diffraction”, *Appl. Phys. Lett.*, vol. 90, 181929 (2007).
- [129] Y. Lim, Y. Lee, J. Heo, and H. Shin, “Highly sensitive hydrogen gas sensor based on a suspended palladium/carbon nanowire fabricated via batch microfabricated processes”, *Sens. Actuator B-Chem.*, vol. 210, pp. 218-224 (2015).
- [130] C. Kilic, and A. Zunger, “Origins of coexistence of conductivity and transparency in  $\text{SnO}_2$ ”, *Phys. Rev. Lett.*, vol. 88, 095501 (2002).
- [131] K. Galatsis, L. Cukrow, W. Wlodarski, P. McCormick, K. Kalanter-zadeh, E. Comini, and G. Sberveglieri, “p- and n-type Fe-doped  $\text{SnO}_2$  gas sensors fabricated by the mechanochemical processing technique”, *Sens. Actuator B-Chem.*, vol. 93, pp. 562-565 (2003).

- [132] N. Han, L. Chai, Q. Wang, Y. Tian, P. Deng, and Y. Chen, “Evaluating the doping effect of Fe, Ti and Sn on gas sensing property of ZnO”, *Sens. Actuator B-Chem.*, vol. 147, pp. 525-530 (2010).
- [133] C. O. Park, and S. A. Akbar, “Ceramics for chemical sensing”, *J. Mater. Sci.*, vol. 38, pp. 4611-4637 (2003).
- [134] N. Barsan, and U. Weimer, “Conduction model of metal oxide gas sensors”, *J. Electroceram.*, vol. 7, pp. 143-167 (2001).
- [135] J. Burgues, S. Marco, “Low power operation of temperature-modulated metal oxide semiconductor gas sensor”, *Sensors*, vol. 18, pp.339 (2018).
- [136] A. A. Firooz, A. R. Mahjoub, and A. A. Khodadadi, “Highly sensitive CO and ethanol nanoflower-like SnO<sub>2</sub> sensor among various morphologies obtained by using single and mixed ionic surfactant templates”, *Sens. Actuators B-Chem.*, vol. 141, pp. 89–96 (2009).
- [137] N. Singh, A. Ponzoni, R. K. Gupta, P. S. Lee, and E. Comini, “Synthesis of In<sub>2</sub>O<sub>3</sub>–ZnO core–shell nanowires and their application in gas sensing”, *Sens. Actuators B-Chem.*, vol. 160, pp. 1346–1351 (2011).
- [138] L. Xu, R. Xing, J. Song, W. Xu, and H. Song, “ZnO–SnO<sub>2</sub> nanotubes surface engineered by Ag nanoparticles: synthesis, characterization, and highly enhanced HCHO gas sensing properties”, *J. Mater. Chem. C*, vol. 1, pp. 2174–2182 (2013).
- [139] Y. Zeng, K. Zhang, X. Wang, Y. Sui, B. Zou, W. Zheng, and G. Zou, “Rapid and selective H<sub>2</sub>S detection of hierarchical ZnSnO<sub>3</sub> nanocages”, *Sens. Actuators B-Chem.*, vol. 159, pp. 245–250 (2011).

- [140] X. Pan, X. Zhao, J. Chen, A. Bermak, and Z. Fan, “A fast-response/recovery ZnO hierarchical nanostructure based gas sensor with ultra-high room-temperature output response”, *Sens. Actuator B-Chem.*, vol. 206, pp. 764-771 (2015).
- [141] F. Wang, H. Li, Z. Yuan, Y. Sun, F. Chang, H. Deng, L. Xie, and H. Li, “A highly sensitive gas sensor based on CuO nanoparticles synthesized via sol-gel method”, *RSC Adv.*, vol. 6, pp. 79343-79349 (2016).
- [142] J. Yun, C. Y. Jin, J. Ahn, S. Jeon, and I. Park, “A self-heated silicon nanowire array: selective surface modification with catalytic nanoparticles by nanoscale Joule heating and its gas sensing applications”, *Nanoscale*, vol. 5, pp. 6851-6856 (2013).
- [143] Z. Dai, L. Xu, G. Duan, T. Li, H. Zhang, Y. Li, Y. Wang, Y. Wang, and W. Cai, “Fast-response, sensitive and low-powered chemosensors by fusing nanostructured porous thin film and IDEs-microheater chip”, *Sci. Rep.*, vol. 3, 1669 (2013).
- [144] B. Bierer, J. Kneer, J. Wollenstein, and S. Palzer, “MEMS based metal oxide sensor for simultaneous measurement of gas induced changes of the heating power and the sensing resistance”, *Microsyst. Technol.*, vol. 22, pp. 1855-1863 (2016).
- [145] G. Meng, F. Zhuge, K. Nagashima, A. Nakao, M. Kanai, Y. He, M. Boudot, T. Takahashi, K. Uchida, and T. Yanagida, “Nanoscale thermal management of single SnO<sub>2</sub> nanowire: pico-joule energy consumed molecule sensor”, *ACS Sensors*, vol. 1, pp. 997-1002 (2016).
- [146] D. Briand, S. Colin, J. Courbat, S. Raible, J. Kappler, N. F. De Rooij, “Integration of MOX gas sensors on polyimide hotplate”, *Sens. Actuators B-Chem.*, vol. 130, pp. 430-435 (2008).
- [147] J. Courbat, D. Briand, Y. Yue, S. Raible, N. F. De Rooij, “Multi sensor platform on

- plastic foil for environmental monitoring”, *Procedia Chem.*, vol. 1, pp. 597-600 (2009)
- [148] S. E. Moon, H. –K. N. –J. Choi, J. Lee, W. S. Yang, J. Kim, J. J. Jong, D. –J. Yoo, “Low-power-consumption metal oxide NO<sub>2</sub> gas sensor based on micro-heater and screen printing technology”, *J. Nanosci. Nanotechnol.*, vol. 12, pp. 5543-5546 (2012).
- [149] S. E. Moon, J. –W. Lee, N. –J. Choi, H. –K. Lee, W. S. Yang, J. Kim, “High-response and low-power-consumption CO micro gas sensor based on nano-powders and a micro-heater”, *J. Korean Phys. Soc.*, vol. 60, 99. 235-239 (2012).
- [150] J. Courbat, D. Briand, Y. Yue, S. Raible, N. F. De Rooij, “Drop-coated metal-oxide gas sensor on polyimide foil with reduced power consumption for wireless applications”, *Sens. Actuator B-Chem.*, vol. 161, pp. 862-868 (2012).
- [151] A. Oprea, J. Courbat, D. Briand, N. Barsan, U. Weimar, N. F. De. Rooij, “Environmental monitoring with a multi sensor platform on polyimide foil”, *Sens. Actuator B-Chem.*, vol. 171-172, pp. 190-197 (2012).
- [152] S. Benedict, P. K. Basu, N. Bhat, “Low power gas sensor array on flexible acetate substrate”, *J. Micromech. Microeng.*, vol. 27, 75024 (2017).
- [153] T. Maitra, S. Sharma, A. Srivastava, Y. Cho, M. Madou, and A. Sharma, “Improved graphitization and electrical conductivity of suspended carbon nanofibers derived from carbon nanotube/polyacrylonitrile composites by directed electrospinning”, *Carbon*, vol. 50, pp. 1753-1761 (2012).
- [154] Y. Lim, J. H. Chu, D. H. Lee, S. Kwon, and H. Shin, “Increase in graphitization and electrical conductivity of glassy carbon nanowires by rapid thermal annealing”, *J. Alloys Compd.*, vol. 702, pp. 465-471 (2017).

- [155] A. P. Graham, G. Schindler, G. S. Duesberg, T. Lutz, W. Weber, “An investigation of the electrical properties of pyrolytic carbon in reduced dimensions: Vias and wires”, *J. Appl. Phys.*, vol. 107, 114316 (2010).
- [156] L. Mele, B. Morana, C. de Boer, J. F. Creemer, and P. M. Sarro, “Low-temperature wafer-level packaging of a MEMS microreactor with a lateral feed through by local PECVD TEOS deposition”, *Procedia Chem.*, vol. 1, pp. 1531-1534 (2009).
- [157] Y. Koda, H. Sugita, T. Suwa, R. Kuroda, T. Goto, A. Teramoto, and S. Suguwa, “Low leakage current Al<sub>2</sub>O<sub>3</sub> metal-insulator-metal capacitors formed by atomic layer deposition at optimized process temperature and O<sub>2</sub> post deposition annealing”, *ECS Trans.*, vol. 72, pp. 91-100 (2016).
- [158] S. -W. Jeong, H. J. Lee, K. S. Kim, M. T. You, Y. Roh, T. Noguchi, W. Xianyu, and J. Jung, “HfO<sub>2</sub> gate insulator formed by atomic layer deposition for thin-film-transistors”, *Thin Solid Films*, vol. 515, pp. 5109-5112 (2007).
- [159] P. Jancovic, B. Hudec, E. Dobrocka, J. Derer, J. Fedor, and K. Frohlich, “Resistive switching in HfO<sub>2</sub>-based atomic layer deposition grown metal-insulator-metal structures”, *Appl. Surf. Sci.*, vol. 312, pp. 112-116 (2014).
- [160] S. Baruah, C. Thanachayanont, and J. Dutta, “Growth of ZnO nanowires on nonwoven polyethylene fibers”, *Sci. Technol. Adv. Mater.*, vol. 99, pp. 025009-8 (2008).
- [161] N. Ramgir, N. Datta, M. Kaur, S. Kailasaganapathit, A. K. Debnath, D. K. Aswal, and S. G. Gupta, “Metal oxide nanowires for chemiresistive gas sensor: Issues, challenges and prospects”, *Colloid Surf. A-Physicochem. Eng. Asp.*, Vol. 439, pp. 101-116 (2013).
- [162] A. Z. Sadek, S. Choopun, W. Wlodarski, S. J. Ippolite, and K. Kalantar-zadeh,

- “Characterization of ZnO nanobelt-based gas sensor for H<sub>2</sub>, NO<sub>2</sub>, and hydrocarbon sensing”, *IEEE Sens. J.*, vol. 7, pp. 919-924 (2007).
- [163] Y. Lim, S. Kim, Y. M. Kwon, J. M. Baik, H. Shin, “A highly sensitive gas-sensing platform based on a metal-oxide nanowire forest grown on a suspended carbon nanowire fabricated at a wafer level”, *Sens. Actuator B-Chem.*, Vol. 260, pp. 55-62 (2018).
- [164] S. Hasegawa, I. Shiraki, F. Tanabe, R. Hobara, T. Kanagawa, T. Tanikawa, I. Matsuda, C. L. Petersen, T. M. Hanse, P. Boggild, and F. Grey, “Electrical conduction through surface super structures measured by microscopic four-point probe”, *Surf. Rev. Lett.*, vol. 10, pp. 963-980 (2013).
- [165] X. Li, W. Cai, J. An, S. Kim, J. Nah, D. Yang, R. Piner, A. Velamakanni, I. Jung, E. Tutuc, S. K. Benerjee, L. Colombo, R. S. Ruoff, “Large-area synthesis of high-quality and uniform graphene films on copper foils”, *Science*, vol. 324, pp. 1312-1314 (2009).
- [166] L. Meng, Z. Wang, J. Jiang, Y. Yang, J. Wang, “Defect healing of chemical vapor deposition graphene growth by metal substrate step”, *J. Phys. Chem. C*, vol. 117, pp. 15260-15265 (2013).
- [167] C. Gong, M. Acik, R. M. Abolfath, Y. Chabal, K. Cho, “Graphitization of graphene oxide with ethanol during thermal reduction”, *J. Phys. Chem. C*, Vol. 116, pp. 9969-9979 (2012).
- [168] J. Yun, C. Y. Jin, J. Ahn, S. Jeon, and I. Park, “A self-heated silicon nanowire array: selective surface modification with catalytic nanoparticles by nanoscale Joule heating and its gas sensing applications”, *Nanoscale*, vol. 5, pp. 6851-6856 (2013).
- [169] O. J. A. Schueller, S. T. Brittain, C. Marzolin, and G. M. Whitesides, “Fabrication and characterization of glassy carbon MEMS”, *Chem. Mater.*, vol. 9, pp. 1399-1406

- (1997).
- [170] M. A. Panzer, M. Shandalov, J. A. Rowlette, Y. Oshima, Y. W. Chen, P. C. McIntyre, and K. E. Goodson, “Thermal properties of ultrathin hafnium oxide gate dielectric films”, *IEEE Electron Device Lett.*, vol. 30, pp. 1269-1271 (2009).
- [171] S. Samal, J. Lee, D. Jeong, and H. Kim, “Characterization of thermal conductivity of SiO<sub>2</sub>-Al<sub>2</sub>O<sub>3</sub>-Y<sub>2</sub>O<sub>3</sub> glasses”, *Thermochim. Acta*, vol. 604, pp. 1-6 (2015).
- [172] R. A. Potyrallo, “Multivariable sensors for ubiquitous monitoring of gases in the era of internet of things and industrial internet”, *Chem. Rev.*, vol. 116, pp. 11877-11923 (2016).
- [173] E. Traversa, “Ceramic sensors for humidity detection: the state-of-the-art and future developments”, *Sens. Actuators B-Chem.*, vol. 23, pp. 135-156 (1995).
- [174] E. McCafferty, and A. C. Zettlemyer, “Adsorption of water vapour on  $\alpha$ -Fe<sub>2</sub>O<sub>3</sub>”, *Discuss Faraday Soc.*, vol. 52, pp. 239-254 (1971).
- [175] A. Tischner, T. Maier, C. Stepper, A. Kock, “Ultrathin SnO<sub>2</sub> gas sensors fabricated by spray pyrolysis for the detection of humidity and carbon monoxide”, *Sens. Actuator B-Chem.*, vol. 134, pp. 796-802 (2008).

## ACKNOWLEDGEMENTS

First of all, I thank my advisor. My advisor gave me the first hand when I was in trouble. I made each angular stone with a strong personality like me and made it into jewels like now. I spent seven years in the lab building the best laboratory I've ever had with my advisor. I apologize for not being able to convey my gratitude directly to my thesis. I am forever in debt to him.

I should expand my thanks to all committee members (Prof. Juyong Kim, Prof. Soon-Yong Kwon, Prof. Jeong Min Baik, Prof. Kyoung-Jin Choi and, Jongbaeg Kim) for their generous and scrupulous advices on this dissertation. Thanks again for their valuable time and comments. I want to thank Prof. Juyoung Kim, Prof. Soon-Yong Kwon, Prof. Jeong Min Baik, and Prof. Sang Hoon Joo for their good experimental results about the suspended 1D metal oxide nanostructure-based gas sensor. Prof. Juyoung Kim helped me study the mechanical characteristics of the glassy carbon structure. Prof. Soon-Yong Kwon has made it easy to understand how to improve the electrical characteristics of the glassy carbon structure and the improved principle of the graphene healing mechanism. Prof. Jeong Min Baik pointed out how to selectively grow multiple metal oxide nanowires, so that he was able to produce the first suspended structure type-based gas sensor. Finally, Prof. Sang Hoon Joo helped me to analyze nanoporous carbon structures, and many ideas developed because I showed how to do research. I am grateful to all the professors who have helped me once again.

My special thanks to go former and current MNIS laboratory members who became like family over the past seven years. I shared many precious memories with lab members (Jeong-il Heo, Yunjeong Lee, Jongmin Lee, Junyeong Seo, Jisoo Hong, Soosung Kim, Beomsang Kim, Seungwook Lee, Taejung Kim and Sanghee Jung). Thank you for your help and your encouragement to keep me from giving up.



I thanks to Dongkyu Park, Yeong Min Kwon, Yongmin Kim, and Jin-hoe Hur. Dongkyu Park has always helped the MEMS process, the best senior who has always solve the problem. Yeong Min Kwon helped me to develop a gas sensor and I am always grateful for being like my brother. Yongmin Kim is the best senior in life and has always solved electrical problems. Finally, Jin-Hoe Hur is the best mentor I ever had in UNST. He always encouraged me.

I am thankful to the people in administration office for always kindly helping me: Hyemi Kwak, Nahee Nam, Sohee Park, Kyoung-Young Lim, So Hee Eom, Jiyeon Kim, Byeongjin Gil, and Jongmin Jeong. I also want to thank the member of UNIST Central Research Facilities for the support of fabrication and analysis: Min-Jae Kim, Hyung-il Kim, Lu-da Lee, Hae-ra Kang, Kang-O Kim, Young-ki Kim, Dong-ju Lim, Ji-hye Park, Gyeong-Ae Lee, Sun-yi Lee, Yeong-bi Kang. In addition, I am thankful to support about the processing system: Daemyoung Enterprise Co., Ltd, NEXTRON Co., Ltd, Daejin Tech.

Thank you my friend Jeongwoo Kwon, Beongju Ryu, Jayoung Park, Jiwook Jang, Kangjae Jung, and Jinyong Cha.

Finally, I am grateful to Ji-in Lee, a wonderful future wife who will devote this and my life. The destiny we are connected is the greatest gift I could imagine.

Thanks to my family, I am now, and I have been able to concentration on my doctoral program. I am infinitely grateful to my father Mindong Lim and my mother Mijeong Kim. Especially, I thank to Sungjin Lim, my best friend and wonderful brother. I am sorry to pass on my thesis, and I am always grateful for your truest in me.

## Curriculum Vitae

**Yeongjin Lim, Ph. D.**

School of Materials Science and Engineering

Ulsan National Institute of Science and Technology (UNIST)

709, EB 5, 50 UNIST-gil, Ulsan, 44919, Republic of Korea

E-mail : [khai0922@gmail.com](mailto:khai0922@gmail.com)

Lab homepage : <http://mnis.unist.ac.kr>

### **EDUCATION**

- 2011.09 ~ 2018.08**      **Ulsan National Institute of Science and Technology**  
Combined M.S. & Ph. D. in Materials Engineering  
Advisor : Prof. Heungjoo Shin ([hjshin@unist.ac.kr](mailto:hjshin@unist.ac.kr))  
Dissertation : Suspended 1D metal oxide nanostructure-based gas sensor
- 2009.03 ~ 2010.08**      **Gyeongsang National University**  
M.S. in Materials Engineering  
Advisor : Prof. Cheol Jin Kim ([cjk@gnu.ac.kr](mailto:cjk@gnu.ac.kr))
- 2005.03 ~ 2009.02**      **Gyeongsang National University**  
B.S. in Materials Engineering

## RESEARCH EXPERIENCE

**2015.08 ~ Present**      Development of suspended heterogeneous nanostructure-based hazardous gas microsensor system  
*Ministry of Trade, Industry and Energy*

Development of ultra-small/high sensitivity/high reliability/low power combined gas sensor and system technology based on the type of public part capable of real-time monitoring of 9 kinds of harmful gases (NO<sub>2</sub>, SO<sub>2</sub>, CO, CH<sub>4</sub>, H<sub>2</sub>, VOCs).

Suspended 1D nanostructure-based gas sensor array platform

Gas sensing materials : ZnO, CuO

Power consumption : ~ 1mW

Sensitivity (ppm) : 124.5 (CH<sub>4</sub>), 0.85 (CO), 0.74 (H<sub>2</sub>), 0.079 (NO<sub>2</sub>), 0.91 (SO<sub>2</sub>).

**2015.03 ~ Present**      Development of advanced mechanical systems for monitoring and handling chemical/biological disasters  
*Ulsan National Institute of Science and Technology*

Development of unmanned equipment and technology for biochemical disaster monitoring to prevent prejudice against biochemical disasters and limited biochemical disasters.

Development of multiple metal oxide nanowire-based gas sensor fabricated at the wafer level

Gas sensing materials : Pd nanoparticle, CuO, ZnO, TiO<sub>2</sub>

Wafer level microfabrication process : Carbon-MEMS, Hydrothermal method

Sensitivity (ppm) : 244.9 (CH<sub>4</sub>), 2.35 (CO), 15.4 (H<sub>2</sub>), 1.26 (NO<sub>2</sub>), 2.17 (SO<sub>2</sub>).

**2013.03 ~ 2014.10**      Development of composite sensor and signal processing technology based on layered nanostructure  
*Ministry of Science, Ulsan Science and Technology Promotion Center*

Development of semiconducting signal processing designing technology and system capable of simultaneously processing multiple signal and multiple sensor based on carbon nanowire with a hierarchical structure that can be miniaturized and portable device.

Study of electrical and thermal characteristics of fabricated nanowire and temperature sensing

**2013.01 ~ 2014.01**      Development of gas sensor based on suspended hybrid nanowires

SK Innovation Co., Ltd.

Development of functional nanowire grown on the surface of carbon nanowire for use as a nanowire-based gas sensor that can be miniaturized and portable with simple detection methods and structures.

Development of hybrid ZnO/carbon nanowire fabrication technique at the wafer level

Verification of chemoresistive type gas sensor

Wafer level microfabrication process : Carbon-MEMS

Limit of detection of the Hydrogen gas : 1 ppm

**2012.01 ~ 2014.01**      Development of suspended monolithic carbon nanowire based bio/gas sensor

SK Innovation Co., Ltd.

Development of monolithic carbon nanowire structure fabrication and application which can drastically improve yield and design limit problem of existing public type nanowire-based bio/gas sensor

Development of carbon nanowire array for use as the hydrogen gas sensor

Functionalization for the gas sensor : Palladium materials

Limit of detection of the Hydrogen gas : 10 ppm

**2011.09 ~ 2012.02**      Nano science and technology for advanced diagnostics and personalized medicine

National Research Foundation of Korea

Development of the electrochemical/bio sensor using the interdigitated array electrode

Wafer level microfabrication process : Carbon-MEMS

Electrochemical/bio sensing mechanism : Redox cycling amplification

## HONORS AND AWARDS

- 2017 **Yangsong poster the best paper award**, The Korean ceramic society
- 2017 **Excellent research award**, BK21 plus
- 2017 **Encouragement award**, The 23th HumanTech paper award
- 2016 **The best paper award poster session**, The 18<sup>th</sup> KMEMS conference
- 2015 **The best paper award poster session**, The KSME 2015 Spring (Micro & Nano)
- 2015 **The best paper award poster session**, The 17<sup>th</sup> KMEMS conference
- 2014 **The best paper award poster session**, The KSME 2014 Spring (Micro & Nano)
- 2014 **The best paper award poster session**, The KSME 2013 Fall (Micro & Nano)
- 2013 **The best paper award poster session**, The KSME 2013 Spring (Micro & Nano)
- 2013 **The best paper award poster session**, The 15<sup>th</sup> KMEMS conference
- 2011 **The best paper presentation award**, The Korean BioChip 2011 Fall

## JOURNAL PUBLICATIONS

- [1] J. Heo, **Y. Lim**, H. Shin, “The effect of channel height and electrode aspect ratio on redox cycling at carbon interdigitated array nanoelectrodes confined in a microchannel.”, *Analyst* **138** 6404-6411(2013).  
Part : Chemistry, Analytical (12/76), Level Q1, IF : 3.885
- [2] **Y. Lim**, J. Heo, M. Madou, H. Shin, “Monolithic carbon structures including suspended single nanowires and nanomeshes as a sensor platform.” *Nanoscale Res. Lett.* **8** 492 (2013).  
Part : Physics, Applied (40/148), Level Q2, IF : 2.833
- [3] **Y. Lim**, J. Heo, H. Shin, “Fabrication and application of a stacked carbon electrode set including a suspended mesh made of nanowires and a substrate-bound planar electrode toward for an electrochemical/biosensor platform.” *Sens. Actuators B-chem.* **192** 796-803 (2014).  
Part : Instruments & Instrumentation (2/58), Level Q1, IF : 5.401
- [4] **Y. Lim**, Y. Lee, J. Heo, H. Shin, “Highly sensitive hydrogen gas sensor based on a

- suspended palladium/carbon nanowire fabricated via batch microfabrication.”, *Sens. Actuators B-chem.* **210** 218-224 (2015)  
Part : Instruments & Instrumentation (2/58), Level Q1, IF : 5.401
- [5] D. Sharma, Y. Lim, Y. Lee, H. Shin, “Glucose sensor based on redox-cycling between selectively modified and unmodified combs or carbon interdigitated array nanoelectrodes.”, *Anal. Chim. Acta* **889** 194-202 (2015).  
Part : Chemistry, Analytical (7/76), Level Q1, IF : 4.950
- [6] Y. Lee, Y. Lim, H. Shin, “Mixed-scale channel networks including Kingfisher-beak-shaped 3D microchannel for efficient single particle entrapment.”, *Nanoscale* **8** 11810-11817 (2016).  
Part : Materials science, Multidisciplinary (23/275), Level Q1, IF : 7.367
- [7] Y. Lim, J. Woo, S. H. Joo, H. Shin, “Patternable nanoporous carbon electrodes for use as supercapacitors.”, *J. Electrochem. Soc.* **163** A1886-A1892 (2016).  
Part : Materials science, Coatings & Films (2/19), Level Q1, IF : 3.259
- [8] Y. Lim, J. H. Chu, D. H. Lee, S. Kwon, H. Shin, “Increase in graphitization and electrical conductivity of glassy carbon nanowires by rapid thermal annealing.”, *J. Alloy. Comp.* **702** 465-471 (2017).  
Part : Materials science, Multidisciplinary (66/275), Level Q1, IF : 3.133
- [9] J. Seo, Y. Lim, H. Shin, “Self-heating hydrogen gas sensor based on an array of single suspended carbon nanowires functionalized with palladium nanoparticles.” *Sens. Actuators B-chem.* **247** 564-572 (2017).  
Part : Instruments & Instrumentation (2/58), Level Q1, IF : 5.401
- [10] Y. Lim, S. Kim, Y. M. Kwon, J. M. Baik, H. Shin, “A highly sensitive gas-sensing platform based on a metal-oxide nanowire forest grown on a suspended carbon nanowire fabricated at a wafer level.”, *Sens. Actuators B-chem.* **260** 55-62 (2018).  
Part : Instruments & Instrumentation (2/58), Level Q1, IF : 5.401
- [11] S. Choi, K. Park, S. Lee, Y. Lim, B. Oh, H. Y. Chae, C. S. Park, H. Shin, J. J. Kim, “A three-step resolution-reconfigurable hazardous multi-gas sensor interface for wireless air-quality monitoring applications”, *Sensors* **18** 761 (2018).  
Part : Instruments & Instrumentation (10/58), Level Q1, IF : 2.677

- [12] H. Seo, **Y. Lim**, H. Shin, I. C. Bang, “Effects of hole patterns on surface temperature distributions in pool boiling.”, *Int. J. Heat Mass Transf.* **120** 587-596 (2018).  
Part : Mechanics (9/133), Level Q1, IF : 3.458
- [13] J. Lee, D. Sharma, **Y. Lim**, H. Shin, “Redox cycling effect at microchannel-integrated sandwich electrodes consisting of a suspended mesh and a substrate-bound planar electrode.”, *Sens. Actuator B-chem.* **267** 467-475 (2018).  
Part : Instruments & Instrumentation (2/58), Level Q1, IF : 5.401

### **INTERNATIONAL CONFERENCE PROCEEDINGS**

- [1] **Y. Lim**, J. Heo, M. Madou, H. Shin, “Hybrid monolithic 3D carbon suspended nanowires for the application of electrochemical sensing platform.”, *The 5th International Conference on Sensors*, (11. 10. 23 – 10. 26), Jeju, Republic of Korea.
- [2] J. Heo, **Y. Lim**, M. Madou, H. Shin, “Scalable suspended carbon nanowire meshes as ultrasensitive electrochemical sensing platforms.”, *25th IEEE International Conference on Micro Electro Mechanical Systems*, (12. 01. 29 – 02. 02), Paris, France.
- [3] J. Heo, **Y. Lim**, B. Lee, M. Madou, H. Shin, “Development of a carbon microchannel integrated with a horizontal carbon sandwich electrode pair for ultra sensitive electrochemical/bio sensors.”, *The 16th International Conference on Miniaturized Systems for Chemistry and Life Sciences*, (12. 10. 28 – 11. 01), Okinawa, Japan.
- [4] **Y. Lim**, B. Lee, J. Heo, H. Shin, “Gold nanoparticle-carbon nanowire hybrid interdigitated array nanoelectrodes for enhancing electrochemical signal amplification.”, *The 17th International Conference on Solid-State Sensors, Actuators and Microsystems*, (13. 06. 16 – 06. 20), Barcelona, Spain.
- [5] **Y. Lim**, J. Heo, H. Shin, “A stacked electrode set including suspended carbon nanomeshes and planar carbon pads for electrochemical/bio sensor applications.”, *The 17th International Conference on Solid-State Sensors, Actuators and Microsystems*, (13. 06. 16 – 06. 20), Barcelona, Spain.
- [6] **Y. Lim**, J. Heo, M. Madou, H. Shin, “Development of suspended 2D carbon nanostructures: nanowires to nanomeshes.”, *The 17th International Conference on*

- Solid-State Sensors, Actuators and Microsystems*, (13. 06. 16 – 06. 20), Barcelona, Spain.
- [7] J. Heo, Y. Lim, H. Shin, “Development of a hydrogen gas sensor based on a suspended monolithic carbon nanowire platform.”, *The 17th International Conference on Solid-State Sensors, Actuators and Microsystems*, (13. 06. 16 – 06. 20), Barcelona, Spain.
- [8] Y. Lim, J. Heo, H. Shin, “Suspended carbon nanowire-based structures for sensor platforms.”, *225th ECS Meeting*, (14. 05. 11 – 05. 15), Orlando, USA.
- [9] Y. Lee, Y. Lim, H. Shin, “Fabrication of a monolithic carbon mold for producing a mixed-scale PDMS channel network using a single molding process.”, *The 28th IEEE International Conference on Micro Electro Mechanical Systems*, (15. 01. 18 – 01. 22), Estoril, France, Portugal.
- [10] Y. Lim, Y. Lee, J. Lee, H. Shin, “A circumferentially grown ZnO nanowire forest on a suspended carbon nanowire for a highly sensitive gas sensor.”, *The 28th IEEE International Conference on Micro Electro Mechanical Systems*, (15. 01. 18 – 01. 22), Estoril, France, Portugal.
- [11] Y. Lee, Y. Lim, H. Shin, “Development of the batch fabrication technique using carbon-MEMS for mixed-scale channel networks including tapered 3D microfunnels.”, *The 19th International Conference on Miniaturized Systems for Chemistry and Life Sciences*, (15. 10. 25 – 10. 29), Gyeongju, Republic of Korea.
- [12] D. Sharma, Y. Lim, Y. Lee, H. Shin, “Carbon-interdigitated-array-nanoelectrode-based glucose sensor using redox-cycling between selectively modified and unmodified comb sets.”, *The 19th International Conference on Miniaturized Systems for Chemistry and Life Sciences*, (15. 10. 25 – 10. 29), Gyeongju, Republic of Korea.
- [13] J. Lee, Y. Lim, H. Shin, “Alignment-less microchannel integration onto a stacked carbon electrode set for highly sensitive electrochemical sensor applications.”, *IEEE Sensors 2015*, (15. 11. 01 – 11. 04), Busan, Republic of Korea.
- [14] D. Sharma, Y. Lim, J. Lee, H. Shin, “Electrochemical-enzymatic redox cycling based glucose sensing using selectively functionalized dual carbon nanoelectrodes.”, *The 26th Anniversary World Congress on Biosensors*, (16. 05. 25 – 05. 27), Gothenburg, Sweden.



- [15] **Y. Lim**, S. H. Joo, H. Shin, “Development of pyrolyzed nanoporous carbon electrodes with sponge-like networks of mesopores for use as supercapacitors.”, *225th ECS Meeting*, (16. 05. 29 – 06. 02), San Diego, USA.
- [16] J. Seo, **Y. Lim**, H. Shin, “High performance hydrogen sensor based on an array of single suspended carbon nanowires selectively functionalized with palladium nanoparticles.”, *30th IEEE International Conference on Micro Electro Mechanical Systems*, (17. 01. 22 – 01. 26), LAS Vegas, USA.
- [17] **Y. Lim**, D. Sharma, H. Shin, “Development of patternable nanoporous carbon electrodes for use as biosensors based on redox cycling effect.”, *30th IEEE International Conference on Micro Electro Mechanical Systems*, (17. 01. 22 – 01. 26), LAS Vegas, USA.
- [18] **Y. Lim**, J. H. Chu, D. H. Lee, S. -Y. Kwon, H. Shin, “Electrical conductivity enhancement of 1D glassy carbon nanostructure using rapid thermal annealing.”, *The 17th International Conference on Solid-State Sensors, Actuators and Microsystems*, (17. 06. 18 – 06. 22), Kaohsiung, Taiwan.
- [19] **Y. Lim**, H. Shin, “Metal oxide nanowire forest grown selectively on a suspended carbon nanowire for use as gas sensor platform.”, *7th Gas sensors based on semiconducting metal oxides – basic understanding & application fields*, (17. 11. 08 – 11. 10), Seoul, Republic of Korea.
- [20] **Y. Lim**, S. Lee, Y. M. Kwon, J. M. Baik, H. Shin, “Gas sensor based on a metal oxide nanowire forest built on a suspended carbon nano-heater.”, *31th IEEE International Conference on Micro Electro Mechanical Systems*, (18. 01. 21 – 01. 25), Belfast, United Kingdom.

## PATENTS

- [1] “**Bio Sensor and Manufacturing Method for Bio Sensor Thereof.**”, Domestic patent registration (13. 08. 05, 1012953990000)
- [2] “**Bio Sensor Manufacturing Method.**”, Domestic patent registration (14. 03. 03, 1013721720000) and America patent registration (17. 06. 06, 9, 671, 360)
- [3] “**Manufacturing Method for Bio Sensor.**”, Domestic patent registration (14. 03. 03, 1013718240000)
- [4] “**Bio Sensor and Manufacturing Method Thereof.**”, Domestic patent registration (14. 03. 03, 1013718440000)
- [5] “**Fabrication Method for Gas Sensor and Temperature Sensor based on Suspended Carbon Nanowires.**”, Domestic patent registration (14. 05. 28, 1014034060000)
- [6] “**Manufacturing Method of a Mold for a Microfluidic Chip Integrated with Multiscale Channels.**”, Domestic patent registration (14. 06. 18, 1014113350000)
- [7] “**Method for Forming Nanostructure.**”, Domestic patent registration (15. 03. 26, 101508040000)
- [8] “**Gas Sensor and Method for Manufacturing Gas Sensor.**”, Domestic patent registration (16. 10. 05, 1016650200000)
- [9] “**Method for Manufacturing a Suspended Single Carbon Nanowire and Piled Nano-electrode pairs.**”, America patent registration (16. 12. 06, 9, 513, 555)
- [10] “**Fabrication Method for Carbon Electrodes with Multi-Scale Pores.**”, Domestic patent registration (16. 12. 19, 1016891600000)
- [11] “**Method of Manufacturing Carbon Structure.**”, Domestic patent registration (17. 11. 30, 1018054220000)